DISSERTATION

FUNDAMENTAL STUDIES OF REVERSE MICELLEAR AGGREAGATES BY MULTIMUCLEAR AND MULTIDIMENSIONAL NMR SPECTROSCOPY

Submitted by

Myles Sedgwick

Department of Chemistry

In partial fulfillment of the requirements

For the Degree of Doctor of Philosophy

Colorado State University

Fort Collins, Colorado

Fall 2012

Doctoral Committee:

Advisor: Nancy Levinger

Debbie Crans
Chuck Henry
Deborah Roess
Alan van Orden

ABSTRACT

FUNDAMENTAL STUDIES OF REVERSE MICELLEAR AGGREAGATES BY MULTIMUCLEAR AND MULTIDIMENSIONAL NMR SPECTROSCOPY

Self-assembled reverse micellar aggregates using cationic, anionic and non-ionic surfactants have been investigated by multinuclear and multidimensional NMR. By utilizing ^{51}V NMR chemical shifts and line widths of decavanadate, the local proton concentration and characteristics of the reverse micellar environment are measured. There is a distinct environmental change on the interior of the reverse micelle depending on the surfactant used. ^{51}V NMR signals for decavanadate inside an Igepal CO-520, non-ionic surfactant, reverse micelle display sharp signals indicating the decavanadate experiences water like environment. Conversely, ^{51}V NMR signals for decavanadate inside an Igepal CO-610/430 mixed reverse micelle show significant broadening of the decavanadate signal indicating that the environment inside the reverse micelle in which the decavanadate resides is more viscous. These data provide a description in that the water pool of non-ionic surfactants can be compared.

Time resolved anisotropy decays, ultrafast time-resolved transient absorption, and 2D NMR spectroscopy have been used to study proton transfer reactions in the interiors of Igepal-CO 520, CTAB and AOT reverse micelles. For $w_0 = 10$ reverse micelles formed with anionic AOT surfactant, the HPTS proton transfer dynamics are similar to dynamics in bulk aqueous solution, and the corresponding ^{1}H 2D NOESY NMR spectra display no cross peaks between HPTS and AOT consistent with the HPTS residing, well-hydrated by water, in the interior of the reverse micelle water pool. In contrast, ultrafast transient absorption experiments show no evidence for HPTS photoinduced proton transfer reaction in reverse micelles formed with the cationic CTAB surfactant. In CTAB reverse micelles, clear cross peaks between HPTS and CTAB in the 2D NMR spectra show that HPTS embeds in the interface. Similar behavior is observed for HPTS in Igepal reverse micelles as in CTAB reverse micelles and we interpret the slowed dynamics in the same manner. The 2D NMR spectra for HPTS in Igepal-CO 520 reverse micelles shows interaction that imply the HPTS molecule is rested near the interface inside the reverse micelle.

Dynamic light scattering (DLS) and ^{1}H NMR spectroscopic experiments suggest that the assembly of the reverse micellar aggregates depends on non-polar solvent and co-surfactant used. Two different self-assembled particles form in the AOT/cholesterol /water in cyclohexane, where in the similar system of AOT/cholesterol /water in 1-octanol there is only one particle present. In microemulsions employing 1-octanol as the continuous medium, AOT reverse micelles form in a dispersed solution of cholesterol in 1-octanol. Although the size distribution of self-assembled particles is well-known for many different systems, evidence for simultaneous formation of two distinctly sized particles in solution that are chemically different is unprecedented.

By utilizing optical spectroscopic techniques, 2D NMR, and DLS, the structure of the non-ionic reverse micelles have been characterized. The impact of adding cholesterol, a biologically relevant molecule, has on the structure of the reverse micellar solutions has also been shown.

ACKNOWLEDGEMENTS

I would first like to thank my advisors Nancy Levinger and Debbie Crans, from whom I have learned a great deal from. Without their guidance and persistent help and support, this dissertation would not have been possible. Whether it is Nancy's passion for research or Debbie's excitement when an experiment yielded promising results, it has been nothing but a pleasure to be a member of each of their research groups.

Without the support of my family and friends, I would have given up on graduate school a long time ago. Whether it was helping cover a class for me or coming over to make me dinner while I was writing my thesis, their constant support means a great deal to me.

I would additionally like to thank each member of Levinger and Crans research groups. Without the support from the group members, I would not have been able to finish this work. Their willingness to drop what they were doing to help me out when I was having trouble with an experiment, or trying to synthesize something, meant a lot to me.

TABLE OF CONTENTS

LIST OF TABLES

LIST OF FIGURES

CHAPTER 1

INTRODUCTION

1.1 Reverse Micelles

Amphiphiles can spontaneously assemble into a range of interesting and useful structures, such as those displayed in Figure 1.1.[1,2] Most commonly we are familiar with lipid bilayer structures that form the basis for biological membranes.[1] Within these structures water exists at both the interfaces and in localized, nanoscopic pockets. It is well established that when water is confined, it has drastically different properties than it does in the bulk.

In ternary mixtures of polar, nonpolar and amphiphilic molecules, a wide range of structures can form, including isolated nanoscale water droplets dispersed in a non- polar phase, that is, reverse micelles.[3] These nanoscale water droplets give us the ability to study water in confinement. Reverse micelle have been used for many different applications including modeling biological reactions[4-7], nanoreactors[8,9], templates for nanoparticle syntheses[10-13], drug delivery vessels[14-16], and even electronic displays[17,18]. Researchers have been using probe molecules to try to elucidate the nature of the water pool and interface inside the reverse micelle. Typically the location of a probe molecule is key to understanding what it is reporting.[4,5,16,19,20] In the past, researchers have been using solubility and charge arguments to determine the location of the probe molecule without actually measuring its location. Previous work in the Levinger and Crans

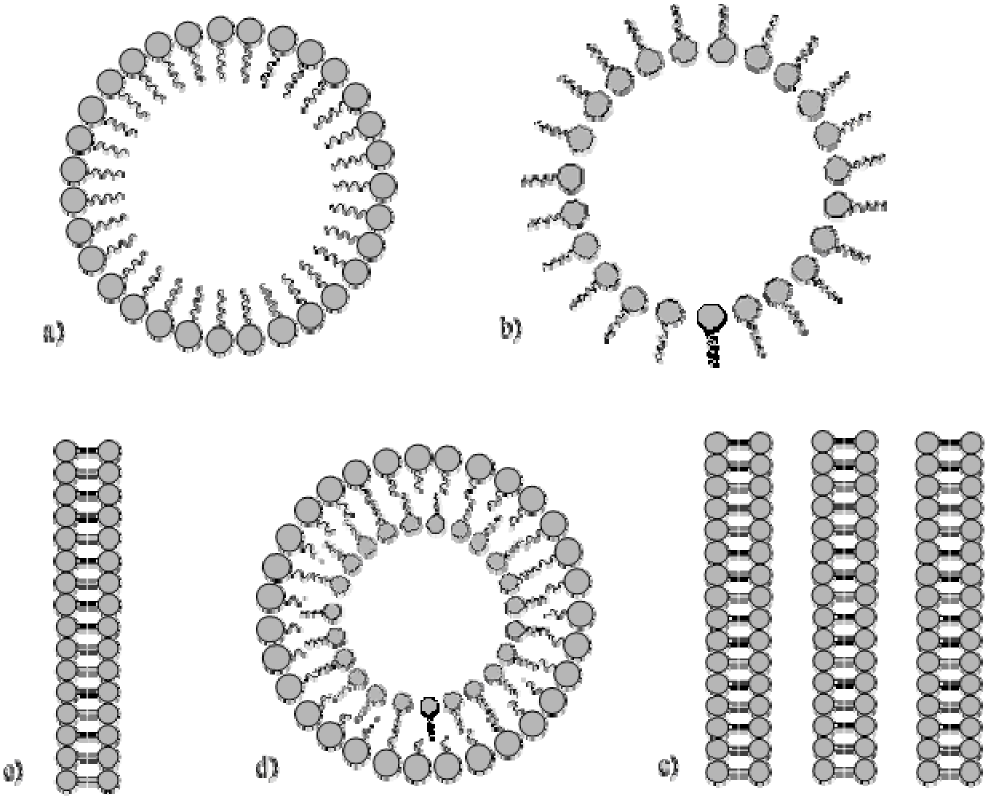

Figure 1.1 Various self-assembled surfactant structures. a) micelle, b) reverse micelle, c) bilayer, d) vesicle and e) multilayer.

groups has shown that using such arguments alone are not enough, as demonstrated by the embedding of a doubly deprotonated probe into a negatively charged interface.[20] One focus of the work reported in this dissertation is the location of various probe molecules inside various reverse micelle systems.

Reverse micelles form in ternary systems, comprising of a polar solvent, nonpolar solvent, and a surfactant, where the polar solvent forms a nanodroplet surrounded by surfactant, Figure 1.1b.[3,19,21-24] In some cases, a cosurfactant is needed for reverse micelle formation.[25,26] Common non-polar solvents that are used include isooctane, cyclohexane, benzene, n-hexane, carbon tetrachloride and dichloroethane.[2,3,15,18,24,25,27-31] In general, reverse micelles are defined by the ratio of the polar solvent (usually water) to the amount of surfactant present,

$$w_0 = \frac{[\text{polar solvent}]}{[\text{surfactant}]} \tag{1.1}$$

If the reverse micelles are spherical, $w_0 \propto r_H$, the hydrodynamic radius. Thus, as w_0 increases, the radius of the reverse micelle also increases.

Reverse micelle research is a continuously growing field.[32] Every year there are new reactions or applications for these robust systems, whether it be new ways to make nanoparticles or for drug formulations. With renewed interest in these systems comes the necessity to make reverse micelles with certain desirable properties and characteristics.

Reverse micelles can be made from a variety of different surfactants, for example those shown in Figure 1.2, giving rise to different types of interfaces. Surfactants are classified based on the composition of their polar head group. There are four different classes of surfactants that are commonly used anionic, cationic, zwitterionic, and non-ionic.

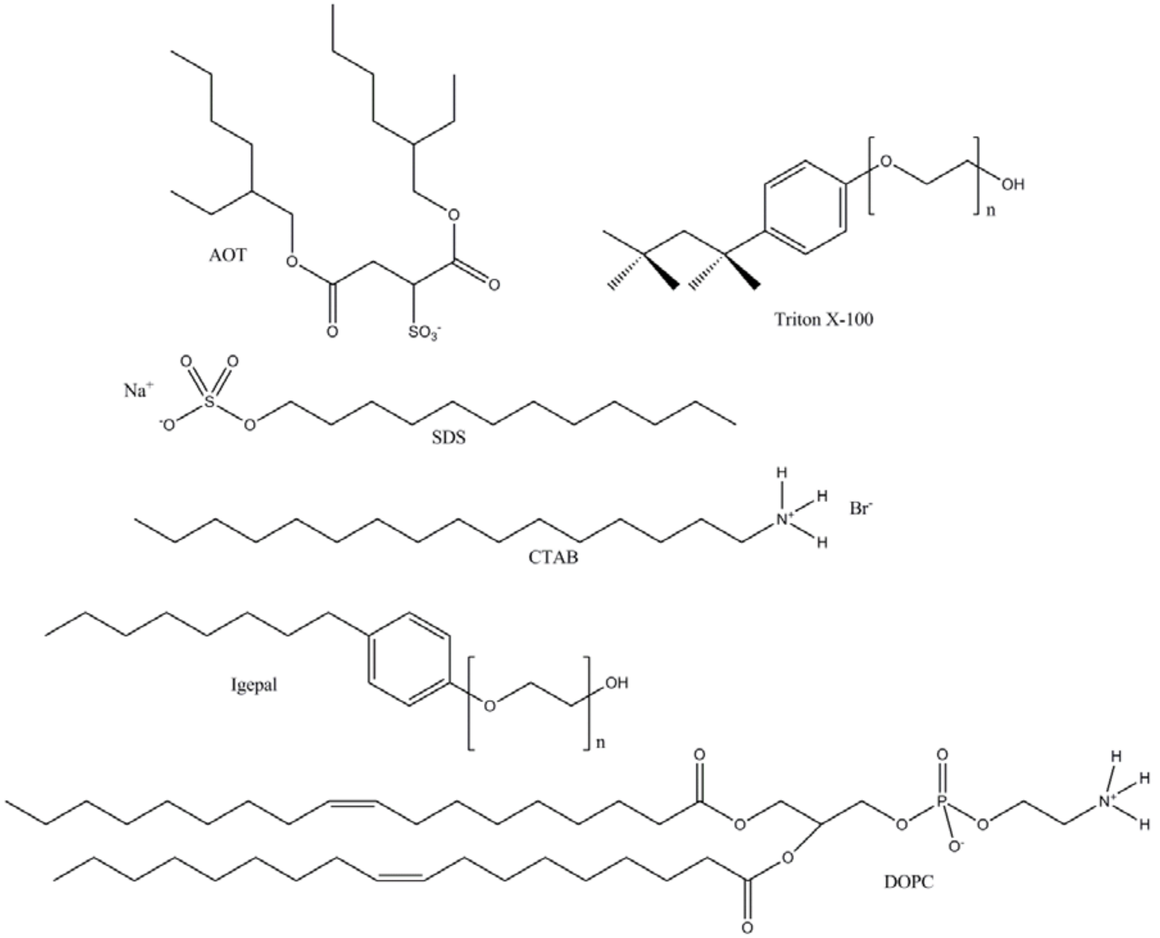

Figure 1.2 Common surfactants used to make reverse micelles. Aerosol OT (AOT) and sodium dodecyl sulfate (SDS) are both anionic surfactants. Cetyltrimethylammonium bromide (CTAB) is a cationic surfactant, needing a co-surfactant to make reverse micelles. Polyoxyethylene octyl

phenyl ether (Triton X-100) and the Igepal are common nonionic surfactants; for Triton X-100, n=9.5 for Igepal CO-520, n=5. Dioleoylphosphatidylcholine (DOPC) is a zwitterionic surfactant.

There are a few different types of anionic surfactants that can be used to make reverse micelles. The most commonly used anionic reverse micelle system is Aerosol OT (AOT) in isooctane.[30,33,34] AOT can form reverse micelles in isooctane over an incredibly large concentration range, from [AOT] = 10^{-3} M to up to 1 M. This system also has a large accessible w_0 range, from w_0= 0 ~50. The surfactant AOT was used for the work reported in chapters 4 and 5.

Cetyltrimethylammonium bromide (CTAB) is one of the most commonly used cationic surfactants and is one of the surfactants used for studies reported in chapter 5. Unlike AOT, CTAB requires the use of a co-surfactant, typically a straight chain alcohol such a 1-octanol or 1-pentanol. To make stable reverse micelles, the molar ratio of co-surfactant to surfactant needs to be from 4:1 to 6:1. Within this range, when the CTAB concentration is 0.1 M, reverse micelles can be formed with w_0's from 0-20. For the same w_0, these reverse micelles are slightly bigger than their AOT counterparts.[31,33] The size can be measured by DLS. The size difference is related to the different aggregation numbers for CTAB reverse micelles and AOT reverse micelles.

For reactions that are sensitive to other ions present, there has been a push to use non-ionic surfactants to make reverse micelles. Two common families of non-ionic surfactants have commonly been used. The alkyl polyethylene ethers are one class, which has a straight alkyl tail attached to a polyethylene glycol head group, Brij-35 is one such surfactant. While the other family, alkyl phenyl polyethylene glycols, have an alkyl tail attached to a phenyl polyethylene glycol. Triton X-100 (n=9.5) and Igepal CO-520 (n=5), alkyl phenyl polyethylene glycols, can make large reverse micelles in a narrow concentration range, 0.2 M to 0.4M in cyclohexane. There is far less freedom in these systems for both non-polar solvent choices and concentrations, than there is with AOT. Both Igepal CO-520 and Triton X-100 can form reverse micelles from a w_0 range of 1 to30. Igepal CO-430 (n=4) and Igepal CO610 (n=6.5) do not form large reverse micelles, $w_0 > 6$, on their own. But when these surfactants are mixed in a 3:1 ratio (0.4 M in surfactant) the mixture can form reverse micelles similar in size those formed with to Igepal CO-520. The differences between Igepal CO-520 and 610/430 reverse micelles are explored further in chapter 3.

Understanding the nature of the reverse micelle systems is key to understanding and predicting the behavior of other molecules in the reverse micelles. The work presented in this dissertation focuses on the differences between anionic, cationic and non-ionic reverse micelles. Details for how to make reverse micelle solutions are presented in chapter 2.1a, 1.1b and 2.1c.

1.2 Dynamic Light Scattering

Dynamic Light Scattering (DLS) is a technique used to measure the size distribution of particles in suspension or polymer solution. When coherent, monochromatic light impinges on the solution with particles in it, there are small time dependent fluctuations in the intensity of the scattered light. The fluctuations measured arise from the laser light that scatters off particles undergoing Brownian motion.[35] A simple experimental set up for a dynamic light scattering experiment is provided in Figure 1.3.

A correlation function can be used to determine repeating patterns in a set of data. To measure the correlation of the intensity of the signal, the time average of the signal is taken,

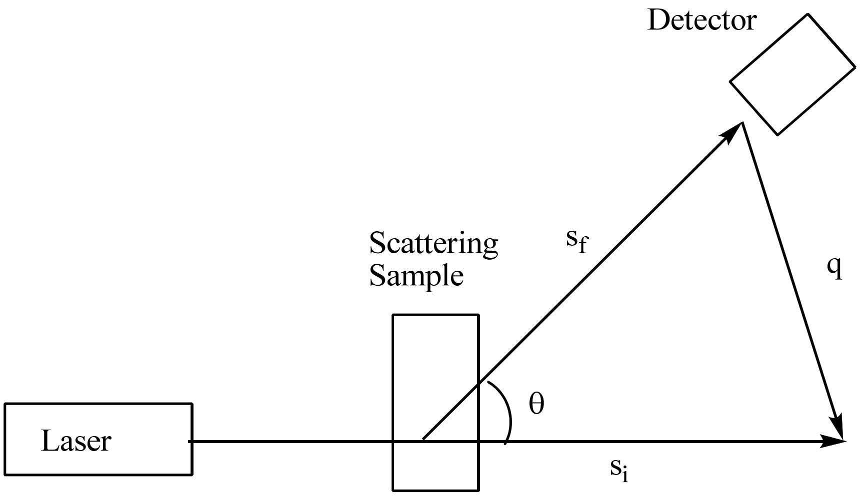

Figure 1.3 Schematic representations of an instrument for a dynamic light scatter experiment.

For the Wyatt DYNAPRO Titan, $\theta=90^o$.

which is an autocorrelation function. In a monodisperse sample, the autocorrelation function is related to the diffusion constant (D) by G(τ). (Equation 1.2 and Equation 1.3)[35]

$$G(\tau) = \langle I(t) \rangle^2 + \langle I(t) \rangle^2 \alpha e^{-2Dq^2\tau} \tag{1.2}$$

$$q = \frac{4\pi n}{\lambda_0} \sin\left(\frac{\theta}{2}\right) \tag{1.3}$$

where $\langle I(t) \rangle$ is the average intensity of the scattered light, α is an instrument scaling factor, n is the refractive index, λ_0 is the wavelength of the light source and θ is the angle of detection with respect to the incident beam (Figure 1.3).

If a hard sphere undergoing Brownian motion in a liquid has significant solvent/solute interactions, then the Stokes-Einstein relationship describes that sphere's diffusion constant. (Equation 1.2)[35]

$$D = \frac{k_b T}{6\pi\eta r_h} \tag{1.4}$$

By knowing the viscosity (η) and refractive index (n) of the sample, one can measure the hydrodynamic radius (r_h) of particles in the solution. In the work presented here, this technique is used to characterize and confirm the formation of reverse micelles, as well as characterize secondary particles that co-exist in solution (chapter 4).

1.3 NMR Spectroscopy

1.3.a ^{51}V NMR Spectroscopy

Vanadium has two isotopes, ^{50}V and ^{51}V, both of which are NMR active and quadrupolar. Due to its high natural abundance (99.5%) and larger receptivity (Table 1.1),[36] ^{51}V is a prime

Table 1.1 Nuclear Properties of Vanadium Isotopes.[36]

	^{50}V	^{51}V
Spin	6	7/2
Natural Abundance	0.24%	99.76%
Relative Receptivity (1 for ^{1}H)	1.34×10^{-4}	0.383
Resonance Frequency (100 MHz for ^{1}H)	9.987 MHz	26.336 MHz

choice for study. Being a quadrupolar nucleus, ^{51}V is sensitive to it local chemical environment, giving rise to a large chemical shift window and sensitivity in the line broadening. The chemical shift window for ^{51}V is very broad (almost 5000 ppm) and depends on the electronic influences of the coordination on the vanadium.[37-39] For example, the signal for VF_5 appears at -865ppm (relative to $VOCl_3$) while $[VSe_4]^{3-}$ appears at 2570 ppm (relative to $VOCl_3$)[37]. Commonly $VOCl_3$ is used to determine 0.0 ppm for solution vanadium NMR. Vanadates have chemical shifts that are usually between -300 and -600ppm. For the results presented in chapter 3, $VOCl_3$ was used to determine the 0.0 ppm and then all spectra were referenced versus a 1M pH=12 sodium orthovanadate solution at -535.7ppm (VO_4^{3-}).

1.3.b Nuclear Overhauser Effect

When one nuclear spin in a system is perturbed, the net intensities of other spins in the system may be affected. When this perturbation is brought about by dipole-dipole cross relaxation, it is known as the nuclear Overhauser effect, NOE.[40] The benefit of this type of interaction is that it can occur through space rather than through bond. This implies that one can identify spins on atoms that are located spatially close to each other that are not close to each other on a molecule through bond. Typically this technique is used to elucidate conformational changes or folding for macromolecules and proteins.[40]

To describe the NOE, for convenience; if we consider a two spin ½ systems (nuclei like ^{1}H), the NOE interaction adds two more energy levels to the energy level diagram, Figure 1.4. In Figure 1.4, the W_I, the transition is at which the resonance is measured, and W_S, the transition in which the resonance is saturated, are referred to as the single quantum transitions.[41] These transitions are responsible for the spin-lattice relaxation of the system. W_2 is double quantum transition and W_0 is the zero quantum transition, both of which are known as cross-relaxation pathways. What is important to note is that W_2 and W_0 involve a simultaneous flip of both spins. These transitions are forbidden in the sense they cannot be excited directly via these pathways, but the system can relax via these pathways. The ability for the spin systems to relax in this manner is the nature of the NOE.

A schematic for a NOE experiment is provided in Figure 1.5. In the NOE experiment, first the W_{1S} transition is saturated, Figure 1.5.a. When this occurs there is equal population of spins in the αα and αβ states and similarly βα and ββ have equal populations as well. Figure 1.5.b shows the relaxation of the system via the W_2 transition. This leads to a net gain in population in the αα and αβ state, which will lead to a net positive NOE enhancement. Conversely, Figure 1.5.c shows the relaxation of the system via the W_0 pathway. This leads to a net loss of population in the αα and αβ states leading to a net negative NOE enhancement. The magnitude of the NOE enhancement is given by Equation 1.5.[41]

$$\varepsilon_{\mathrm{NOE}} = \frac{\gamma_I}{\gamma_S}\frac{(\mathrm{W}_2-\mathrm{W}_0)}{\mathrm{W}_0+2\mathrm{W}_{\mathrm{IS}}+\mathrm{W}_2} \tag{1.5}$$

where γ_I and γ_S are the gyromagnetic ratios of the two nuclei of interest. For a homonuclear experiment, these gyromagnetic ratios are the same and the net NOE enhancement is dependent on W_2, W_{1S} and W_0. It has been shown that a transition corresponding to a given frequency is promoted by molecular motion at the same frequency.[40] Equation 1.6 shows the relationship of the NOE enhancement with the rotational correlation time, τ_c

$$\varepsilon_{\mathrm{NOE}} = \frac{5+\omega^2{\tau_c}^2-4\omega^2{\tau_c}^2}{10+23\omega^2{\tau_c}^2+4\omega^2{\tau_c}^2} \tag{1.6}$$

where ω is the Larmor frequency. The net NOE enhancement is zero when the numerator in equation 1.6 is equal to 0. This occurs at $\varepsilon_{NOE} = \sqrt{(5/4)} \approx 1.12$. In the "extreme narrowing limit", $\omega\tau_c \ll 1$, the ratios of W_0, W_S, and W_2 are 2:3:12[41], which when substituted back into

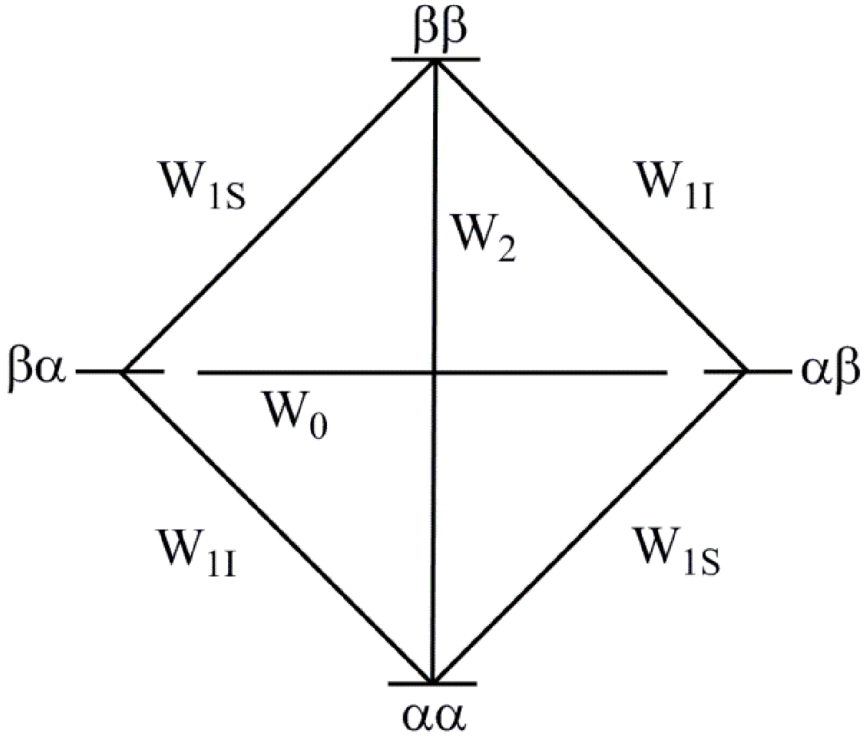

Figure 1.4 Energy level diagram for a two spin system. Both the energy levels and transitions are labeled. W_{1I} is the transition that will be measured.[40]

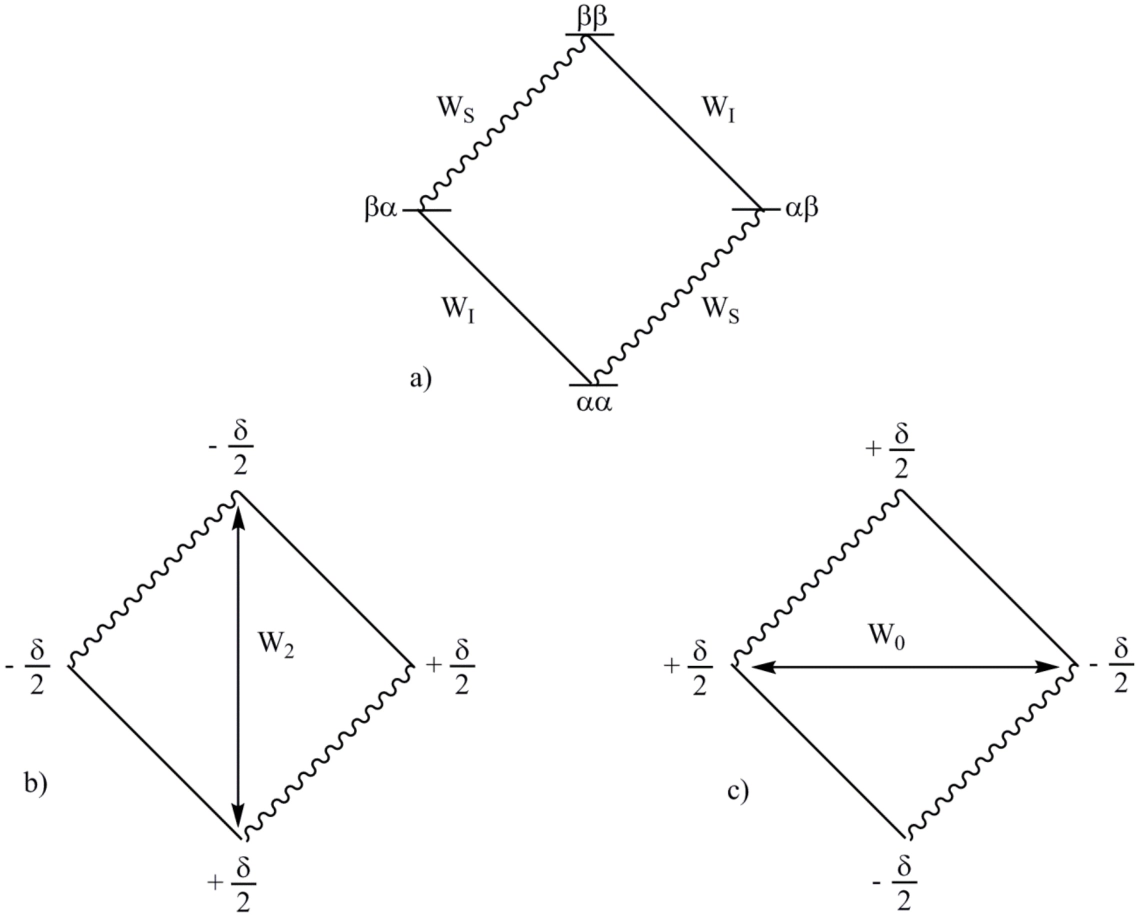

Figure 1.5 Energy level diagram describing the nature of the NOE. a) is the system after saturation of the W_S transition. b) Illustrates the effect on the spin system the W_2 relaxation has on the system. c) Illustrates the effect on the spin system the W_0 relaxation has on the spin system.[40]

equation 1.5, showing that the NOE enhancement is 0.5. Figure 1.6 shows the dependence of the max NOE enhancement on $\omega\tau_{c.}$[40]

1.3.c 2D NMR Spectroscopy

1.3.c.i NOESY Theory

NOESY, or nuclear Overhauser effect (enhancement) spectroscopy, is a method in which all the nuclei that are spatially close can be observed simultaneously. This can be a powerful tool in elucidating the structure and conformation of certain molecules and systems. This type of experiment is not without its disadvantages, mainly the time requirement to acquire a decent spectrum. Experiments can take hours to complete depending on how many transients are collected.

In a 2D NOESY experiment, Figure 1.7, after the first pulse both spins A and B precess in the xy-plane. The rate in which A and B precess in the rotating frame is ω_A and ω_B, respectively. After some time has passed, t_1, the angle in which each spin has precessed through is $\omega_A t_1$ and $\omega_B t_1$, Figure 1.8. Now, a second pulse (Figure 1.7) rotates the spins into the xz-plane. The z-component of the magnetization present after the second pulse is given by $-\cos\omega_A t_1$ and $-\cos\omega_B t_1$ and are said to be frequency labeled.[40] This means the magnitude of the z-component is a function of t_1. The third and final pulse is used to measure the z-magnetization present at the end of t_m and is measured for a time t_2.

If t_m is zero, the third pulse would occur immediately after the second pulse and the precession frequency of each spin would be measured as a function of t_1. This however is not informative, because the precession frequencies during t_1 are the same as they are for t_2 since there is nothing that could have happened between t_1 and t_2 that could have changed them. The data is generated function of both t_1 and t_2 and then plotted as the Fourier transform (FT) of t_1

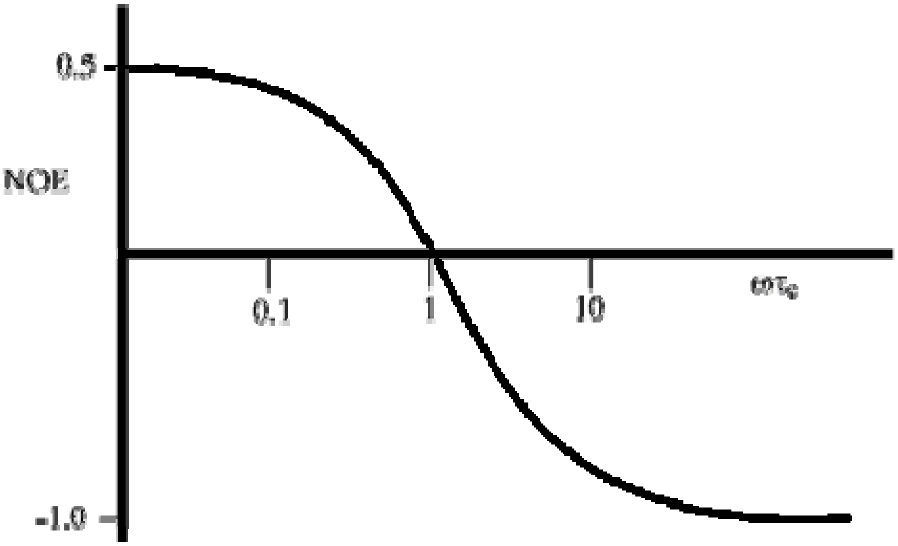

Figure 1.6 Cartoon illustrating the dependence of the maximum NOE enhancement on $\omega\tau_c$.

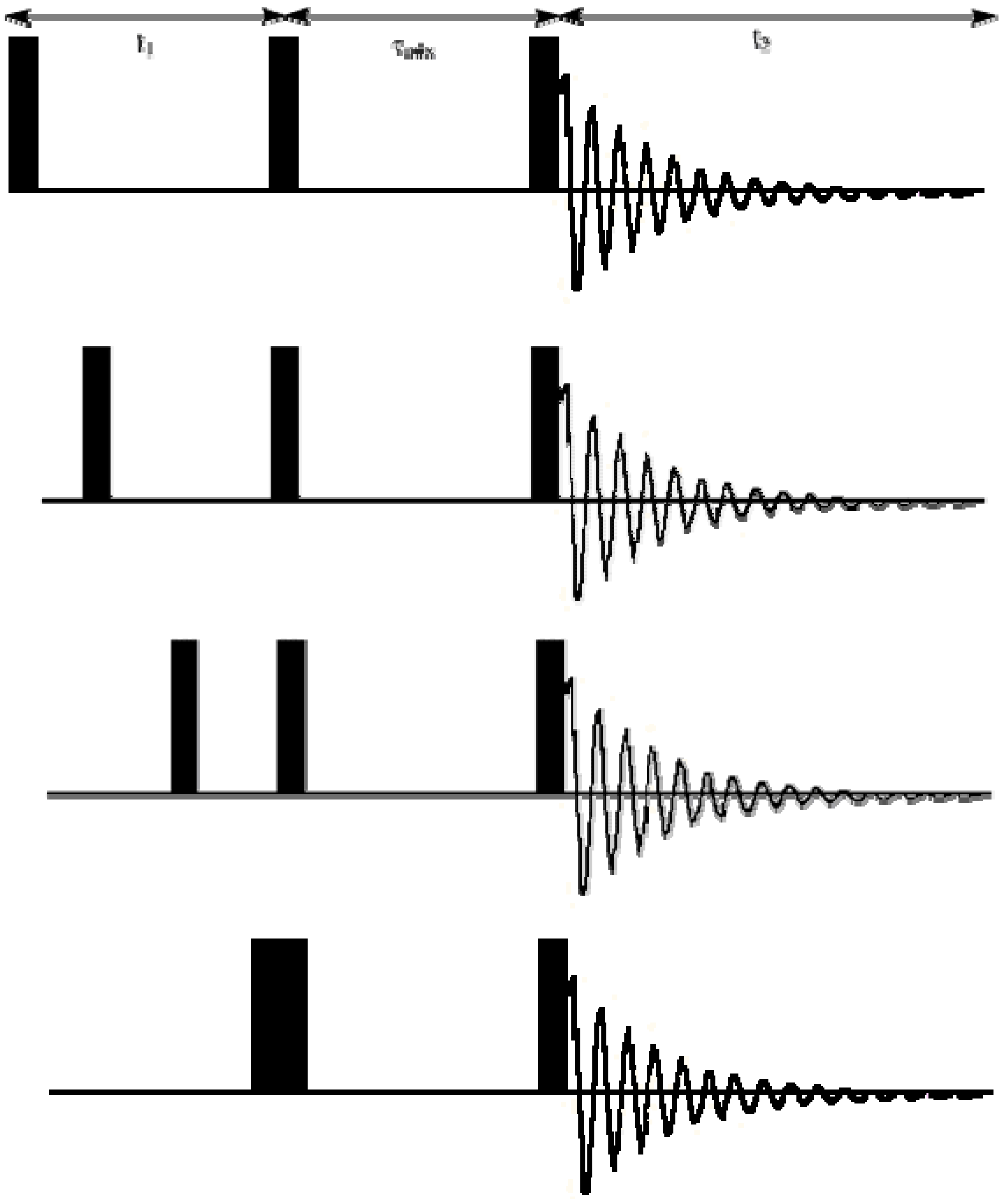

Figure 1.7 Pulse sequence for a 2D NOESY experiment, illustrating the evolution of t_1 during the course of the experiment.

and t_2 (F1 and F2 respectively). We have now generated a plot containing only two peaks having the same frequency in both F1 and F2. These peaks are referred to a diagonal peaks, or “the diagonal” since they lie on the 45^{o} diagonal of the 2D plot, illustrated in Figure 1.8.a.

A NOESY experiment occurs when t_m is not zero, where there is a fixed time delay between the second and third pulse. t_m is the time in which exchange of magnetization can occur, thus generating the NOE. If t_m is too short or there are no interactions during this time, there will be no NOE signal and the plot will look similarly to the plot described Figure 1.8.a. Conversely, if t_m is too long, equilibrium will have been restored between the pulses and no NOE will be observed.

When t_m is chosen appropriately, useful information is obtained if spins A and B undergo magnetization exchange or chemical change during t_m. The amplitude of the signal from spin A ($-\cos\omega_A t_1$) has an additional dependence on $-\cos\omega_B t_1$. The total affects that $-\cos\omega_B t_1$ has on $-\cos\omega_A t_1$ is dependent on the strength and sign of the enhancement. Figure 1.8.b shows the 2D spectrum where t_m is sufficiently long and magnetization exchange has occurred. For spin A, with the dependence of $-\cos\omega_B t_1$ on $-\cos\omega_A t_1$, when the FT is applied with respect to t_1, two peaks are present. One peak is dependent on ω_A and the other on ω_B. The peak corresponding to ω_A for spin A (F1=A, F2=A) is the diagonal peak described earlier, but the peak corresponding to ω_B is peak that appears at (F1=A, F2=B). For large molecules ($\omega\tau_c \gg 1.12$) the diagonal and the cross-peaks will have the same sign, where for small molecules ($\omega\tau_c \ll 1.12$) the diagonal and the cross-peaks have opposite sign.

1.3.c.ii Chemical Exchange

Chemical exchange in a sense contributes in a similar manner to a negative NOE enhancement or the large molecule case.[42] In this case, we will consider a dilute solution ($\chi_A \ll 1$,

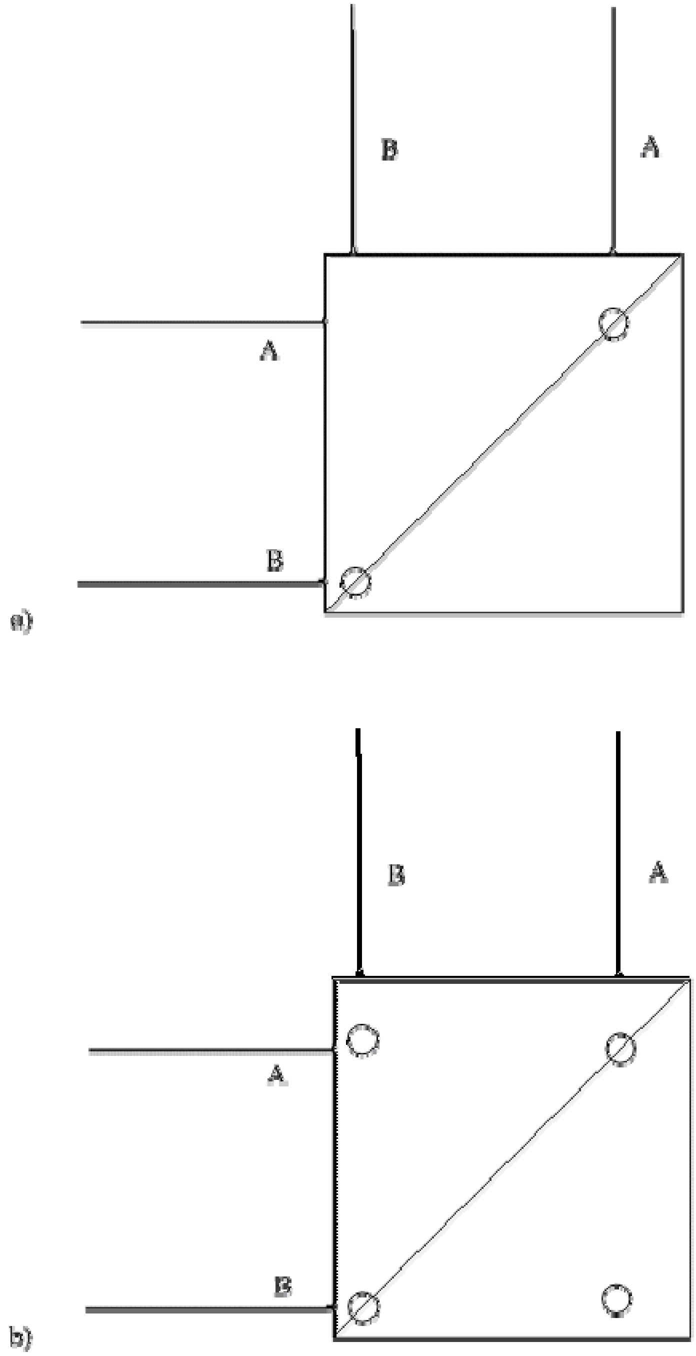

Figure 1.8 Schematic 2D spectrum contour plots. a) 2D NOESY spectrum where $\tau_m = 0$ or sufficiently small enough to not allow spins A and B to cross –relax. b) 2D NOESY spectrum where $\tau_m \neq 0$ and cross-relaxation occurs.

and $\chi_B \cong 1$) of A spin molecules in a B spin solvent. In the absence of dipole-dipole relaxation, for slow chemical exchange processes (k_{AB}, $k_{BA} \ll |\omega_A - \omega_B|$) magnetization can be transferred from A to B and vice versa via chemical exchange. This will lead to peak amplitudes;

$$a_{(A,A)}(t_m) = a_{(B,B)}(t_m) = \frac{1}{4} e^{-Rt_m}[1 + e^{-kt_m}] \tag{1.7}$$

$$a_{(A,B)}(t_m) = a_{(B,A)}(t_m) = \frac{1}{4} e^{-Rt_m}[1 - e^{-kt_m}] \tag{1.8}$$

where $a_{AA}(t_m)$ and $a_{BB}(t_m)$ are the amplitudes of the diagonal peaks, $a_{AB}(t_m)$ and $a_{BA}(t_m)$ are the amplitudes of the cross peaks in the 2D spectrum and R is the external relaxation rate.[42] For this case, the diagonal and the cross peaks have the same phase, regardless of R and t_m.

Now, let's consider the case where the solvent and solute spins can interact through dipolar interactions. The amplitude of the peaks are;

$$a_{(A,A)}(t_m) = \chi_A e^{-2R_D t_m} \tag{1.9}$$

$$a_{(B,B)}(t_m) = e^{-Rt_m} \tag{1.10}$$

$$a_{(A,B)}(t_m) = \chi_A \frac{R_D}{2R_D - R}[e^{-Rt_m} - e^{-2R_D t_m}] \tag{1.11}$$

where R_D is the rate of dipolar relaxation. In most cases $R \gg R_D$ and the cross peaks will be modulated by the leakage relaxation R. When this is the case, equation 1.11 can be represented as a ratio.

$$\frac{a_{(A,B)}(t_m)}{a_{(A,A)}(t_m)} = \frac{R_D}{R} \tag{1.12}$$

In the limit of $R \gg R_D$, diagonal peaks will have the opposite phase as the diagonal. In chapter 5, peaks resulting from chemical exchange were present in the 2D NOESY spectrum of a dye inside the CTAB reverse micelle system

This experiment yields excellent results when $\omega\tau_C \gg 1$ and $\omega\tau_C \ll 1$. But when $\omega\tau_C \approx 1$, the net NOE enhancement is zero, or very low and it is nearly impossible to generate a strong NOE cross peak. This regime is valid for molecules that have a molecular weight from about 1-3 kDa. For this case, a modification to the NOESY experiment was developed. This technique is commonly known as rotating Overhauser effect spectroscopy (ROESY) or the lesser known, “cross-relaxation appropriate for mini-molecules emulated by spin-locking” (CAMELSPIN). ROESY experiments are set up similarly to the NOE experiment, Figure 1.9. The main difference is the spin-locking in the pulse sequence.

1.3.c.iii ROESY

The advantage of ROESY is that the dependence of the NOE enhancement on $\omega\tau_c$ is different than with a traditional NOE experiment. In fact, in a ROESY experiment, the NOE enhancement does not ever cross zero and all cross peaks are positive. This is beneficial for those hard to work with molecules that have molecular weights from 1-3k Da. Most of the artifacts that are present in ROESY spectrum are opposite phase from the ROE signal, which makes interpretation of the ROESY spectrum slightly easier. However, due to the spin-locking, numerous other processes can occur during this time which can complicate the ROESY spectrum. Two other processes that are quite common are HOHAHA (Homonuclear Hartmann-Hahn effect)[40] and chemical exchange or conformation change. Both of these processes are opposite sign of that of the ROE, but can clutter the spectrum up and reduce signal from the NOE attempting to be observed. Unfortunately also, when $\omega\tau_C \gg 1$ and $\omega\tau_C \ll 1$, the NOE contribution in the ROESY experiment is less than the enhancement when doing a NOESY experiment. Despite all these drawbacks, ROESY can still be a powerful tool in conjunction with other experiments to help understand a system. In chapter 5, ROESY and NOESY are used in tandem to help interpret each other.

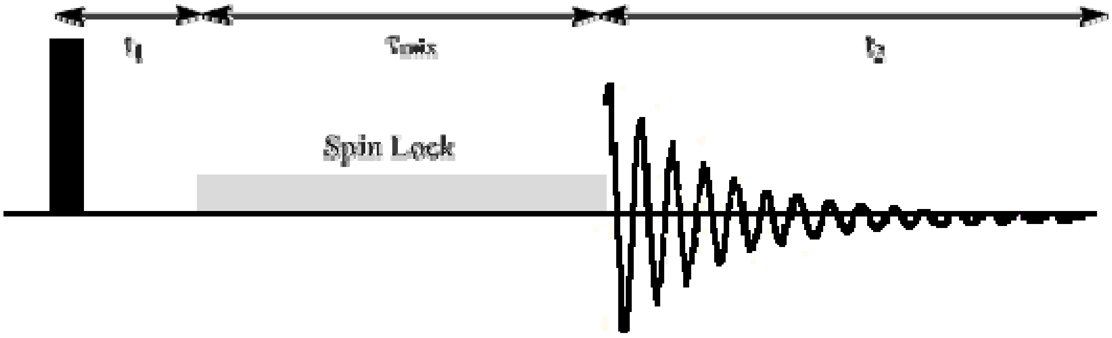

Figure 1.9 2D ROESY pulse sequence.

1.4 Probe Molecules

1.4.a Vanadium (V) Oxometalates

Vanadium is a trace element occurring naturally in approximately 65 different minerals.[43] Although vanadium exists in mineral form, it is primarily obtained as a byproduct of mining, typically from uranium based sandstones, magnetite and fossil fuel. Although vanadium can be found in trace amounts in the human body, it is unclear if it is essential or it is just beneficial.[44]

Vanadium (V) oxides have a rich speciation and protonation equilibria in aqueous solution.[39] The simple and colorless vanadate oligomers including vanadate monomer (V_1), dimer (V_2), tetramer (V_4), and pentamer (V_5), Figure 1.10, interchange with each other on the millisecond to second time scale in neutral and basic aqueous solution unlike the yellow-orange decavanadate (V10), whose interconversion with the other oligomers occurs on a substantially longer time scale.[38] Decavanadate is the thermodynamically stable vanadium species from pH = 3-6. Below pH = 2, V10 rapidly hydrolyzes to VO_2^+; although not thermodynamically the most stable form above pH = 6, decavanadate can persist for limited time periods because of its slow hydrolysis into other vanadate oligomers.[45]

The quadrupolar relaxation of vanadium makes them excellent probes for their surroundings, which can be measured by ^{51}V NMR.[39] Small changes in the coordination environment of vanadium change the ^{51}V NMR chemical shift. At pH = 3-6, decavanadate dominates the phase diagram and changes in its protonation state can be monitored. When it is full deprotonated, decavanadate has a -6 charge. As the pH of the solution increases from 3 to 6 it undergoes three protonation events. These equilibria are shown as Equations 1.7, 1.8 and 1.9.[34]

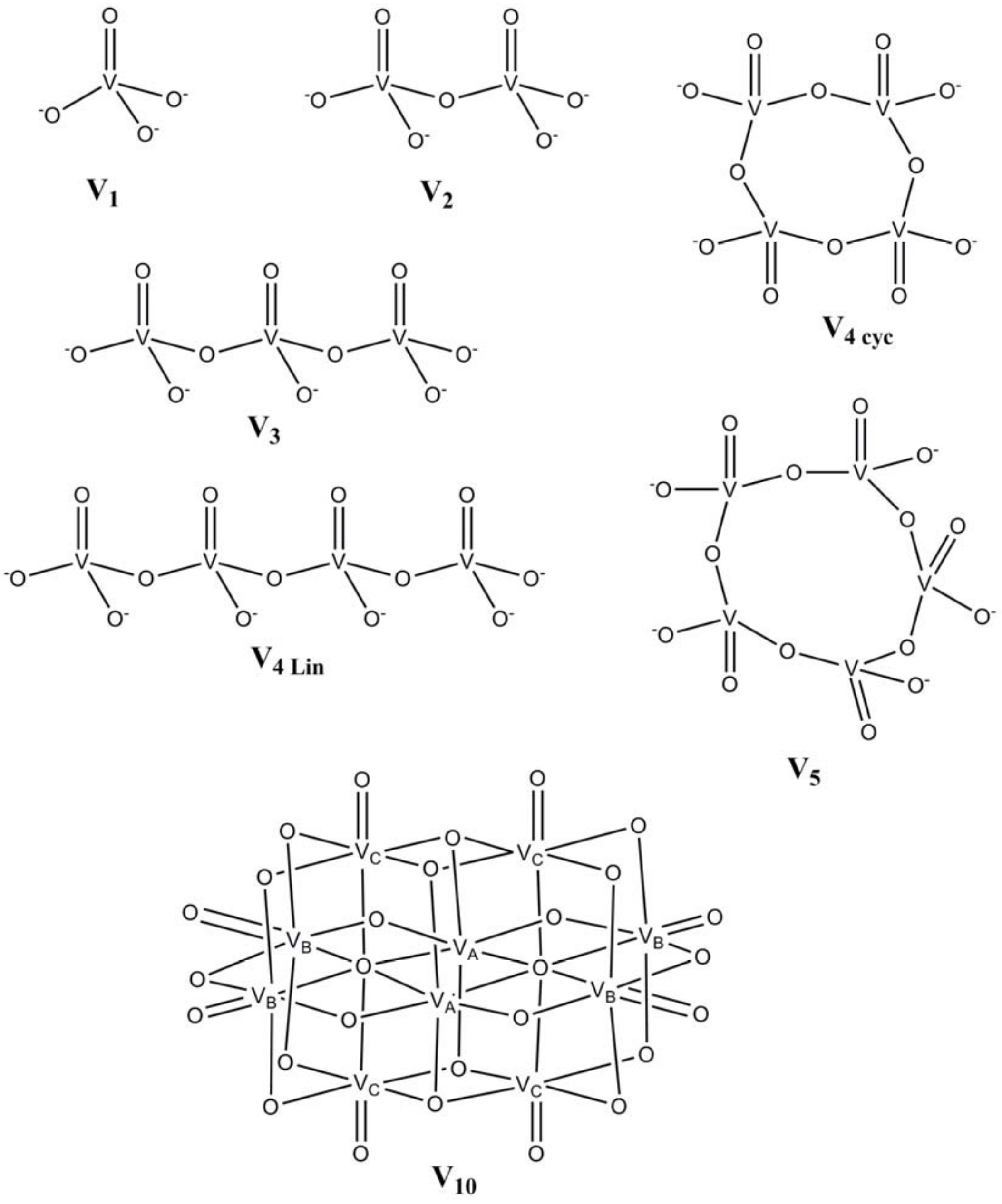

Figure 1.10 Structures of the vanadate oligomers in their ionic form. Axial (V_C), equatorial (V_B) and centrally located (V_A) vanadium atoms are labeled on the structure of decavanadate (V_{10})

$$\mathrm{V_{10}O_{28}}^{6-} + \mathrm{H}^{+} \rightleftharpoons \mathrm{HV_{10}O_{28}}^{5-} \quad \mathrm{pK_1} = 5.5 - 6.0^{45} \tag{1.7}$$

$$\mathrm{HV_{10}O_{28}}^{5-} + \mathrm{H}^{+} \rightleftharpoons \mathrm{H_2V_{10}O_{28}}^{4-} \quad \mathrm{pK_2} = 3.1 - 3.7^{45} \tag{1.8}$$

$$\mathrm{H_2V_{10}O_{28}}^{4-} + \mathrm{H}^{+} \rightleftharpoons \mathrm{H_3V_{10}O_{28}}^{3-} \quad \mathrm{pK_3} \approx 2^{45} \tag{1.9}$$

Decavanadate has 3 different types of vanadium atoms in the structure. It has four vanadium atoms in the equatorial position, four in the axial position and two embedded deep within the interior of the cluster. Successive protonation of the decavanadate leads to a downfield chemical shift for all the vanadium nuclei in decavanadate.[34] The axial and equatorial vanadium atoms display a larger shift, compared to the interior vanadium atoms, which is to be expected, because they are on the exterior of the cluster. In the work presented in chapter 3, decavanadate is used to probe the interior of the Igepal CO-520 reverse micelles and Igepal CO-430/610 reverse micelles.

1.4.b Excited-State Proton Transfer Probes

As discussed in section 1.1, understanding the environment inside the reverse micelle may lead to a better understanding of how certain processes take place in nature or in different systems. Proton transfer reactions are essential for enzymatic function[46] and how proton channels move protons across biological membranes[47]. By using 8-hydroxypyrene-1,3,6 trisulfonate, HPTS, we are able to study proton transfer dynamics inside a reverse micelle.

As a photoacid, HPTS has a drastically lower $\mathrm{pK_a}$ in the first excited state than it does in the ground state[48,49]. Spry et al. studied HPTS found proton transfer dynamics in Nafion membranes at high hydration mirrored 0.5 M HCl solution;[50] at lower hydration levels, the HPTS resides at the Nafion surface where the low local pH precluded proton dissociation. Understanding how HPTS interacts with the various types of reverse micelles will help elucidate mechanisms for proton transfers in other confined media. The experiments conducted in chapter 5 studied the excited-state proton transfer dynamics in three different types of reverse micelles.

1.5 References

(1) Luzzati, V.; Tardieu, A. *Annu. Rev. Phys. Chem.* **1974**, *25*, 79.

(2) Kunieda, H.; Shinoda, K. *J. Colliod Interface Sci.* **1978**, *70*, 577.

(3) Nave, S.; Eastoe, J.; Heenan, R. K.; Steytler, D.; Grillo, I. *Langmuir* **2000**, *16*, 8741.

(4) Falcone, R. D.; Biasutti, M. A.; Correa, N. M.; Silber, J. J.; Lissi, E.; Abuin, E. *Langmuir* **2004**, *20*, 5732.

(5) Durfor, C. N.; Bolin, R. J.; Sugasawara, R. J.; Massey, R. J.; Jacobs, J.; Schultz, P. G. *Journal of the American Chemical Society* **1988**, *110*, 8713.

(6) Menger, F. M.; Yamada, K. *Journal of the American Chemical Society* **1979**, *101*, 6731.

(7) Fendler, J. H. *Chem. Rev.* **1987**, *87*, 877.

(8) Johnson, M. D.; Lorenz, B. B.; Wilkins, P. C.; Lemons, B. G.; Baruah, B.; Lamborn, N.; Stahla, M.; Chatterjee, P. B.; Richens, D. T.; Crans, D. C. *Inorganic Chemistry* **2012**, *51*, 2757.

(9) Kumar, K. R.; Brooks, D. E. *Macromolecular Rapid Communications* **2005**, *26*, 155.

(10) Cushing, B. L.; Kolesnichenko, V. L.; O'Connor, C. J. *Chem. Rev.* **2004**, *104*, 3893.

(11) Colfen, H.; Mann, S. *Angew. Chem.-Int. Edit.* **2003**, *42*, 2350.

(12) Pileni, M. P. *Nat. Mater* **2003**, *2*, 145.

(13) Xia, Y.; Yang, P.; Sun, Y.; Wu, Y.; Mayers, B.; Gates, B.; Yin, Y.; Kim, F.; Yan, H. *Adv. Mater* **2003**, *15*, 353.

(14) Müller-Goymann, C. C. *European Journal of Pharmaceutics and Biopharmaceutics* **2004**, *58*, 343.

(15) Lawrence, M. J.; Rees, G. D. *Advanced Drug Delivery Reviews* **2000**, *45*, 89.

(16) Lawrence, M. J. *European Journal of Drug Metabolism and Pharmacokinetics* **1994**, *19*, 257.

(17) Parent, M. E.; Yang, J.; Jeon, Y.; Toney, M. F.; Zhou, Z.-L.; Henze, D. *Langmuir* **2011**, *27*, 11845.

(18) Comiskey, B.; Albert, J. D.; Yoshizawa, H.; Jacobson, J. *Nature* **1998**, *394*, 253.

(19) Sedgwick, M. A.; Crans, D. C.; Levinger, N. E. *Langmuir* **2009**, *25*, 5496.

(20) Crans, D. C.; Rithner, C. D.; Baruah, B.; Gourley, B. L.; Levinger, N. E. *J. Am. Chem. Soc.* **2006**, *128*, 4437.

(21) Levinger, N. E. *Science* **2002**, *298*, 1722.

(22) Piletic, I. R.; Moilanen, D. E.; Spry, D. B.; Levinger, N. E.; Fayer, M. D. *J. Phys. Chem A* **2006**, *110*, 4985.

(23) Schubel, D.; Ilgenfritz, G. *Langmuir* **1997**, *13*, 4246.

(24) Zhu, D. M.; Feng, K. I.; Schelly, Z. A. *J. Phys. Chem* **1992**, *96*, 2382.

(25) Palazzo, G.; Lopez, F.; Giustini, M.; Colafemmina, G.; Ceglie, A. *The Journal of Physical Chemistry B* **2003**, *107*, 1924.

(26) Shinoda, K.; Lindman, B. *Langmuir* **1987**, *3*, 135.

(27) Roberts, C. B.; Thompson, J. B. *The Journal of Physical Chemistry B* **1998**, *102*, 9074.

(28) Zhu, D. M.; Wu, X.; Schelly, Z. A. *Langmuir* **1992**, *8*, 1538.

(29) Abuin, E.; Lissi, E.; Duarte, R.; Silber, J. J.; Biasutti, M. A. *Langmuir* **2002**, *18*, 8340.

(30) Lang, J.; Jada, A.; Malliaris, A. *The Journal of Physical Chemistry* **1988**, *92*, 1946.

(31) Naoe, K.; Takeuchi, C.; Kawagoe, M.; Nagayama, K.; Imai, M. *Journal of Chromatography B* **2007**, *850*, 277.

(32) Barbero, M. C.; Valpuesta, J. M.; Rial, E.; Gurtubay, J. I. G.; Goni, F. M.; Macarulla, J. M. *Arch. Biochem. Biophys.* **1984**, *228*, 560.

(33) Zulauf, M.; Eicke, H. F. *The Journal of Physical Chemistry* **1979**, *83*, 480.

(34) Baruah, B.; Roden, J. M.; Sedgwick, M.; Correa, N. M.; Crans, D. C.; Levinger, N. E. *J. Am. Chem. Soc.* **2006**, *2006*, 12758.

(35) Berne, B. J.; Pecora, R. *Dynamic Light Scattering: With Applications to Chemistry, Biology, and Physics*; Dover Publicaitons Inc.: Mineola, NY, 2000.

(36) Harris, R. K. *Encyclopedia of Nuclear Magnetic Resonance*; John Wiley & Sons: Chichester, UK, 1996; Vol. 5.

(37) Rehder, D. *Coordination Chemistry Reviews* **2008**, *252*, 2209.

(38) Crans, D. C.; Rithner, C. D.; Theisen, L. A. *J. Am. Chem. Soc.* **1990**, *112*, 2901.

(39) Crans, D. C. *Comments Inorg. Chem.* **1994**, *16*, 1.

(40) Neuhaus, D.; Williamson, M. *The Nuclear Overhause Effect in Structure and Conformational Analysis*; VCH Publishers, Inc: New York, New York, 1989.

(41) Solomon, I. *Physical Review* **1955**, *99*, 559.

(42) Jeener, J.; Meier, B. H.; Bachmann, P.; Ernst, R. R. *J. Chem. Phys.* **1979**, *71*, 4546.

(43) Moskalyk, R. R.; A.M., A. *Minerals Engineering* **2003**, *16*, 793.

(44) Crans, D. C.; Smee, J. J.; Gaidamauskus, E.; Yang, L. *Chem. Rev.* **2004**, *104*, 849.

(45) Howarth, O. W.; Jarrold, M. *J. Chem. Soc, Dalton Trans* **1978**, 503.

(46) Michel, H.; Behr, J.; Harrenga, A.; Kannt, A. *Annu. Rev. Biophys. Biomol. Struct* **1998**, *27*, 329.

(47) Wraigh, C. A. *Biochim Biophys Acta-Bioenerg.* **2006**, *1757*, 886.

(48) Bardez, E.; Monnier, E.; Valeur, B. *J. Phys. Chem.* **1985**, *89*, 5031.

(49) Pines, E.; Huppert, D.; Agmon, N. *J. Phys. Chem* **1998**, *88*, 5620.

(50) Spry, D. B.; Fayer, M. D. *J. Phys. Chem. B* **2009**, *113*, 10210.

CHAPTER 2

EXPERIMENTAL METHODS

2.1 Sample Preparation

2.1.a Anionic Reverse Micelles

In the work presented in chapters 4 and 5 of this dissertation, Aerosol OT (sodium bis(2-ethylhexyl) sulfosuccinate) was the anionic surfactant that was used. In chapter 4, the AOT that was used was purified by dissolving a large amount (100-250g) in methanol. The amount of methanol is not important, just that there is enough methanol to dissolve all the AOT and the sample is non-viscous. After the AOT is dissolved, activated charcoal is placed in the bottom of the flask and left to sit for 24-72 hrs. After 24-72hrs, the AOT/methanol solution is vacuum filtered 2-3 times, to ensure that all the charcoal is removed. If this is not the case, the resultant purified AOT will be yellow in color and will need to be purified again. After filtration, the solution is then placed on a rotary evaporator, under vacuum at room ~35 ^{o}C, and left to fully evaporate the methanol. Once this done, the AOT is placed in a vacuum desiccator with P_2O_5. The resultant AOT was then checked for moisture by NMR spectroscopy and integrating the water peak versus one of the peaks from AOT. Typical results show about 0.1-0.2 water molecules per AOT molecule in the sample. Nonpolar solvents used for making reverse micelles are stored with molecular sieves in them to help remove the water from them as well. The AOT used in chapter 5 was used as purchased from Aldrich without further purification.

The concentration of the surfactant needs to be above a critical reverse micelle concentration (CRMC) for reverse micelles to form. While the CRMC is different from the critical micelle concentration (CMC), which is the concentration of surfactant in water to make micelles, it is commonly reported in the literature as the CMC. For AOT in isooctane, this number has been estimated to be about 10^{-3} M. To confirm the formation of reverse micelles, the samples are studied by DLS and compared to values in the literature, if available. For both cyclohexane and 1-octanol, the CRMC is not reported in the literature; the experiments conducted in chapter 4 indicate that it is below 0.1M in surfactant concentration. In AOT/isooctane, once the surfactant concentration is above 0.25M, the sample begins to form small micellar aggregates. At a high concentrations (>0.3M) and w_0 >20, the system begins to get flocculated.[1]

AOT reverse micelles are made by adding a small aliquot of water to the AOT/non-polar solvent mixtures. The range of w_0 values that can be achieved is dependent highly on the non-polar solvent. In isooctane, AOT can form reverse micelles to an upwards of $w_0 \sim 64$. In cyclohexane, $w_0 < 30$ is achievable.

2.1.b Cationic Reverse Micelles

In chapter 5, the cationic surfactant used was cetyltrimethylammonium bromide (CTAB). To be used to make reverse micelles, CTAB must first be purified by double recrystallization from an ethanol/acetone mixture. Unpurified crystals of CTAB are places in a 50:50 mixture of acetone: ethanol. This solution is heated to 40-50 ^{o}C and is stirred until all of the CTAB that will dissolve has dissolved. This solution is then filtered to remove any remaining CTAB undissolved and placed in a round bottom flask. The resultant solution is then placed in a dry ice/acetone bath at -78 ^{o}C. After cooling for a few hours, filter the remaining solution. The crystals on the filter paper are the CTAB crystals. Repeat this procedure one more time with the CTAB crystals recovered.

Unlike with AOT, CTAB does not form reverse micelles as easily. CTAB requires a co-surfactant in order to form stable reverse micelles as well as having a narrower concentration range for forming stable emulsions. The co-surfactant is typically a straight chain alcohol and for the work reported in chapter 5 we used 1-octanol. Reverse micelles solutions are made by dissolving CTAB into the non-polar solvent, usually cyclohexane. Once dissolved, the co-surfactant is added in a ratio range of 4:1 to 6:1 co-surfactant to surfactant ratio. Water is then added to make the appropriate $w_{0.}$ The CTAB/1-octanol/cyclohexane system has a w_0 range from 5 to about 20.

2.1.c Nonionic Reverse Micelles

In the work presented in chapters 3 and 5, a class of non-ionic surfactants known as Igepal was used, specifically the Igepal CO series. Unlike with AOT and CTAB, the Igepal CO series is used without further purification or drying. The Igepal CO class of surfactants also has a more limited concentration range in order to make reverse micelles. Due to the recent emergence of using Igepal as a non-ionic surfactant for making reverse micelles, it is far less characterized than that of CTAB or AOT. Reverse micelle formation is has only been demonstrated in a few organic solvents, although other systems just may have not been studied thoroughly.[2-7] Cyclohexane is most predominant non-polar solvent used for Igepal reverse micelles reported in the literature. This fact and the easy access to d_{12}-cyclohexane for NMR experiments, led us to use cyclohexane as the solvent for chapters 3 and 5 Although a specific CRMC is not currently known for Igepal CO 430, 520 or 610, 0.4M is a standard concentration reported in the literature and for this reason, all the studies in chapters 3 and 5 use this concentration. Igepal CO-520 can form reverse micelles on its own, without the use of co-surfactants, whereas Igepal CO-430 and Igepal CO-610 need a co-surfactant in order to make large w_0s ($w_0 > 8$). Typically, a mixture of both Igepal CO-430 and Igepal CO-610 are used to make a solution that is 0.4 M in total surfactant, in a 1:3 ratio of Igepal CO-610 to Igepal CO-430.

Igepal reverse micelles are made in a similar manner to AOT reverse micelles. First the surfactant is dissolved into the non-polar solvent. Since most Igepals are viscous liquids, measuring out exact quantities is hard to measure out when making small amounts of surfactant stock solution. Once the surfactant stock solution is made, aliquots of water are added to make the appropriate w_0. After adding the water, vortically mixing or sonicating the sample for about 1-3 minutes may be needed in order to make the solution transparent.

2.1.d Decavanadate Synthesis

In chapter 3, decavanadate is used to probe the interior of various Igepal CO reverse micelles. Decavanadate can be made in a variety of different ways in solution, optimizing the pH between 3 and 6.5. Two common synthesis methods are shown in equation 2.4 and 2.5. In both cases vanadate is dissolved in aqueous solution and is then acidified.

$$10\ Na_3VO_{4(aq)} + 24\ HA_{(aq)} \rightarrow Na_6V_{10}O_{28\ (aq)} \bullet 18H_2O + 24\ NaA_{(aq)} \tag{2.4}$$

$$10\ NaVO_{3(aq)} + 4\ HA_{(aq)} \rightarrow Na_6V_{10}O_{28\ (aq)} \bullet 18H_2O + 4\ NaA_{(aq)} \tag{2.5}$$

In both of these synthesis methods, there is no regard for the excess products that are generated. Typically if either of these synthesis methods is used, the decavanadate is recrystallized before use. For most the work done in the Crans and Levinger research groups[8,9], equation 2.5 is the synthesis method of choice and the decavanadate is used without further purification. This synthesis is preferential due to the near instantaneous formation of decavanadate.

However, in chapter 3, decavanadate was needed that did not have any excess counterions in solution. Even if you recrystallized the $Na_6V_{10}O_{28\,(aq)} \bullet 18H_2O$ from equations 2.4 and 2.5, if different protonation states are desired, acid would have to be added, resulting in excess ions. For this reason a slower method for making decavanadate was used. Equations 2.6, 2.7 and 2.8 show the reaction for which these decavanadates are made.[10]

$$5\ V_2O_{5\,(s)} + 3\ MOH_{(aq)} \rightarrow M_3H_3V_{10}O_{28\,(aq)} \bullet 18H_2O \qquad (2.6)$$

$$5\ V_2O_{5\,(s)} + 4\ MOH_{(aq)} \rightarrow M_4H_2V_{10}O_{28\,(aq)} \bullet 18H_2O \qquad (2.7)$$

$$5\ V_2O_{5\,(s)} + 5\ MOH_{(aq)} \rightarrow M_5H_1V_{10}O_{28\,(aq)} \bullet 18H_2O \qquad (2.8)$$

In chapter 3, decavanadate was made as described by equations 2.6-2.8. Solutions are made to have an overall decavanadate concentration of 10mM. To make a 10 mL stock solution 0.100g (err on less V_2O_5 than more, since this is already an excess) of V_2O_5 was added to volumetric flask. Assuming sodium decavanadate is the target, 0.012g (for $Na_3H_3V_{10}O_{28}$), 0.016 (for $Na_4H_2V_{10}O_{28}$) and 0.020g (for $M_5H_1V_{10}O_{28}$) of NaOH is added to the volumetric as well. Water is then added to volume. The solution is then heated at 50-60 ^{o}C for up to 168 hrs. After this time, the solution should be orange/red in color. Excess V_2O_5 is still present in the bottom of the flask. The solution is then filtered to remove the excess V_2O_5.

2.2 NMR spectroscopy

2.2.a ^{1}H NMR

^{1}H NMR experiments carried out in this dissertation we primarily done in the central instrument facility (CIF). There are 3 NMRs in the CIF that were used for various experiments. On the 7.05T (300MHz) NMR, data was collected using the "std1h" or equivalent "s2pul" pulse sequence and parameters. In both of these experiments, the pulse sequence is shown below, Figure 2.1. The delay times are labeled as d_1 and d_2. The width of the 90° pulses are labeled as pw_1 and pw_2. The acquisition time is labeled t, in which the spectrum is collected. For these experiments d_1 = 1s, $pw_1 = 0$, $d_2 = 0$, $pw_2 = 4.0$ μs, and t = 2.7 s with a sweep width (sw) set to 6000 Hz. The sweep width is area in which the data is collected, not the area in which the data is displayed. Setting pw_1 and d_2 to zero effectively removes this 90° pulse from the sequence. It is important that $t+d_1 > 5T_1$. For most protons, this sequence will satisfy that condition. For data collection, typically between 64 and 256 transients are collected and then averaged. For samples with low concentration or large couplings, up to 5120 transients have been collected.

Even though the two 9.4 T (400 MHz) NMRs in the CIF have different software, they collect their data in much the same way. Only slight variations from the std1h pulse sequence described in Figure 2.1 exist. Mainly, $pw_2 = 5.4$ μs, t = 3 s and sw =6410 Hz, all other parameters are identical.

2.2b ^{51}V NMR

^{51}V NMR presented in this dissertation were performed primarily on the 7.05T NMR (78.8MHz). Recent additions to the CIF have allowed the robotic 9.4T instrument to perform ^{51}V NMR; none of those spectra are present in this body of work. The pulse sequence for a standard

1D ^{51}V NMR experiment follow the general form illustrated in Figure 2.1. For ^{51}V NMR, pw_1, d_1, and d_2 are all set to zero where $pw_2 = 3.1$ μs and t = 95.7 ms. Because of the large area in which vanadium chemical shifts can occur, a large sweep width is utilized, sw = 83,682 Hz. Notice how small the acquisition time is, it is 95.7 ms vs 2.3 secs. This allows us to collect data for ^{51}V NMR faster than that of ^{1}H NMR. This again related to the T_1 of the nucleus of interest. Vanadium nuclei have a much faster T_1 relaxation time than most Hydrogen nuclei. Due to the quick acquisition of data, typically a few thousand transients are collected.

2.2c 2D NMR Spectroscopy

The pulse sequences for both the NOESY and ROESY experiments are detailed in chapter 1.4.c. These pulse sequences are not simple to display as the 1D experiment. Typically one NOESY pulse sequence parameters will not work ideally for a different molecule. This is mainly due to the time it takes to run a 2D experiment. Optimizing a 2D spectrum can save hours if not days of data collection. To determine the parameters used in chapter 5, first standard 1D spectrum is collected. By changing the pw_1, d_1 and t, one tries to determine the optimum settings. Typically a T_1 determination will be done as well, as saving a fraction of a second can translate to 3-4 hours of time saved over the course of the entire experiment. The mixing time is an extra parameter that can be difficult to get a handle on. Usually mixing times are chosen to be between 1 and 1000 ms, but which mixing time is better is dependent on the sample. A mixing time of 200 ms is one that works best for most of the samples presented in chapter 5. All of the specific details are discussed further in chapter 5.

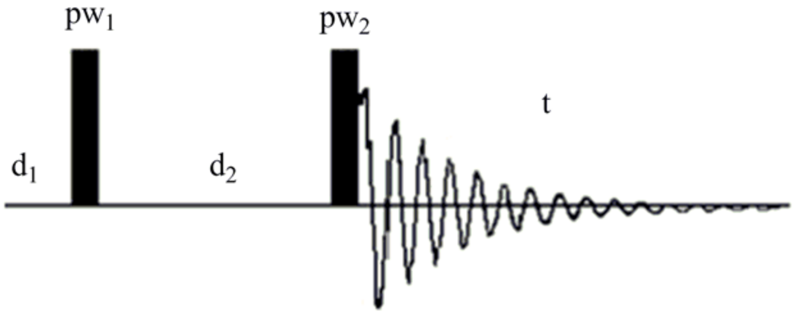

Figure 2.1 Representative 1D NMR pulse sequence. The delay times are labeled as d_1 and d_2. The width of the 90^o pulses are labeled as pw_1 and pw_2. The acquisition time is labeled t, in which the spectrum is collected.

2.3 Dynamic Light Scattering

As described in chapter 1, there are two pieces of additional information that is required before one can analyze the data from a DLS experiment. The viscosity and refractive index are needed. The viscosities and refractive indexes for the solvents used in this work are presented in Table 2.1. The viscosities and refractive indexes for the neat solvents are assumed to be similar for the reverse micelle solutions. This assumption is validated by comparing the sizes obtained from dynamic light scattering to those collected in the literature.

DLS data was acquired using a Wyatt DynaPro Titan. This instrument is interfaced to a computer and uses the program "Dynamics" to control it. Although this instrument utilizes a micro volume cuvette, so only 12 µL of sample are need to collect data, generally 1 mL of sample is required due to the strict cleaning and filtering processes needed to collect data on the instrument. Stray dust or other particles can enter the sample and wreak havoc on data collection. To prepare a reverse micelle sample for analysis, it must first be filtered through a 0.2 µm filter. This will get rid of any dust or larger aggregates in the sample. Not all samples can or need to be filtered, for instance some polymer solutions have features larger than 0.2 µm that may wish to be observed.

Before placing the sample the cuvette, a simple background measurement must be made. By placing the cuvette in the instrument with just the solvent, there should be no scattering. Any scatting that is detected considered background (should be below 1k counts). Now the sample can be placed in the instrument. Once the sample is filtered and placed the cuvette, the cuvette is placed in the instrument and left alone for about 5-10 mins so the sample can equilibrate with the

Table 2.1 Refractive Indexes and Viscosities (η) of Isooctane, Cyclohexane and Benzene.

	n_D @ ~590nm[11]	**η(cP) @ 25°C**
Isooctane	1.3915	0.473[12]
Cyclohexane	1.4232	0.98[13]
Benzene	1.501	0.607[14]

temperature of the instrument, which is default 25 ^{o}C. The laser power needs to be tuned so that it is at least 10x the background measured with the background measurement. If the laser power is too high, 500k counts or more, the detector may be overloaded. For extremely clean reverse micelle samples, there should be about 30-50k counts.

Each measurement on the DLS is a set number of acquisitions that is set by the user or 10 by default. Each acquisition is a set number of 1 second experiments set by the user, or 10 by default. Each acquisition can be individually selected and interpreted, but the individual experiments cannot. This can useful as, unless your sample is extremely clean, inevitably a piece of dust crosses the path of the laser and 1-3 acquisitions can end up having erroneous data. Once this data is collected it is fitted to Equation 1.2 and then the size of the particle(s) is displayed as a histogram. The particle sizes from the histograms are then averaged.

2.4 References

(1) Ayako Gotoa; Yasuhiro Kuwaharab; Akihiro Suzukib; Hisashi Yoshiokab; Rensuke Gotob; Tohoru Iwamotoc; Imae, T. *Journal of Molecular Liquids* **1998**, *72*, 137.

(2) Zhu, D. M.; Feng, K. I.; Schelly, Z. A. *The Journal of Physical Chemistry* **1992**, *96*, 2382.

(3) Roberts, C. B.; Thompson, J. B. *The Journal of Physical Chemistry B* **1998**, *102*, 9074.

(4) Willard, D. M.; Riter, R. E.; Levinger, N. E. *Journal of the American Chemical Society* **1998**, *120*, 4151.

(5) Cason, J. P.; Roberts, C. B. *The Journal of Physical Chemistry B* **2000**, *104*, 1217.

(6) Khougaz, K.; Gao, Z.; Eisenberg, A. *Langmuir* **1997**, *13*, 623.

(7) Abuin, E.; Lissi, E.; Duarte, R.; Silber, J. J.; Biasutti, M. A. *Langmuir* **2002**, *18*, 8340.

(8) Crans, D. C.; Rithner, C. D.; Theisen, L. A. *J. Am. Chem. Soc.* **1990**, *112*, 2901.

(9) Baruah, B.; Roden, J. M.; Sedgwick, M.; Correa, N. M.; Crans, D. C.; Levinger, N. E. *J. Am. Chem. Soc.* **2006**, *2006*, 12758.

(10) Johnson, G.; Murmann, R. K.; Deavin, R.; Griffith, W. P. *Inorganic Synthesis* **2007**, *19*, 140.

(11) *CRC Handbook of Chemistry and Physics*; Haynes, W. M., Ed.; CRC, 2012.

(12) Pádua, A. A. H.; Fareleira, J. M. N. A.; Calado, J. C. G.; Wakeham, W. A. *Journal of Chemical & Engineering Data* **1996**, *41*, 1488.

(13) Silva, A. A.; Reis, R. A.; Paredes, M. r. L. L. *Journal of Chemical & Engineering Data* **2009**, *54*, 2067.

(14) Medani, M. S.; Hasa, M. A. *Can. J. Chem. Eng* **2009**, *55*, 203.

CHAPTER 3

EXPLORING THE STRUCTURE AND PH CHARACTER OF A NONIONIC REVERSE MICELLE SYSTEM

Preface

Part of the work, the ^{51}V NMR portion, presented in this chapter has appeared as the journal article, "What's inside a nonionic reverse micelle? Probing the interior of Igepal reverse micelles using decavanadate." by Myles A. Sedgwick, Debbie C. Crans and Nancy E. Levinger, *Langmuir,* **25**, 5496-5503 (2009). ^{1}H NMR data presented in this chapter are included, but are not published in the *Langmuir* paper.

3.1 Introduction

The applications for nonionic surfactants, especially those based on poly(ethylene oxide) (PEO), are growing rapidly. Three major classes of these surfactants have received significant attention. For example, alkyl polyether surfactants (C_iE_j, Brij) find use as detergent in HPLC applications.[1] Triton X-100 is used primarily for solubilizing membrane proteins during isolation of membrane-protein complexes.[2] The class of Igepal surfactants that form the focus of the work reported here, that is nonylphenylpolyethylene oxide based surfactants, has shown broad application industrial and biochemical processes. For example, Igepal CO-520, with an average polar tail of five PEO units, finds use as an emulsifier and dispersant for universal colorants, and as a deicing fluid for aircraft.[3] With a slightly shorter PEO tail (~4 PEO units) Igepal CO-430 is used heavily as a dispersant and detergent for oil emulsion drilling, and also in cosmetics applications. With a polar tail slightly longer than Igepal CO-520 or 430 (~6-7 PEO units) Igepal CO-610 is largely used as a detergent for dry cleaning or in solvent emulsion cleaners. In nonpolar media, these surfactants have been shown to form reverse micelles (RMs), that is, isolated droplets of polar solvent, most often water, sequestered from a nonpolar solvent by an amphiphile, in this case, the nonionic surfactant.[4-8] Although the fundamental surfactant structure, an alkylated benzene with a hydrophilic PEG tail, remains the same among the various specific Igepal CO surfactants, their varied applications suggest subtle differences in properties of the Igepal CO surfactants.

Research groups have explored RM formation from the nonionic Igepal CO surfactants, in an array of nonpolar solvents.[6-17] Variability in the PEO chain length in Igepal CO surfactants leads to heterogeneity in their composition. This is one way these systems differ from ionic surfactants, such as Aerosol OT (AOT) or cetyltrimethylammonium bromide (CTAB), commonly used to form RMs. The differences in these surfactants' structures can dramatically impact the properties of the resulting microemulsions. It has been shown that mixtures of different Igepal surfactants improve the range over which RMs form.[8,18-26] To get RMs with a broad hydration range, researchers report using cosurfactants or coemulsifiers; for example the combination of Igepal CO-430 and CO-610 is very effective and can produce RM sizes not accessible from either surfactant on its own. Most of the studies focus on whether self-assembly leads to formation of micelles or RMs; although some report size and shape[9,13,15,17] and many discuss the utility of these systems for nanoparticle synthesis.[11,18,27-32] Nucleation of nanoparticles in these environments has been shown to depend on the size, shape and nature of water pool in these systems. Because the head groups of these surfactants include a PEO chain, we anticipate that this RMs may display characteristics and properties different from the much more commonly probed ionic surfactants, such as AOT (sodium di-ethylhexylsulfosuccinate). Furthermore, how the PEO segment interacts with the water will impact the nature of the RM interior.

Various properties change when the water is sequestered inside a RM; they are often designated by the parameter w_0 which is equal to the ratio of polar solvent concentration versus the surfactant concentration in the nonpolar solvent, $w_0 = [H_2O]/[\text{surfactant}]$.[33] In spherical RMs, w_0 is directly proportional to the micellar radius. Researchers have explored the characteristics of the water in several RM environments using a range of techniques.[6,9,34-48] For example, steady-state and time-resolved IR experiments suggest that intramicellar water near the interfacial region possesses structure and dynamics different from water in the core region in both RMs formed with ionic and nonionic surfactants.[6,39,44,45] Ultrafast fluorescence spectroscopy has allowed characterization of intramicellar microviscosity[49] or solvation dynamics,[9,38,47] which both show that the reverse micellar interior is hindered compared to bulk aqueous solution.

Although a substantial amount is known about the nature of water in RMs formed from ionic surfactants such as AOT, significantly less is known about the interiors of nonionic RMs. We aim to uncover fundamental information about RMs formed using nonionic surfactants to compare with RMs made from charged surfactants and understand the properties of the nonionic RMs.

A common technique for exploring the interior of RMs enlists a probe molecule solubilized within the RMs. Fluorescent probes have commonly been used to explore dynamical and equilibrium properties.[38,42,46,47,49] We have recently demonstrated the utility of oxovanadates to probe the interior of AOT RMs.[34-36] The oxovanadate anions, where the decavanadate (abbreviated V_{10}, $V_{10}O_{28}^{6-}$) has proven to be particularly useful, effectively probe the reverse micellar interior because they respond to small changes in their environment.[50] The vanadates have a well characterized speciation and protonation states that vary as a function of pH and ionic strength and that have been characterized with respect to various solution properties including pH, ionic strength, viscosity and temperature.[50] Because they are highly charged inorganic species, they reside in the intramicellar water pool.[34-36] From experiments encapsulating decavanadates with the charged AOT surfactant, we have learned that the interior of the AOT RM acts like a buffer, shifting the H^+ concentration toward neutral.[34-36] We also have seen nonviscous environments providing little resistance for movement of the probe for the interior water unless the RMs are small enough to encroach on the polyoxovanadate solvation sphere.

We use ^{51}V NMR to study the oxovanadates in RM environments.[51,52] Although the ^{51}V NMR studies using V_{10} require substantially higher concentrations of probe molecules than do corresponding fluorescence measurements such as those identified above,[38,47,49] the oxovanadates probe complementary properties of the RMs. V_{10}, whose structure is shown in Figure 1b, is the most stable vanadate oligomer at acidic pH. At slightly acidic pH, for example pH~6, the decavanadate bears a -6 charge, whereas at lower pH (~3) the decavanadate becomes di- and triprotonated giving it a -4 and -3 charge, respectively.[52,53] Equations 3.1-3.3 describe the protonation equilibria of decavanadate in aqueous solution.

$$V_{10}O_{28}^{6-} + H^+ \rightleftharpoons HV_{10}O_{28}^{5-} \qquad pK_1 = 5.5 - 6.0\ ^{54} \tag{3.1}$$

$$HV_{10}O_{28}^{5-} + H^+ \rightleftharpoons H_2V_{10}O_{28}^{4-} \qquad pK_2 = 3.1 - 3.7\ ^{54} \tag{3.2}$$

$$H_2V_{10}O_{28}^{4-} + H^+ \rightleftharpoons H_3V_{10}O_{28}^{3-} \qquad pK_3 \approx 2\ ^{54} \tag{3.3}$$

There exist three different environments that the vanadium atoms occupy in the decavanadate, four axial (V_c), four equatorial (V_b) and two buried centrally in the interior (V_a) of the complex. Each different vanadium environment in the decavanadate yields a distinct ^{51}V NMR signal.[53] For the -3 anion the ^{51}V NMR peaks appear at -525 ppm (V_c), -507 ppm (V_b), -424 ppm (V_a).[54] As the pH increases, the chemical shifts for all three vanadium sites move downfield; V_c and V_b display the most dramatic shifts by 10-15 ppm making it a very sensitive probe to H^+ concentration in the vicinity of the V_{10} molecule.

In the work reported in this chapter, we explore the interior of nonionic Igepal CO RMs using ^1H and ^{51}V NMR, with decavanadate as a probe, when appropriate. The RMs systems we have studied include the water/Igepal CO-520/cyclohexane and RMs formed using a mixture of Igepal CO-610 and Igepal CO-430 in cyclohexane. The decavanadate ^{51}V NMR line widths give insight into the structure of the interior of these RMs. Through comparison with compounds that model the headgroup region we learn that to what extent the PEO portion of the Igepal CO-520 is hydrated. Samples prepared using aqueous solutions at different starting pH demonstrate interesting dependence on acidity and basicity. Combined with a detailed comparison of similar experiments with the V_{10} probe carried out in AOT[36] these studies provide insight regarding the nature of the water pool in RMs prepared from different nonionic PEO-surfactants and AOT.

3.2 Materials and Methods

3.2.a Materials

Sodium, ammonium, and potassium metavanadate, vanadium pentoxide (V_2O_5), Igepal CO-520 (nonylphenyl ethoxylates), sodium hydroxide, potassium hydroxide, tetraethylene glycol, tetraethylene glycol monomethyl ether, ammonium hydroxide, and cyclohexane were purchased from Aldrich. Tetraethylene glycol monomethyl ether was purchased from Arcos at > 99% purity. Igepal CO-610 and Igepal CO-430 were provided by Rhodia Inc. Cyclohexane, Igepal CO-520, Igepal CO-610, and Igepal CO-430 were used without further purification. Surfactants are reported >99% pure with the major impurities being water (<0.1%) and 1,4 dioxane (<0.001%) and ethylene oxide (<0.0003%). ^{51}V NMR spectra of aqueous decavanadate spiked with 1,4 dioxane showed no impact on the spectroscopy. Deionized water was used throughout and was prepared to a specific resistivity of >18 MΩ cm (Barnstead E-pure system).

3.2.b V_{10} Solution Preparation

A series of 10.0 mM decavanadate (V_{10}) stock solutions (100 mM MVO_3, M= Na, K, NH_4^+) were prepared at a range of pH values, 3.1, 4.0, 5.0 and 6.0. V_{10} solutions were prepared using two different methods. We have prepared it by dissolving MVO_3 into water in a volumetric flask, adjusting the pH to 3.1 using 6 M HCl to form V_{10} before raising the pH to the required value using 1 M NaOH and the required volume. We have also prepared V_{10} directly from V_2O_5 to create V_{10} balanced by exactly the number of counterions necessary for charge neutrality, with no excess ions in solution, as described in detail in chapter 2.[55] A series of 10.0 mM decavanadate stock solutions (50.0 mM V_2O_5) were prepared from pH 3 to pH 6. V_{10} solutions were prepared by dissolving V_2O_5 in a basic solution, with the stoichiometry necessary to yield the desired decavanadate species. For example, to generate $HV_{10}O_{28}^{5-}$, the MOH to V_{10} ratio was 5:1. In no case did this ratio exceed 5:1. This solution was left stirring for 24-168 hrs until the V_2O_5 dissolved completely. All RMs solutions were freshly prepared. The pH values of the aqueous solutions were measured at 298 K using a pH meter (Orion 420A) calibrated with three buffers of pH 4, 7 and 10. The pH values were adjusted to within 0.05; pH variability between sample preparation and measurement was within 0.1 pH unit unless otherwise noted.

3.2. c Reverse micelle preparation and characterization

A 0.4 M surfactant stock solution was prepared for each study by dissolving the surfactant in cyclohexane as described in Chapter 2. Decavanadate V_{10}-loaded RMs of a specific w_0 value, roughly 5, 10 and 15, were prepared by pipetting a specific volume of the aqueous V_{10} stock solution at a known pH into aliquots of the Igepal stock solutions. All samples were vortexed and the resulting solutions were transparent and yellow. All measurements were performed at 298 K. Viscosity and conductivity measurements confirmed the formation of RMs by given results similar to those reported in the literature.[56]

3.2.d NMR Spectroscopy

The 1D ^{1}H spectra were recorded on a Varian INOVA-400 at 400 MHz. Routine parameters were used when collecting the ^{1}H spectra. An external reference of tetramethylsilane (TMS) was used for the ^{1}H chemical shifts. Signals were averaged at 1028 scans.

^{51}V NMR spectra were recorded using a Varian INOVA-300 spectrometer at 78.9 MHz. ^{51}V NMR spectra were acquired with a 83.6 kHz spectral window, a 60° pulse angle, and a 0.096 s acquisition time with no relaxation delay. ^{51}V chemical shifts were referenced against an external sample of VO_4^{3-}, which had been referenced against a sample of $VOCl_3$. For peak position measurements, a 15 Hz exponential line broadening was applied before Fourier transformation.[57]

3.2.e Spectral Analysis and Curve Fitting of Spectra

The NMR FIDs collected were Fourier transformed and subjected to phase correction (MestReC V. 4.5.9.1 NMR data processing software for Windows). Resulting spectral peaks were fitted to find the chemical shifts and line widths (OriginPro 8.1) of each spectral peak. Error reported is the standard deviation of the error from fits to three separate measurements.

3.2.f Hydrated Igepal and Polyethyleneglycol Monomethyl Ether

Samples mimicking the polar section of the Igepal surfactant were created with water and tetraethylene glycol monomethyl ether. Samples of hydrated Igepal surfactant (in the absence of nonpolar solvent) were also investigated. Samples were prepared by titrating the TGME or Igepal with an aqueous solution of pH 4 decavanadate solution. The decavanadate solution was added in molar equivalents of water to TGME. This procedure was also repeated using pure Igepal CO-520 (no nonpolar solvent) instead of TGME.

3.3 Results

The experiments presented here utilize the properties of V_{10} in the RMs as monitored with ^{51}V NMR to develop our understanding of the various environments inside the Igepal CO-520 and the Igepal CO-610/430 RMs. The chemical shifts of the individual V_{10} peaks are used to indicate the protonation state of the V_{10} upon encapsulation in the RMs, while the line widths indicate the local microviscosity sensed by the decavanadate molecule or its ability to tumble freely. By examining several types of PEO-containing RM systems we investigate and compare the properties of water pools in different sizes and types of RMs.

Figure 3.1 shows the ^{51}V NMR spectra of decavanadate (V_{10}) in Igepal CO-520 RMs formed with different degrees of hydration (w_0), compared to the aqueous stock solution from which the RM solutions were prepared. The three signals observed correspond to the different

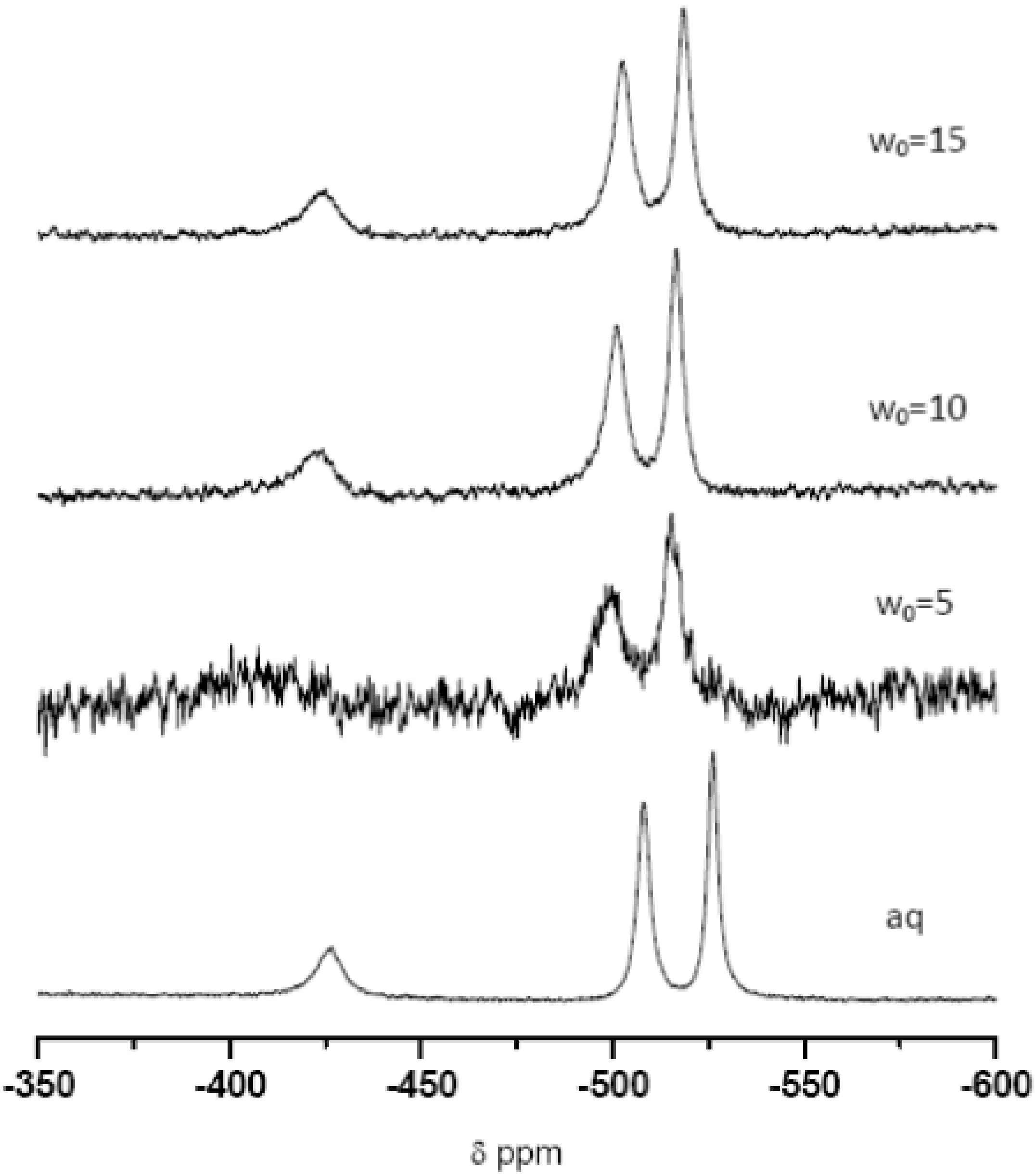

Figure 3.1 ^{51}V 78.9 MHz NMR spectra of V_{10} in Igepal CO-520 reverse micelles at different w_0 values (5-15), created from the same V_{10} stock solution, 10.0 mM V_{10} at pH=3.1. The aqueous stock solution is shown for on the bottom for comparison.

vanadium environments inside the decavanadate V_A, V_B, and V_C (see Chapter 1). The aqueous stock solution was prepared with pH = 3.1 and the spectrum of the aqueous decavanadate solution indicates the V_{10} exists primarily in a -4 charge state, consistent with this pH value (eq. 3.2). Compared to the chemical shifts in the aqueous stock solution, the V_{10} signals shift downfield in RM solutions; values for these chemical shifts are given in Table 3.1. The chemical shifts observed for V_{10} indicate deprotonation of the V_{10} upon introduction in to the RMs. The chemical shifts and line widths measured for these samples appear the same using two different methods to prepare the V_{10} (see chapter 2). Spectra of the aqueous stock solutions using the two different methods to prepare the V_{10} are shown in Figure 3.2.We also compare the line widths of the V_{10} signals inside the RM to the bulk aqueous solution; values are given in Table 3.1. Although the spectra for V_{10} in w_0 = 10 and 15, appear slightly broader compared to the stock solution, the decavanadate appears to still be able to tumble without significant hindrance. At w_0 =5 the spectrum suggests that the RM interior is beginning to impact the molecular motion of V_{10}.

In addition to exploring the interiors of Igepal CO-520 RMs as a function of hydration, we have also measured the ^{51}V NMR spectra of RM encapsulated V_{10} as a function of the pH of the starting aqueous solution. Figure 3.3 compares the ^{51}V NMR chemical shift for w_0 =10 prepared from V_{10} stock solutions with pH ~3, 4,5, and 6. Equations 3.1-3.3 demonstrate that in the pH = 4-5 range, the monoprotonated V_{10} species, $HV_{10}O_{28}^{5-}$, should predominate although at pH = 6, we should start to see evidence for the fully deprotonated species, $V_{10}O_{28}^{6-}$. Interestingly, regardless of the protonation state of V_{10} in the starting stock solution, the chemical shifts of each peak in the ^{51}V NMR spectra of the intramicellar V_{10} are experimentally indistinguishable. The observed similar chemical shifts in these spectra demonstrate that the apparent H^+

Table 3.1 ^{51}V NMR Peak Positions and Linewidths for the Three Vanadium Signals in V_{10}.

V_A

	520				610/430			
w_0	δ(ppm)	error (ppm)	Linewidth (Hz)	error (Hz)	δ(ppm)	error (ppm)	Linewidth (Hz)	error (Hz)
Stock	-425.8	0.1	619.04	17.5	-425.8	0.1	619.04	17.5
15	-423.7	0.1	817.6	19.71	-419.5	0.1	1078.21	87.6
10	-421.7	0.1	810.3	21.1	-418.9	0.1	1204.5	*
5	-407.4	1.1	7292.7	744.6	-419.4	0.1	1627.9	*

V_B

	520				610/430			
w_0	δ(ppm)	error (ppm)	Linewidth (Hz)	error (Hz)	δ(ppm)	error (ppm)	Linewidth (Hz)	error (Hz)
Stock	-508.6	0.1	282.5	12.5	-508.6	0.2	282.5	12.5
15	-502.5	0.1	421.2	14.6	-501.5	0.2	889.9	58.4
10	-500.8	0.1	434.4	15.4	-501.1	0.2	1070.1	55.2
5	-499.2	0.1	668	13.9	-502.3	0.2	948.2	49.6

V_C

	520				610/430			
w_0	δ(ppm)	error (ppm)	Linewidth (Hz)	error (Hz)	δ(ppm)	error (ppm)	Linewidth (Hz)	error (Hz)
Stock	-526.1	0.1	230.7	16.4	-526.1	0.3	230.7	16.4
15	-518.4	0.1	327.0	21.9	-517.9	0.3	440.2	21.9
10	-516.4	0.1	310.5	19.2	-517.2	0.3	557.0	22.4
5	-515.4	0.1	407.3	17.8	-518.1	0.3	510.3	19.7

All reverse micelles were formed from an aqueous stock solution of V_{10} at pH=3.1. δ is the chemical shift. * = No error could be estimated for these measurements.

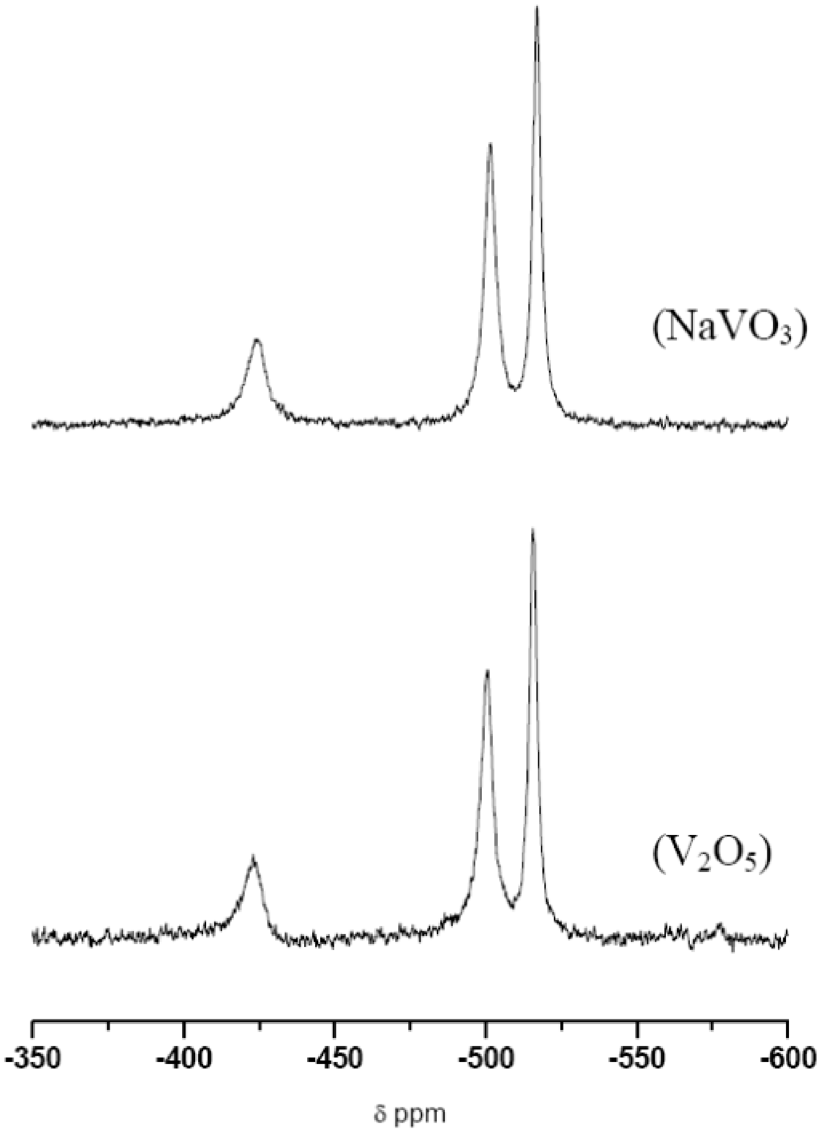

Figure 3.2 ^{51}V NMR (78.9 MHz) spectra of two aqueous stock solutions of decavanadate, one made from vanadium (V) pentoxide (V_2O_5) and the other made from sodium metavanadate ($NaVO_3$). For most of the work provided in this chapter, the decavanadate used was made from V_2O_5 to ensure that there are no excess counter ions present in solution.

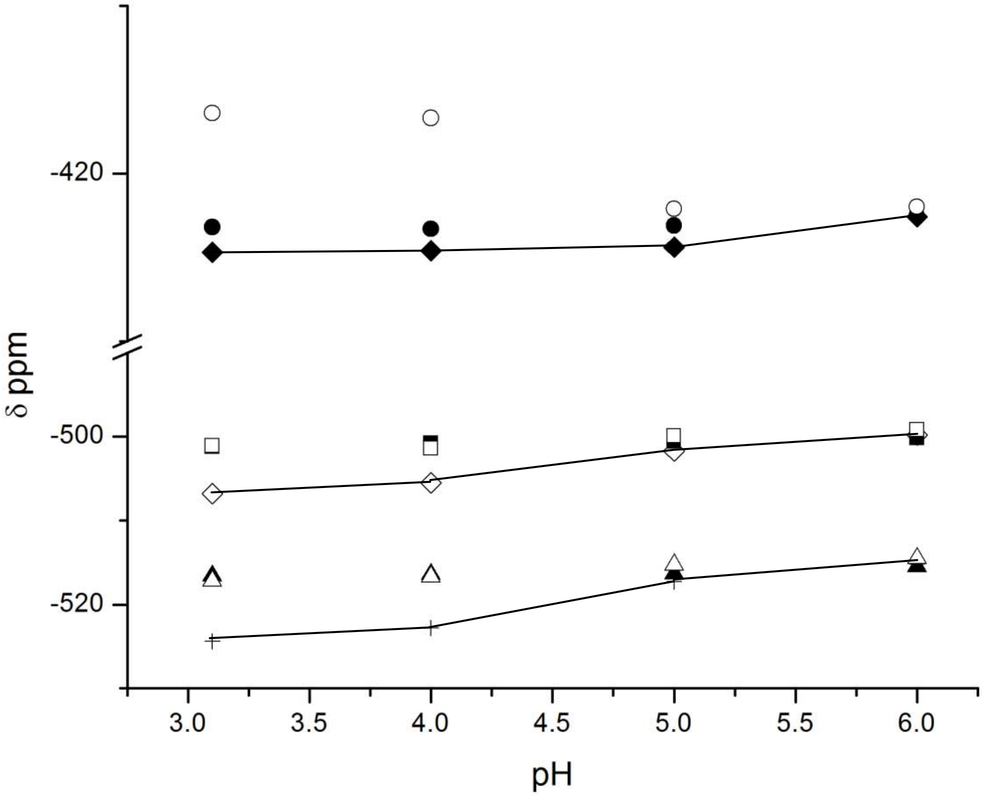

Figure 3.3 The chemical shift of the three V_{10} peaks in w_0 = 10 reverse micelles are shown as a function of solution pH; Igepal CO-520 (● V_A, ■ V_B, ▲ V_C) and Igepal CO 610/430 (○ V_A, □ V_B, △ V_C) RM solutions. The chemical shifts for the V_{10} in aqueous stock solutions are indicted by ◆ V_A, ◇ V_B and + V_C with connecting lines to guide the eye.

concentration within the RMs remains essentially unchanged despite the different starting protonation state for the V_{10} in the aqueous stock solutions. Furthermore, the chemical shifts observed correspond to the deprotonated V_{10} species, that is $V_{10}O_{28}^{6-}$.[50-53] Also, the clear and sharp peaks indicate that the V_{10} molecule's environment is sufficiently unrestrictive to allow it to sample a range of environments on the time scale of the measurement, that is, it can tumble reasonably freely. This observation suggests that the V_{10} resides in a well-defined, bulk-like water pool in the Igepal CO-520 RMs but the environment favors the fully deprotonated V_{10} species.

In contrast to the results for Igepal CO-520 RM solutions, ^{51}V NMR spectra of a V_{10} in Igepal CO-610/430 RMs, shown in Figure 3.4, as a function of w_0, appear broader, more substantially impacted by the environment. Specifically, the line widths of the peaks in the V_{10} spectra are noticeably broader that those in the Igepal CO-520 RMs, especially in the V_B peak. We have fitted the line widths and the values for them are presented in Table 3.1. The line widths differ less as a function of w_0 within the Igepal CO 610/430 RM series than the differences observed between the Igepal CO-520 RMs and the mixed micelles. This suggests that the Igepal CO-610/430 RMs restrict the V_{10} molecule much more than the environment in the Igepal CO-520 RMs. At the same time, the chemical shifts are consistent with deprotonation of $H_2V_{10}O_{28}^{4-}$ and $H_3V_{10}O_{28}^{3-}$ in these confined environments.[50-53]

Figure 3.3 displays the chemical shifts in the ^{51}V NMR of V_{10} in the Igepal CO-520 and in the Igepal CO 610/430 RM solutions as s function of the pH of the stock solution. We observe little change for the chemical shifts as a function of pH for the Igepal CO-520 RM solutions, whereas some change is observed for the V_A vanadium atom for the Igepal CO

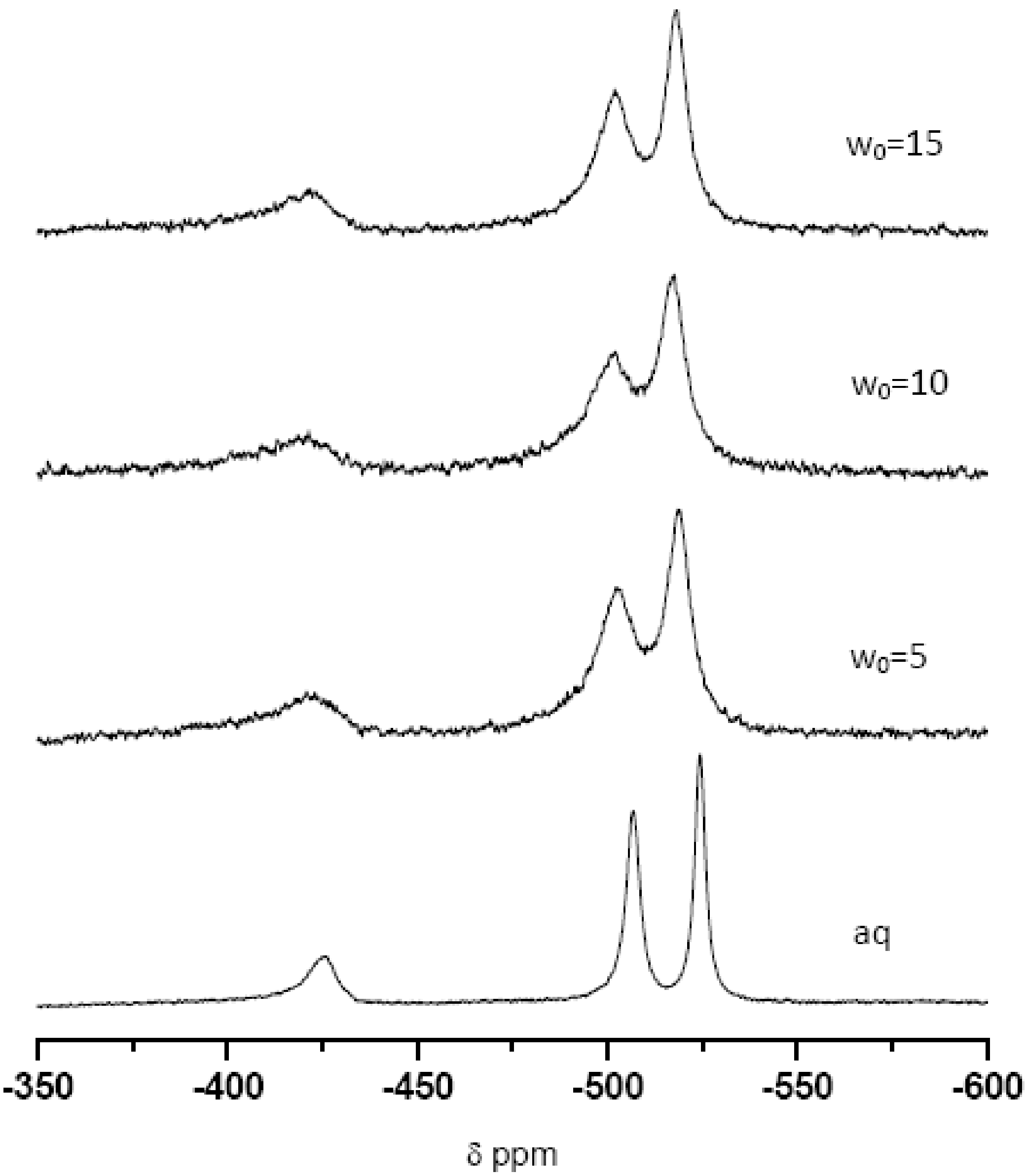

Figure 3.4 ^{51}V 78.9 MHz NMR spectra of V_{10} in Igepal CO-610/430 mixed reverse micelles at different w_0 values (5-15), created from the same V_{10} stock solution, 10.0 mM V_{10} at pH=3.1. The aqueous stock solution is shown on the bottom for comparison.

610/430 RM when acidic stock solution was introduced to the micelles. The divergence of the chemical shifts for V_A at low pH values shown in Figures 3.1, 3.3 and 3.4 indicates that the proton is significantly differently solvated in these two systems, despite the inherent similarity between these three PEO-based surfactants.

Attempts to prepare the RMs from ternary solutions of water/Igepal CO-430 or CO-610/ and aqueous decavanadate solution were not successful. Reports of microemulsions formed with these surfactants have appeared in the literature,[8,18,27] and we were able to prepare small RMs encapsulating V_{10}. However, when we attempted to prepare larger RMs, w_0 = 5 to 15, with aqueous decavanadate solution, the microemulsions did not emulsify and in several samples precipitation occurred.

To provide another comparison point for the RM solutions, we recorded ^{51}V NMR spectra of V_{10} in model PEO solutions with molar ratios of 4:1 H_2O:TGME, 4:1 H_2O:Igepal CO-520 for comparison to w_0 = 4 Igepal RM in cyclohexane. The spectra are shown in Figure 3.5. Here, we note that the signals are substantially broader in the hydrated model systems than they appear in the RM samples. This suggests that the V_{10} molecule is less mobile in the model samples than it is in the actual RMs. This indicates that a “true water pool” forms in the RMs in contrast to the model systems where the water interacts substantially with the PEO ether oxygen atoms. By analogy, these results also suggest that the water in the RM samples exists largely as a water pool and not fully hydrating the PEO chains.

These systems were then investigated using ^1H NMR, in the absence of decavanadate. Figure 3.6 displays the representative ^1H NMR spectra for an Igepal CO-520 reverse micelle (w_0 = 3), as well as hydrated TEG and TGME, two compounds modeling the headgroups of Igepal CO-520; each sample includes 3:1(water: surfactant) molar equivalents of water. The peak

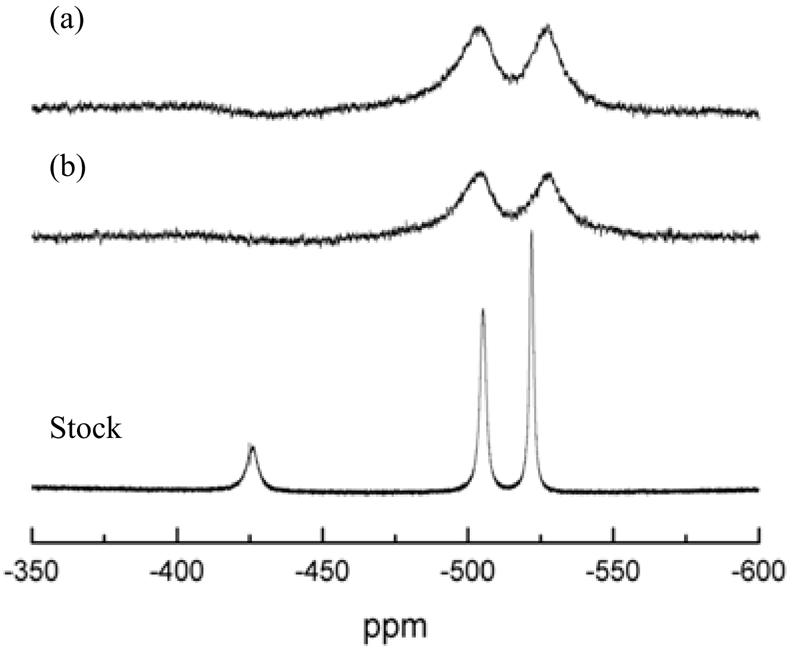

Figure 3.5 ^{51}V 78.9 MHz NMR spectra of V_{10} in the presence of 4:1 (a) hydrated TGME and (b) hydrated Igepal CO-520.

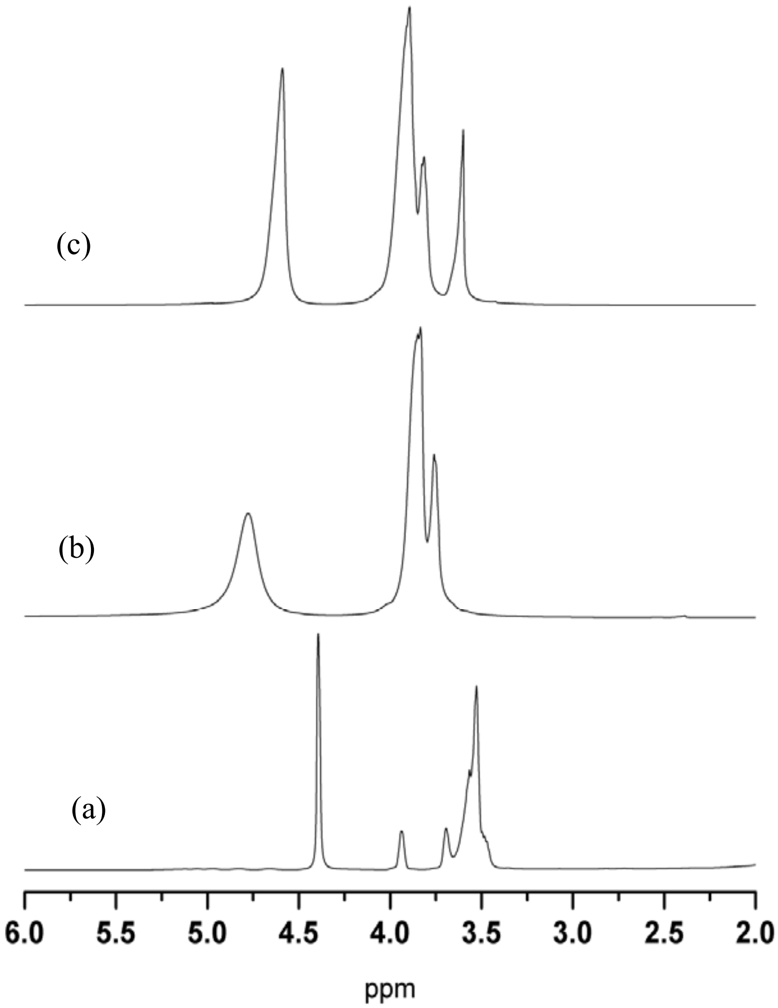

Figure 3.6 ^{1}H NMR spectra of a) w_0=3 Igepal CO-520 reverse micelle and of the hydration (3:1 water: surfactant) of two model headgroups, b) tetraethylene glycol and c) tertaethylene glycol monomethyl ether. The water peaks linewidths and chemical shifts are shifted downfield from that of the Igepal CO-520 w0=3 RM. The polyethylene oxide peaks are also shifted downfield and are broadened significantly, indicating that they are hydrated. The sharpness of peaks in the Igepal CO-520 reverse micelle indicates minimal hydration of the polyethylene oxide head groups.

appearing in the range from 4.3 ppm -5.0 ppm reflects water in the system. Signals shown in Figure 3.6 arising from the TEG and TGME samples are significantly broader and are shifted downfield compared to their counterparts in the Igepal CO-520 reverse micelle samples. With increasing water content, the TEG and TGME ^{1}H NMR spectra become increasingly broad; at mole ratios above 3:1 the samples are so viscous that the ^{1}H NMR peaks become exceedingly broad and challenging to detect. Conversely as shown in Figure 3.2, the Igepal CO-520 reverse micelle signals display only minimal broadening with increasing water content.

We also explored the role of pH on the interior of the nonionic reverse micelles. We measured ^{1}H NMR signals in Igepal CO-520 reverse micelle samples prepared with stock solutions of varying pH from 5 to 13. Figure 3.7 shows the water peak in these ^{1}H NMR spectra for samples in which w_0=10. Between pH 5 and 9, the ^{1}H NMR signal associated with water displays increasing downfield shifts. At higher pH values above 9, the spectra shift back upfield, to chemical shift values smaller than the signal at pH=5. More noticeably spectra reveal a significant splitting of the signal, to the point where two semi-resolved peaks appear at pH 13.

3.4 Discussion

Several findings are worth noting in the data presented and are summarized as follows. First, the Igepal CO-520 RMs form a distinct water pool akin to those found in RMs formed by ionic surfactants such as AOT. Second, the properties of the water pool and the interaction of water with the surfactant marking the interface varies significantly with the specific Igepal surfactant and/or mixture. Third, the proton concentration for a pH-sensitive probe in the water

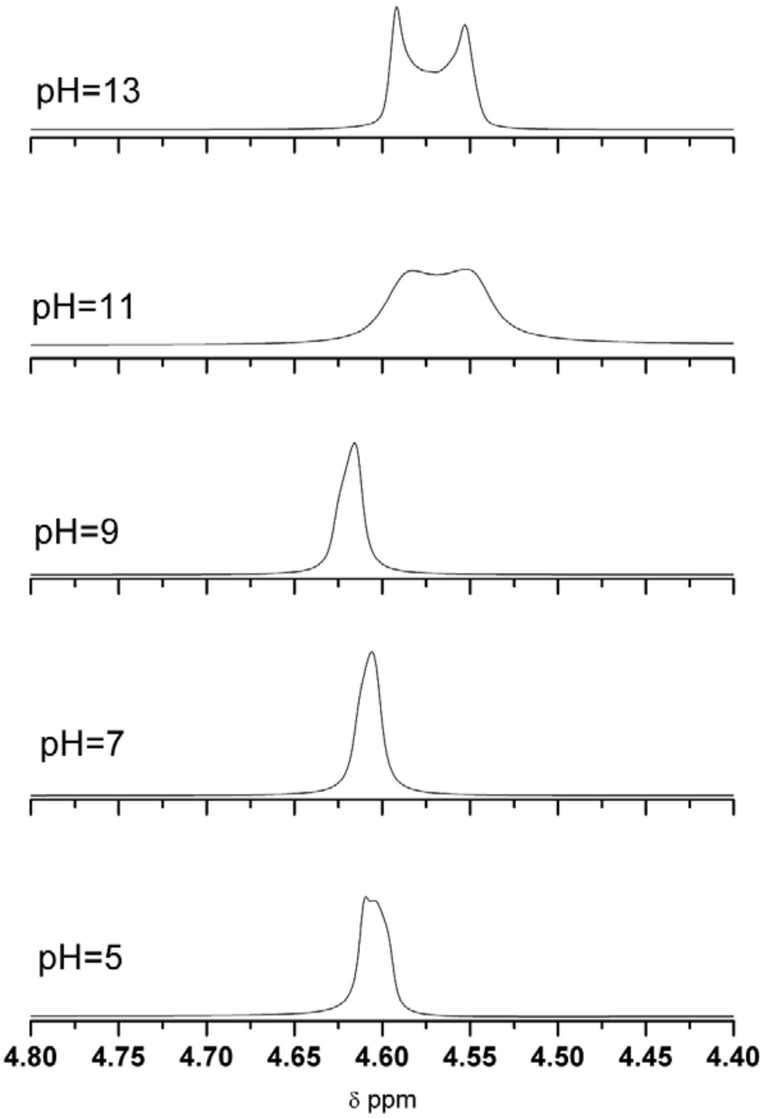

Figure 3.7 ^{1}H NMR spectra of Igepal CO-520 reverse micelles w_0=10 with varying pH of the water added to the samples.

pool reflects a neutral pH regardless of the pH used for preparation of the RMs. The details in the discussion of these findings follow.

The ^{51}V NMR linewidth results show that V_{10} in the Igepal CO-520 RMs moves quite freely. This is somewhat surprising given that the polar head group of the Igepal surfactant is a PEO chain that could be at least partially if not completely hydrated. In Igepal CO-520 the PEO chain is, on average, five PEO units long. Given that each PEO ether oxygen can accept up to two hydrogen bonds with water,[58] the Igepal CO-520 PEO segment should be able to accommodate 10 hydrogen bonded water molecules. Thus, if each PEO oxygen were completely hydrated, then the interior of RMs with $w_0 \leq 10$ should present a hydrated polymer solution rather than a pool of water, as found in RMs formed from ionic surfactants like AOT.[33,39,47] A hydrated PEO solution should present a highly viscous environment[59] that would prevent the V_{10} from tumbling freely as the ^{51}V NMR spectra indicate as shown in figure 3.6. TGME and TEG were studied and compared to hydrated Igepal (no organic solvent) to see the effect a viscous environment would have on the V_{10}. This kind of viscous environment indeed exists in the hydrated Igepal and model TGME/TEG solutions, where we observe substantially broadened peaks compared to bulk aqueous solution or in the RMs. The sharp signals in the ^{51}V NMR spectra of V_{10} in Igepal CO-520 RMs demonstrate that the V_{10} senses a relatively nonviscous environment, which indicates the existence of a water pool solvating the intramicellar V_{10} formed inside the RMs rather than a hydrated PEO solution as one might expect. The formation of a non-viscous water pool is further confirmed by the ^{1}H NMR signals for the head group of Igepal CO-520 in a reverse micelle and when it is hydrated. The existence of a well-formed water pool has previously been postulated for Igepal and other nonionic reverse micellar systems.[17,40] For example, from small angle neutron scattering studies, Lipgens, et al. observed a water pool formed in Igepal RMs.[17] In addition, the common surfactant Triton X-100 has been observed to form water droplets at hydration levels as low as $w_0 = 2.5$.[40] Our observations from ^{51}V NMR studies of V_{10} support the interpretation that the water pools in Igepal CO-520 RMs are well defined similar to those observed in Triton X-100[40] and AOT-RMs.[34-36]

To identify a hydrated PEO if it dominated the interior of the Igepal CO-520 inside the RMs, we have explored two model systems. We have dissolved a V_{10} solution into TGME/water mixtures (Figure 3.5). We have also measured ^{51}V NMR spectra of V_{10} in solutions containing water in Igepal CO-520 without the nonpolar solvent, that is, solutions of hydrated surfactant with no RM formation (Figure 3.5). In these solutions the viscosity of the samples increased substantially with added water indicating that the water hydrates the ether oxygens.[60] The ^{51}V NMR spectra of the TGME and aqueous Igepal solutions shown in Figure 3.5 display a completely different response to the environment found in the RM solutions; specifically V_{10} spectra appear dramatically broadened corresponding to a highly immobilized environment as does the ^{1}H of the PEO units. If the water in the RMs hydrated the PEO tails of the Igepal surfactant, then we would expect to observe similar spectral broadening for the V_{10} in the Igepal CO-520 RMs as in the case for the polyether and hydrated Igepal solutions. The sharp V_{10} signals in the ^{51}V NMR spectra acquired in RM samples is consistent with the molecule being in a well formed and bulk-like water pool.

Although the environment inside the Igepal CO-520 allows the V_{10} to move with relative ease, the interior of RMs formed from a mixture of Igepal CO-610 and Igepal CO-430 presents a significantly more restrictive environment. This is evident from the increased line width of the ^{51}V NMR spectra for V_{10} in the mixed surfactant micelle environment; see Figure 3.4 and Table 3.1. We have created RMs from a mixture of Igepal CO 520 and Igepal 610 and observed broader spectral lines indicating a more “viscous” interior in this environment. We hypothesize that the a mismatch of the polyethylene oxide tails of the Igepal CO 610, with an average 6.5 PEO repeat units and the CO 430, with an average 3 repeat units, allows some of the longer PEO tails to protrude from the shorter tails These longer PEO portions interact with water forming hydrogen bonds that increase the local viscosity and thus imposes a more restricted environment on the V_{10}. This interpretation is consistent with observed line width increases in mixed Igepal CO-520/610 RMs where the longer PEO portion on Igepal CO-520 leads to less protrusion of the Igepal CO-610 tails.

We did not anticipate that the results would vary so much between the different Igepal CO surfactant RM systems. As a result, we explored whether the results could be due to impurities in the surfactant systems. However, ^{1}H NMR shows no evidence of impurities in the surfactants themselves. Furthermore, our past studies have shown that the presence of small amounts of an additional component in the RM did not yield differences of the magnitude shown in these studies.[61,62] We suggest that these observed differences may reflect the subtle differences in the utilities of these surfactants.

Because hydration of PEO is very facile, it seems logical that the polar PEO portion of the Igepal surfactants would be well hydrated by the intramicellar water. However, our results for Igepal CO-520 RMs suggest that the PEO moieties remain relatively free from water. Small angle neutron scattering studies of Igepal CO-520 RMs reveal that the surfactant shell that delineates the inner water pool from the nonpolar continuous phase is thinner than the length of the fully extended Igepal CO-520 molecule, suggesting that the molecules comprising the RM surface adopt a structure more compact than the "all trans" configuration. Previous studies have shown that PEO can adopt a helical structure in which water molecules bridge between ether oxygens.[63] It is possible that the level of PEO hydration impacts the properties of the intramicellar water pool. Results from our ^{51}V NMR studies described here confirm that there is a distinct water pool for the Igepal CO 520, as the V_{10} appears to tumble freely. However, as we show, this result is not obtained with the Igepal CO 610/430 mixed RMs.

We observe significant differences in the line widths for V_{10} in Igepal CO-520 and the mixed Igepal CO-610/430 RMs (Figures 3.1 and 3.3, Table 3.1). Specifically, linewidths are broader in the mixed system. As noted above, RMs do not form in ternary solutions using pure Igepal CO-610 or Igepal CO-430; we find RM formation only for the mixed surfactant system. In both systems the line widths decrease with increasing w_0. We have seen similar trends for V_{10} in anionic AOT RMs.[36] In the Igepal CO-520 RMs, the interior reflects a viscosity much like bulk water, allowing the V_{10} to tumble freely, as depicted in Figure 3.8a and observed previously in AOT RMs.[36] In contrast, the RMs formed from the mixture of Igepal CO-610 and 430 presents a more viscous environment, as represented in Figure 3.8b where the gray shading indicates volume occupied by PEO moieties while white indicates the aqueous water pool.

One intriguing result of this research is observation of the deprotonation of the V_{10} inside the Igepal CO RMs. We have observed this effect in RMs formed from surfactants with ionic head groups, like AOT.[34-36] In those cases, we rationalized that the sodium counter cations to the AOT surfactant could exchange with protons from the V_{10}. But in the Igepal CO RMs, there are no such counterions available to exchange with the H^+. However, V_{10} prepared using $NaVO_3$ includes an excess of Na^+ ions in solution. To explore whether these counterions are necessary for the observed apparent pH change around the V_{10}, we have prepared the V_{10} by carefully titrating a V_2O_5 solution with NaOH.[55] This synthetic approach leaves only counterions required to balance the V_{10} charge and no excess ions. If excess ions present from the $NaVO_3$ synthesis

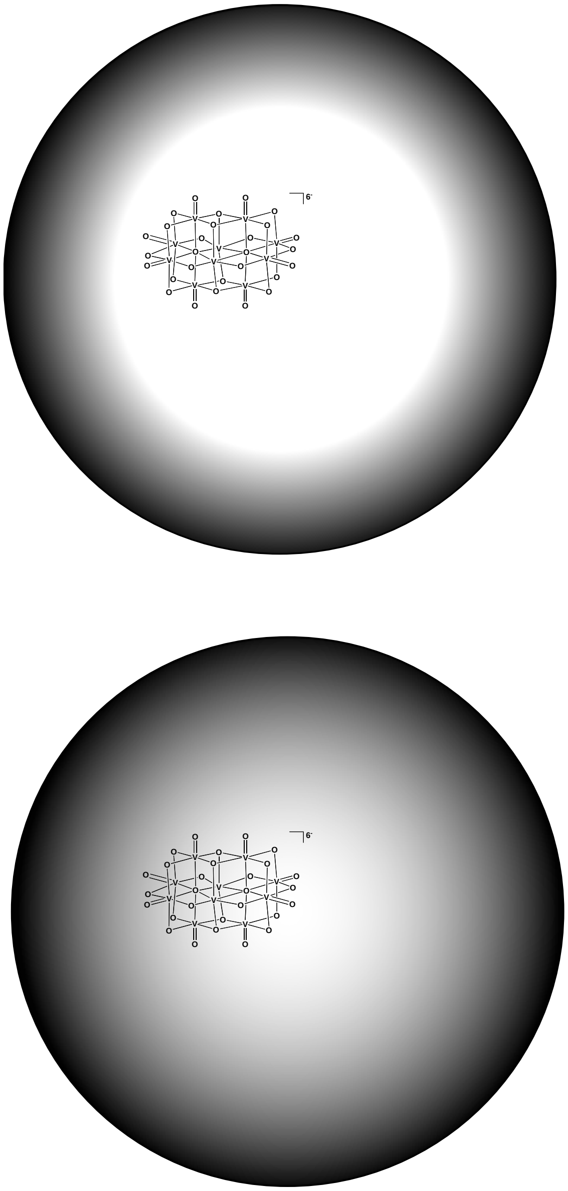

Figure 3.8 A schematic representation of the reverse micelle environment investigated here. Gray indicates the volume where polyethylene oxide tails reside; white indicates an aqueous environment. In the Igepal CO-520 reverse micelles (top) the V_{10} molecule senses a relatively nonviscous aqueous environment compared to the Igepal CO-610/430 mixture (bottom) where more hydration of the surfactant polyethylene oxide.

were facilitating the deprotonation inside the RM, we should detect a difference in the chemical shifts for the V_{10} prepared from V_2O_5. However the ^{51}V NMR spectra of V_{10} in the Igepal CO-520 RMs reveal identical chemical shifts and line widths regardless of sample preparation method (spectra of stock solutions and RM are shown in supporting information). Thus, we cannot attribute the V_{10} deprotonation to counterions motion in this system. However, subtle differences are observed for the chemical shifts of the V_A atom in the V_{10} whether it is found in the Igepal CO-520 or in the Igepal CO-610/430. Interestingly, the V_A is found to change with pH in the Igepal CO-610/430 consistent with the interpretation that in the mixed system, the PEO-units are more solvated and thus more sensitive to changes when the V_{10} is at least somewhat protonated.

The conundrum that $H_2V_{10}O_{28}^{4-}$ loses two protons in a RM where there are no excess cations remains a surprising finding, Figure 3.4. It is not clear what driving force exists for the proton to dissociate from the $H_2V_{10}O_{28}^{4-}$ in the RMs and remain dissociated from the anion. For the Igepal CO-520 acidic H^+ concentrations are observed regardless of the pH of the starting solution, whereas for the Igepal CO 610/430 RM solutions the situation is slightly more complex in that the internal vanadium atoms show evidence that they are more like those observed in aqueous solution at the highest H^+ concentrations. Once dissociated from the $H_2V_{10}O_{28}^{4-}$, the H^+ cannot escape from the RMs into the nonpolar solvent; thus they must reside in the water pool or at the RM interface, most likely interacting with the surfactant ether oxygen atoms. Experiments probing aqueous surfaces report the propensity for H^+ to preferentially reside at interfaces.[64-66] Calculations of water droplets have demonstrated migration of H_3O^+ to the surface where it is stabilized with the H_3O^+ oxygen facing away from other water molecules to accommodate its partial positive charge. Although the pH in a RM is not the same as the pH in aqueous solution, these considerations suggest that it is unlikely that the protons dissociated from V_{10} protonate the Igepal ether oxygen atoms because the aqueous stock solution of $H_2V_{10}O_{28}^{4-}$ used to form the RMs was pH~4.

Several factors may be important for stabilizing the deprotonated V_{10} molecules. First, if the dissociated proton is stabilized at the interface, then its entropic contribution to ΔG could favor it remaining dissociated. Second, at pH >5, there is an enthalpic advantage to deprotonating V_{10}.[67] Our previous work suggests a buffer-like effect of the AOT RM[36] interior which could be important for the nonionic Igepal CO-520 studied here. Taken together, these two effects can account for the observed proton dissociation from V_{10}. In addition, considering Debye-Huckel theory allows us to estimate the distance between ions in a solution. Although Debye-Huckel theory is most appropriate for low concentration solutions of ions with low charge, we can use the theory to get a rough estimate for the interior of the RMs.[68] For the unprotonated $V_{10}O_{28}^{6-}$ ion balanced by six monovalent ions (either Na^+ or H^+) we estimate that the anion and cations are separated by at least 0.45 nm. When the anion is reduced to $H_2V_{10}O_{28}^{4-}$ with four monovalent ions, then the separation increases to almost 0.7 nm. Although the interiors of the RMs are quite small, Lipgens et al. report the inner water core of radius is 2.7 nm for w_0 = 10 water/Igepal CO-520/hexane RMs,[17] thus the RM water pool is substantially larger than the Debye length. In bulk aqueous solution, ions would reside in dynamic equilibrium with the central anion. However in the minuscule confined geometry of the RM interior, as soon as a counterion moves away from the central solvation sphere, its environment may differ enough to provide a driving force for it to move to the interface. Furthermore, experiments probing Igepal micelles in aqueous solution show that small ions partition effectively into the PEO layer.[10] This suggests that the majority of the positively charged counterions, including the protons, could be found at the interface. The results presented here suggest that any positively charged counterions, including the acidic protons that dissociate from the originally introduced $H_2V_{10}O_{28}^{4-}$ ion, would reside at the inner surface of the RMs. This too could lead to preferential adsorption of protons at the micelles' inner surfaces.

3.5 Conclusion

Here we report results from studies using V_{10} as a probe for the interior of the selected Igepal CO RMs and 1H NMR results for systems devoid of V_{10}. In the Igepal CO-520 RMs, there is a well-defined water pool, mostly free from the PEO head groups of the Igepal CO-520. In the mixed Igepal CO 610/430 RMs, there is more interaction of the water pool with the Igepal head groups. This is inferred from the signal broadening in the mixed surfactant RMs, which indicates the inability of the V_{10} to tumble freely. Sharp spectral lines observed for V_{10} in the Igepal CO-520 RMs shows that V_{10} moves essentially without restriction in this environment and that the V_{10} is not solvated by the hydrated PEO headgroups, which also have sharp spectral lines, of the Igepal. Results from these studies differ substantially from the RMs that form from Igepal CO-430 or Igepal CO-610 that are too small to contain a V_{10} molecule. These studies underline the dramatic differences between the Igepal RMs and suggest that the structure of RM water pool varies because of the differences in hydration of the PEO tails. These studies also allow comparison between the water pools in different nonionic RM systems and with the ionic AOT RMs we have studied previously.[34-36]

The placement of protonated V_{10} in RMs created from Igepal surprisingly yielded spectra consistent with deprotonated V_{10} with regard to the V_B and V_C atoms. Similar results were previously obtained using the V_{10} probe in a negatively charged AOT RM system,[36] and the observation attributed to a proton gradient that allows exchange of the protons at the AOT surface with the Na^+ associated with V_{10}. The deprotonation result in Igepal CO-520 RMs was unexpected, because we prepared some of these RMs with no excess counter ions present with V_{10} in the water pool. Thus, a gradient in which other ions balance the increased charge on the deprotonated V_{10} is not possible. Indeed, the lack of variation between spectra collected with excess or no excess of counterions downplays the role of the ions in the deprotonation event. A noticeable difference between the Igepal CO-520 and Igepal CO-610/430 is however, the changes in V_A at low pH. Interestingly, the vanadium atom that is showing differences is the non-oxo vanadium atom, which is the broadest signal and only indirectly sensitive to the vanadium atoms that are protonated at low pH. This observation underline the subtle solvation differences that exist between these RMs. Importantly, the nonionic Igepal RMs appear to have contributions to ΔG and V_{10} that apparently favor deprotonation, but some differences in solvation is taking place.

3.6 References

(1) Karsa, D. R.; Houston, J. In *Chemistry and Technology of Surfactants*; Farn, R. J., Ed.; Blackwell Publishing Ltd: Oxford, 2007, p 1-23.

(2) Barbero, M. C.; Valpuesta, J. M.; Rial, E.; Gurtubay, J. I. G.; Goni, F. M.; Macarulla, J. M. *Arch. Biochem. Biophys.* **1984**, *228*, 560-568.

(3) Rhodia, personal communication.

(4) Fleischer, G.; Gratz, K.; Karger, J.; Meyer, H. W.; Quitzsch, K. *J. Colloid Interface Sci.* **1997**, *190*, 9-16.

(5) Gratz, K.; Helmstedt, M.; Meyer, H. W.; Quitzsch, K. *Colloid Polym. Sci.* **1998**, *276*, 131-137.

(6) Moilanen, D. E.; Levinger, N. E.; Spry, D. B.; Fayer, M. D. *J. Am. Chem. Soc.* **2007**, *129*, 14311-14318.

(7) Paul, B. K.; Mitra, R. K. *J. Colloid Interface Sci.* **2005**, *288*, 261-279.

(8) Michaels, M. A.; Sherwood, S.; Kidwell, M.; Allsbrook, M. J.; Morrison, S. A.; Rutan, S. C.; Carpenter, E. E. *J. Colloid Interface Sci.* **2007**, *311*, 70-76.

(9) Ghosh, S. K.; Khatua, P. K.; Bhattacharya, S. C. *J. Colliod Interface Sci.* **2004**, *279*, 523-532.

(10) Ghosh, S. K.; Khatua, P. K.; Ghosh, J. K.; Bhattacharya, S. C. *Spectrochim. Acta A.* **2005**, *61*, 395-401.

(11) Bae, D. S.; Kim, E. J.; Bang, J. H.; Kim, S. W.; Han, K. S.; Lee, J. K.; Kim, B. I.; Adair, J. H. *Met. Mater. Int.* **2005**, *11*, 291-294.

(12) Mitra, R. K.; Paul, B. K. *Colloids Surf. A.* **2005**, *252*, 243-259.

(13) Novoa, A. F.; Quiben, J.; LizMarzan, L. M. *Colloid Polym. Sci.* **1996**, *274*, 239-244.

(14) Park, S.; Moilanen, D. E.; Fayer, M. D. *J Phys Chem B* **2008**, *112*, 5279-5290.

(15) Schlicht, L.; Spilgies, J. H.; Runge, F.; Lipgens, S.; Boye, S.; Schubel, D.; Ilgenfritz, G.-. *Biophys.Chem.* **1996**, *58*, 39-52.

(16) Schomacker, R.; Orlich, B.; Braun, G. *Ber. Bunsen-Ges. Phys. Chem. Chem. Phys.* **1997**, *101*, 1695-1698.

(17) Lipgens, S.; Schubel, D.; Schlicht, L.; Spilgies, J. H.; Ilgenfritz, G.; Eastoe, J.; Heenan, R. K. *Langmuir* **1998**, *14*, 1041-1049.

(18) Chang, C. L.; Fogler, H. S. *Langmuir* **1997**, *13*, 3295-3307.

(19) Zhong, Q.; Steinhurst, D. A.; Carpenter, E. E.; Owrutsky, J. C. *Langmuir* **2002**, *18*, 7401-7408.

(20) Morrison, S. A.; Cahill, C. L.; Carpenter, E. E.; Calvin, S.; Harris, V. G. *J. Nanosci. Nanotechnol.* **2005**, *5*, 1323-1344.

(21) Ghosh, S. K.; Khatua, P. K.; Bhattacharya, S. C. *Int. J. Mol. Sci.* **2003**, *4*, 562-571.

(22) Rosen, M. J.; Zhou, Q. *Langmuir* **2001**, *17*, 3532-3537.

(23) Lim, G. K.; Wang, J.; Ng, S. C.; Gan, L. M. *Langmuir* **1999**, *15*, 7472-7477.

(24) Gan, L. M.; Liu, B.; Chew, C. H.; Xu, S. J.; Chua, S. J.; Loy, G. L.; Xu, G. Q. *Langmuir* **1997**, *13*, 6427-6431.

(25) Lim, G. K.; Wang, J.; Ng, S. C.; Chew, C. H.; Gan, L. M. *Biomaterials* **1997**, *18*, 1433-1439.

(26) Luisi, P. L.; Giomini, M.; Pileni, M. P.; Robinson, B. H. *Biochim. Biophys. Acta* **1988**, *947*, 209-246.

(27) Bagwe, R. P.; Mishra, B. K.; Khliar, K. C. *J. Dispersion Sci. Technol.* **1999**, *20*, 1569-1579.

(28) Bellezza, F.; Cipiciani, A.; Costantino, U.; Marmottini, F.; Quotadamo, M. A. *Colloid and Poly. Sci.* **2006**, *285*, 19-25.

(29) Carr, C. S.; Shantz, D. F. *Chemistry Mater*. **2005**, *17*, 6192-6197.

(30) Nanni, A.; Dei, L. G. *Langmuir* **2003**, *19*, 933-938.

(31) Zhang, D. B.; Qi, L. M.; Cheng, H. M.; Ma, J. M. *Chin. Chem. Lett.* **2003**, *14*, 100-103.

(32) Zhang, D. B.; Qi, L. M.; Ma, J. M.; Cheng, H. M. *J. Mater. Chem.* **2002**, *12*, 3677-3680.

(33) De, T. K.; Maitra, A. *Adv. Colloid Interface Sci.* **1995**, *59*, 95-193.

(34) Baruah, B.; Crans, D. C.; Levinger, N. E. *Langmuir* **2007**, *23*, 6510-6518.

(35) Baruah, B.; Swafford, L. A.; Crans, D. C.; Levinger, N. E. *J Phys Chem B* **2008**, *112*, 10158-10164.

(36) Baruah, B.; Roden, J. M.; Sedgwick, M.; Correa, N. M.; Crans, D. C.; Levinger, N. E. *J. Am. Chem. Soc.* **2006**, *128*, 12758-12765.

(37) Harpham, M. R.; Ladanyi, B. M.; Levinger, N. E.; Herwig, K. W. *J. Chem. Phys.* **2004**, *121*, 7855-7868.

(38) Riter, R. E.; Willard, D. M.; Levinger, N. E. *J. Phys. Chem. B* **1998**, *102*, 2705-2714.

(39) Piletic, I. R.; Moilanen, D. E.; Spry, D. B.; Levinger, N. E.; Fayer, M. D. *J. Phys. Chem. A* **2006**, *110*, 4985-4999.

(40) Zhu, D. M.; Wu, X.; Schelly, Z. A. *J. Phys. Chem.* **1992**, *96*, 7121-7126.

(41) Vasilescu, M.; Caragheorgheopol, A.; Almgren, M.; Brown, W.; Alsins, J.; Johannsson, R. *Langmuir* **1995**, *11*, 2893-2898.

(42) Pant, D.; Levinger, N. E. *Langmuir* **2000**, *16*, 10123-10130.

(43) Hasegawa, M.; Sugimura, T.; Shindo, Y.; Kitahara, A. *Colloids and Surf. A* **1996**, *109*, 305-318.

(44) Dokter, A. M.; Woutersen, S.; Bakker, H. J. *Proc. Natl. Acad. Sci. U.S.A.* **2006**, *103*, 15355-15358.

(45) Cringus, D.; Lindner, J.; Milder, M. T. W.; Pshenichnikov, M. S.; Vohringer, P.; Wiersma, D. A.-. *Chem. Phys. Lett.* **2005**, *408*, 162-168.

(46) Correa, N. M.; Biasutti, M. A.; Silber, J. J. *J. Colloid Interface Sci.* **1996**, *184*, 570-578.

(47) Bhattacharyya, K. *Accounts Chem. Res.* **2003**, *36*, 95-101.

(48) Bandula, R.; Vasilescu, M.; Lemmetyinen, H. *J. Colloid Interface Sci.* **2005**, *287*, 671-677.

(49) Hasegawa, R.; Sugimura, T.; Suzaki, Y.; Shindo, Y.; Kitahara, A. *J. Phys. Chem.* **1994**, *98*, 2120-2124.

(50) Crans, D. C. *Comments Inorg. Chem.* **1994**, *16*, 1-33.

(51) Pettersson, L.; Andersson, I.; Hedman, B. *Chem. Scrip.* **1985**, *25*, 309-317.

(52) Pettersson, L.; Hedman, B.; Andersson, I.; Ingri, N. *Chem. Scrip.* **1983**, *22*, 254-264.

(53) Crans, D. C.; Smee, J. J.; Gaidamauskas, E.; Yang, L. Q. *Chem. Rev.* **2004**, *104*, 849-902.

(54) Howarth, O. W. *Prog. NMR Spectrosc.* **1990**, *22*, 453-483.

(55) Crans, D. C.; Shin, P. K. *Inorg. Chem* **1988**, *27*, 1797-1806.

(56) Guo, R.; Zhang, X. H.; Liu, T. Q. *Acta Phys.-Chim. Sin.* **1999**, *15*, 319-326.

(57) Elvingston, K.; Crans, D. C.; Petterson, L. *J. Am. Chem. Soc.* **1997**, *119*, 7005-70121.

(58) Kjellander, R.; Florin, E. *J. Chem. Soc.-Faraday Trans. I* **1981**, *77*, 2053-&.

(59) Gonzaleztello, P.; Camacho, F.; Blazquez, G. *J. Chem. Eng. Data* **1994**, *39*, 611-614.

(60) Tontiwachwuthikul, P.; Chakma, A. *J. Chem. Eng. Data* **2005**, *50*, 734-734.

(61) Roess, D. A.; Smith, S. M. L.; Winter, P.; Zhou, J.; Dou, P.; Baruah, B.; Trujillo, A. M.; Levinger, N. E.; Yang, X. D.; Barisas, B. G.; Crans, D. C. *Chem. Biodivers.* **2008**, *5*, 1558-1570.

(62) Stover, J.; Rithner, C. D.; Inafuku, R. A.; Crans, D. C.; Levinger, N. E. *Langmuir* **2005**, *21*, 6250-6258.

(63) Tasaki, K. *J. Am. Chem. Soc.* **1996**, *118*, 8459-8469.

(64) Petersen, M. K.; Iyengar, S. S.; Day, T. J. F.; Voth, G. A. *J. Phys. Chem. B* **2004**, *108*, 14804-14806.

(65) Petersen, P. B.; Saykally, R. J. *J. Phys. Chem. B* **2005**, *109*, 7976-7980.

(66) Petersen, P. B.; Saykally, R. J. *Annu. Rev. Phys. Chem.* **2006**, *57*, 333-364.

(67) Cruywagen, J. J. In *Adv. Inorg. Chem.*; Sykes, A. G., Ed.; Elsevier: 1999; Vol. 4, p 136-140.

(68) Robinson, R. A.; Stokes, R. H. *Electrolyte solutions*; Dover Publications: Mineola NY, 2002.

CHAPTER 4

COEXISTING AGGREGATES IN MIXED AEROSOL OT AND CHOLESTEROL MICROEMULSIONS

Preface

The work presented in this chapter has appeared as the journal article, " Coexisting cholesterol aggregates in AOT microemulsions" by Myles Sedgwick, Alejandro M. Trujillo, Noah Hendricks, Nancy E. Levinger, and Debbie C. Crans, *Langmuir,* **27**, 948-54 (2011). Alejandro M. Trujillo and Noah Hendricks both contributed to this work. Mr. Trujillo performed cholesterol NMR experiments presented in this work, as well as a 2D NOESY experiments that are mentioned, but not shown. Mr. Hendricks performed preliminary dynamic light scattering experiments on the cholesterol/AOT emulsion system. All the remaining work presented and data analysis were performed by Myles Sedgwick.

4.1 Introduction

Cholesterol is a key component of cellular membranes with crucial roles in metabolism and membrane fluidity of living systems. This molecule is tightly regulated in biological systems and a critical constituent of membrane microdomains serving as signal transduction platforms.[1-5] Cholesterol's interaction in membrane systems has been investigated both experimentally and theoretically.[6-11] Given the complex nature of cellular membranes, researchers often use simplified models to probe the molecular interactions of cholesterol. Recent applications also illustrate the utility of cholesterol as a targeting agent for administration of chemotherapeutics such as cisplatin (Lipoplatin)[12-14] and anti-inflammatory agents such as cyclosporin (Neoral) currently used in clinical treatments of several cancers.[15-17] The systems discussed here provide fundamental experimental information on the types of structures that form in complex media, which remain very important and may impact the understanding of how cholesterol acts in many life-science related systems.

Microemulsions, which form from mixtures of chemical components that often include fractions that are normally immiscible with each other, represent a simplified system often invoked for model studies of molecular interactions. Using a surfactant, a microemulsion can stabilize water in a nonpolar solvent.[18,19] Depending on the nature and the proportions of the components, various different phases can exist in the microemulsions,[20,21] such as bicontinuous sponge phases, hexagonal phases, micelles and reverse micelles. The reverse micelle phase typically forms in ternary solutions of surfactants sequestering water from a nonpolar phase[19,22-27] but can also include a wide range of other components that enhance emulsification by adding to the polar phase, nonpolar phase or to the interface between the polar and nonpolar phases.[25,26,28-34] Microemulsions have been used in a wide range of drug delivery applications,[12,17,35-37] recently including delivery of anti-cancer agents and anti-inflammatory agents.[12,14,15,17] Well-known drugs such as cisplatin have gained new life in novel microemulsion formulations.[12] Cholesterol has successfully been used as a targeting agent in microemulsions; [38-40] these applications, in addition to the fundamental action of cholesterol in signal transduction in membranes, underline the importance of understanding the types of structures formed in unconventional media.

The precise location of a particular molecule added to a microemulsion can sometimes be hard to predict and often is not determined. For example, many researchers expect ionic probes to remain solvated in the reverse micelle aqueous phase simply because of the molecule's net charge. We have recently shown that charged ionic probes that are very water soluble can partition deeply into the interfacial region of reverse micelles.[26,41] The properties of these systems are sensitive to many components, including concentration of surfactant, pH, temperature, and amount of polar solvent added.[21,42-44] Adding other components can lead to changes in the microemulsion characteristics as the newly added component interacts with the self-assembled molecules that comprise the complex structure.[45,46] For example, in the phosphatidylcholine microemulsions systems described by Formariz et al., the addition of the solute, Doxorubicin, changes the size and shape of the structures formed.[47]

The surfactant AOT, sodium di-ethylhexylsulfosuccinate, Figure 4.1, has been used to form reverse micelles in a vast range of different systems, which have been characterized using many different techniques.[19,21,22,25,26,48-57] Generally, the size of these self-assembled reverse micelles follows a Poisson distribution centered around the thermodynamically favored compositionally distinct fundamental unit. At high surfactant concentrations, researchers observe flocculation, percolation and aggregation of reverse micelles into larger structures.[58] However, even in these systems, research shows formation of single compositionally distinct fundamental units in these solutions. Solutions containing coexisting self-assembled particles with differing sizes were proposed by Rack et al. to explain experimental observations, but the authors provided no direct evidence supporting the existence of two differently sized particles in their solutions.[59] The possibility for two distinct self-assembled structures of similar energy to form in a single macroscopic phase in the same region of the phase diagram is rare, particularly

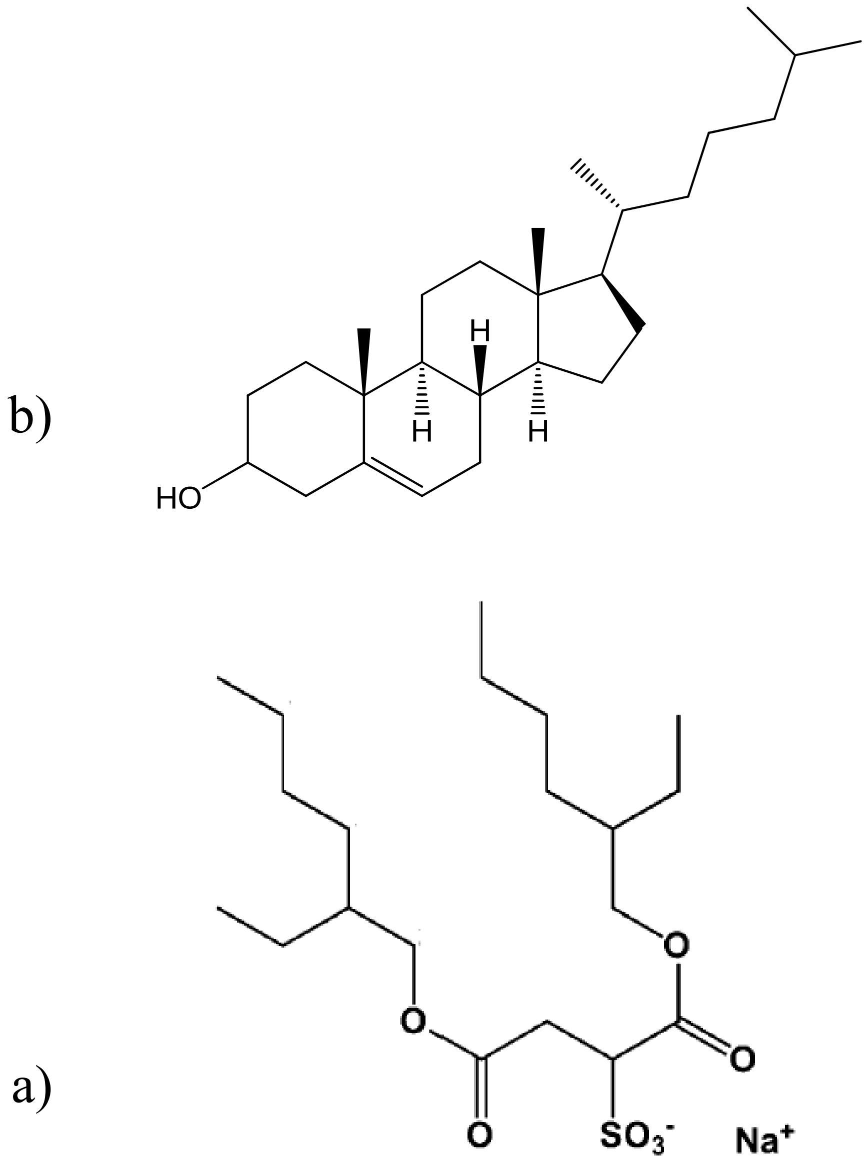

Figure 4.1 a) Structure of Aerosol-OT (AOT). b) Structure of cholesterol.

considering the high propensity of AOT to self-aggregate and form highly stable reverse micelles. As a result the potential number of molecules capable of competing with AOT to form structures of similar stability is very limited.

The importance of cholesterol interactions with lipids has encouraged researchers to explore its interactions in AOT microemulsions and controversy exists regarding its location.[22,54,55,60] Most of the data in the literature suggests that when cholesterol is added to a microemulsion solution, it associates with the AOT reverse micelles. Using ^{13}C NMR NOE experiments, Maitra found that cholesterol embeds in the interface of AOT reverse micelles.[22] Destree' used AOT reverse micelles to make cholesterol nanoparticles, and these studies inferred that cholesterol is solubilized in the water pool.[54] Chattopadhyay and Kelker used a fluorescent probe and found that cholesterol was located in the interior of the interface in the AOT reverse micelle system.[55] Evidence has been reported showing changes in ^{1}H NMR chemical shifts of cholesterol in the AOT reverse micelle system,[60] although this was corrected upon subsequent in-depth studies.[61] Because the precise location of cholesterol in the microemulsion varies with samples, given the diversity in the literature description of the AOT/cholesterol (AOT/cholesterol) system, direct evidence is needed for a fundamental understanding of how cholesterol interacts in AOT microemulsions.

In the research reported here, we have characterized the behavior of cholesterol added to various reverse micelle solutions formed with the commonly used surfactant, AOT. The experiments were designed to explore the interaction of cholesterol in a microemulsion system and probe the nature of the interaction between cholesterol and AOT using dynamic light scattering (DLS), NMR spectroscopy and other routine characterization techniques for microemulsions. We have investigated the impact of a wide range of differing parameters on the particle size obtained from DLS measurements. In contrast to literature reports,[22,54,55] our results indicate that cholesterol does not add to AOT assemblies, forming a homogenous membrane like structure. Instead, cholesterol forms submicellar aggregates in solution coexisting in solution with pure AOT reverse micelles. These findings represent a significant departure from previously reported structures. In addition, we present experimental proof-of-concept demonstrating the coexistence of two compositionally different self-assembled particles in solution.

4.2 Experimental Methods

4.2.a Materials

Sodium bis(2-ethylhexyl)sulfosuccinate (98%, Aerosol OT, AOT), cholesterol (98%, chol), isooctane (99%),cyclohexane (99%), DMSO (99%) and d12-cyclohexane(99%), and deuterated chloroform (99%, $CDCl_3$) were all obtained from Sigma Aldrich. All chemicals were used without further purification except AOT which was purified using previously described techniques.[49] Dryness and purity of AOT was confirmed by ^1H NMR analysis.[49] Doubly distilled water was used for all reverse micelle systems.

4.2.b Solution Preparation

Stock solutions of AOT were prepared by dissolving purified AOT in cyclohexane to make a 100 mM solution. Studies were also performed with isooctane with similar result, however the data presented here reflect samples prepared from cyclohexane. Aliquots of these stock solutions were used to make individual reverse micelle solutions. For cholesterol containing solutions, solid cholesterol and solid AOT were dissolved together in the nonpolar solvent simultaneously, before the addition of water.

Samples were prepared with AOT concentrations ranging from 10^{-4} to 1 M in cyclohexane. All samples used were optically transparent. Samples were prepared for various hydrations, w_0= [water]/ [AOT] values from 4 to 20, by dissolving the appropriate amount of water, by mass, into each AOT solution. These samples were used in DLS analysis to determine reverse micelle size, percolation effects, and to compare to sizes reported in the literature.[19]

Reverse micelles stock solutions were prepared in two different ways. One way was to prepare solutions from a stock solution of AOT and Cholesterol solid and the other way was to use codissolve solid AOT and solid cholesterol to volume by adding cyclohexane. Samples with AOT:cholesterol ratios of 6:1, 5:1, 4:1, 3:1 and 2:1 were prepared. All stock AOT solutions were made at 100 mM and the appropriate amount of cholesterol was added to each solution, as a solid, to form the ratios listed above. Samples with ratios of AOT:cholesterol were attempted at 1:1, 1:2, and 1:3, but these samples were not homogenous nor optically transparent. Increasing /decreasing the overall AOT concentration did not alleviate the sample issues and thus was concluded the ratios in which there is more cholesterol than AOT are unachievable in this system. All samples used, for the data reported here, were homogeneous at all ratios and optically transparent. A range of reverse micelles with varying w_0 sizes from w_0=4 to 32, were made using the 4:1 ratio of AOT:cholesterol. These systems were analyzed using both ^{1}H NMR and DLS and generated sizes consistent with literature values.[19,62]

4.2.c Characterization: Dynamic Light Scattering

Characteristics of the various solutions were measured using dynamic light scattering (DLS, Wyatt DynaPro Titan). To obtain effective data requires intensities of 10^5-10^6 counts, we varied the instrument's GaAs laser power between 10 and 20 percent; scattered light was collected at 90°. Prior to data acquisition, samples were equilibrated in the DLS instrument for

10 min at 25°C. Each measurement consisted of a minimum of 10 runs, each of which is a set number of scans. Scans were performed at a rate of 10 acquisitions for 100 seconds.

To obtain valid results from DLS measurements requires knowledge of the system's refractive index, n_i and viscosity, η, in addition to well-defined conditions. The refractive indices for the AOT RM solutions were assumed to be the same as neat organic solvent used .[63,64] Viscosities were measured for a range of AOT RM solutions and AOT stock solutions was determined to be about 1.04 cP. Figure 4.2 shows the size of the reverse micelles as a function of AOT concentration. All of these data were analyzed using this viscosity. Because the size of the RMs does not change as a function of concentration, and is consistent with the literature values, it was determined that the assertion to use the measured viscosity is appropriate. Cleanliness of the cuvettes used for measurements was of paramount importance for obtaining reliable and reproducible data. Cuvettes were cleaned in a 3:1 ratio of ammonium hydroxide: hydrogen peroxide base bath solution and rinsed with doubly distilled water then dried with MeOH before use. Before introducing each sample to the cuvette, it was rinsed with pure isooctane twice, then with the 100 mM AOT stock solution and finally with the sample to be analyzed. The sample was then filtered directly into the cuvette through a 0.2 μm filter as needed. Prior to making measurements on a given day, the background signal from air, water and a standard Triton X-100 solution[65] were collected to confirm cleanliness of the cuvettes. At the end of each day cuvettes were cleaned with a Pihrana solution and a “cuvette cleaner” (Starna Cells Inc.) solution.

The DLS instrument generated correlation functions from scattering of particles in solution. Typically, we use the DynaPro DYNAMICS software (ver. 6.7.3) assuming a spherical form for the particles to evaluate the light scattering data. The DYNAMICS ver. 6.7.3 analyzes the autocorrelation to regulated fits and a cumulant fit, which is an average of the regulated fits.

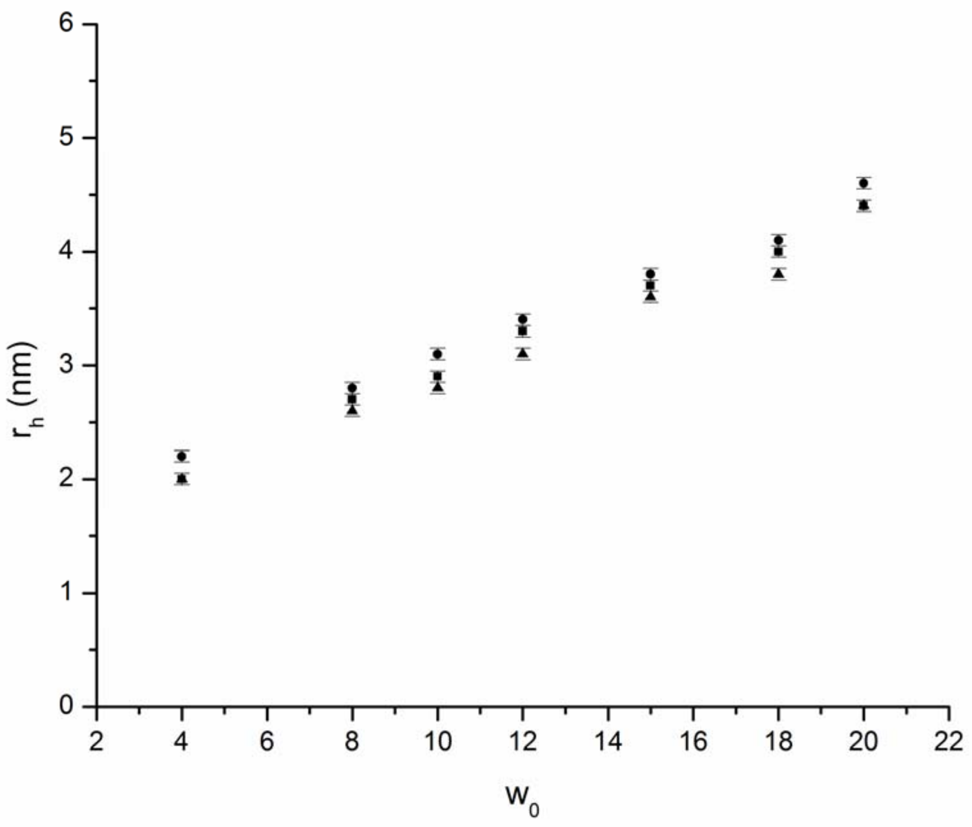

Figure 4.2 Hydrodynamic radius, r_h, of AOT reverse micelles as a function of w_0 for various continuous bulk solvents, AOT (200mM)/cyclohexane (circles), AOT (200mM)/1-octanol (squares), AOT(200mM)/d_{12}-cyclohexane (triangles). Error bars represent standard deviation of the particle sizes measured by dynamic light scattering.

We find that data extracted from the regulated fit and analyzed in Origin Pro v 8.1 provides more reliable sensitivity to correlation features associated with the particles in solution than using the DYNAMICS software. Based on our exponential fits to the data, we obtain reverse micelle size with a 10% instrument error. The reproducibilities of the experiments are reported with standard deviation.

4.2.d Characterization: NMR Spectroscopy and Other Supporting Methods

Solutions were also characterized using ^{1}H NMR spectroscopy. Water content in the AOT surfactant was determined by dispersing the surfactant in DMSO. Aggregation of AOT in protonated and deuterated cyclohexane was confirmed by ^{1}H NMR as previously reported.[49] AOT concentrations ranged from submillimolar to 0.2 M. Spectra were obtained using a Varian 400 MHz NMR spectrometer or a Varian Inova-500 MHz spectrometer using the Varian supplied pulse sequence at Colorado State University.

4.3 Results

One effective method to measure the presence and properties of soft particles in solution enlists light scattering; we use this method to explore the average size of particles in solution.[19] Our DLS measurements for AOT in cyclohexane, d_{12}-cyclohexane and 1-octanol show the increasing size with increasing w_0 in Figure 4.2, confirming that the size of the reverse micelles increased as the relative amount of water is increased in these microemulsions. The sizes we measure for the reverse micelles in cyclohexane are consistent with reports in the literature.[62,66] Normally reverse micelles form in non-polar solvents,[43] but here we also present evidence of their formation in a somewhat polar solvent, 1-octanol. Figure 4.2 shows that for the same value of w_0, reverse micelles in each different solvent all have similar size and increase in size linearly with increasing w_0. Data in Figure 4.2 also show that particles formed in 1-octanol are slightly smaller than those formed in cyclohexane and that particle size is smaller in deuterated cyclohexane compared to protonated cyclohexane.

Reverse micelles can form over a range of AOT concentrations. Figure 4.3 shows the hydrodynamic radius of two differently sized (two different w_0 values) reverse micelles formed in 1-octanol and in h_{12}-cyclohexane for a range of AOT concentrations, as measured by DLS. The data reveal insignificant variation in the hydrodynamic radius with concentration; the reverse micelle size does not depend on surfactant concentration. However, when the AOT concentration exceeds 0.2 M, secondary larger features appear in the DLS signals. These larger features are attributed to interactions between micelles, described by flocculation and/or percolation.[67] When collecting reverse micelle data, we avoid using concentrations that are above the flocculation and percolation point whenever possible.

In addition to observing the presence of particles in solutions by DLS, interactions between surfactants are evident in ^{1}H NMR spectra. Figure 4.4 shows the ^{1}H NMR spectra of reverse micelles prepared using cyclohexane both in the absence and presence of cholesterol are similar consistent with reverse micelle formation. The spectrum of pure cholesterol is presented at the bottom of the figure for comparison. The spectra show that cholesterol has little or no significant impact on the chemical shifts of the AOT in the spectrum. This suggests that AOT reverse micelles form in the presence of cholesterol without significant interaction. If there were an interaction between cholesterol and a significant fraction of the AOT reverse micelles, we would expect to see shifts in the AOT and the cholesterol peaks.[49] Attempts to characterize these interactions by 2D NOESY ^{1}H NMR spectroscopy were inconclusive due to overlap of AOT and cholesterol peaks, size regime of the reverse micelles and the time scale of the experiment.

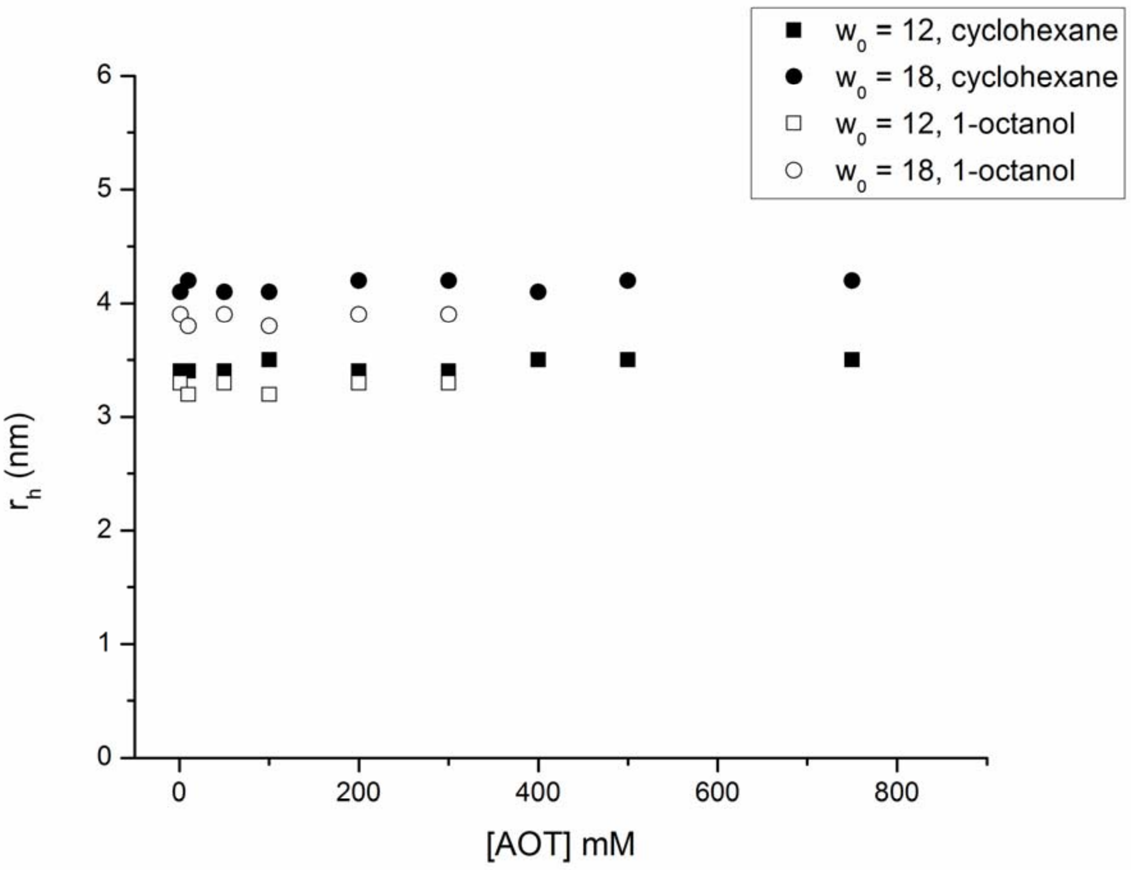

Figure 4.3 AOT reverse micelle (w_0 =12 ●○ , and w_0 =18 ■□) hydrodynamic radius, r_h (AOT) as a function of [AOT]. Filled symbols (■,●) represent data for water/200mM AOT/cyclohexane reverse micelles while hollow points (□,○) are water/200mM AOT/1-octanol reverse micelles. Error bars represent the standard deviation of the particle size.

However, the 1D ^{1}H NMR spectra in Figure 4.4 show that the environment of cholesterol in the AOT/cyclohexane solution is similar to that observed in chloroform. Because cholesterol molecules self-aggregate in chloroform[68], these spectra support the interpretation that self-aggregation takes place in cyclohexane as discussed further below.

Before considering mixed systems of AOT and cholesterol, we explored the solution behavior of cholesterol in cyclohexane and 1-octanol. Figure 4.5 shows the results from DLS experiments measuring the size of particles formed by cholesterol in cyclohexane and 1-octanol, r_{agg} the average radius of the cholesterol particles, as a function of cholesterol concentration. In the cyclohexane sample, as the concentration of cholesterol increases, the particle size increases. This suggests formation of cholesterol aggregates, in agreement with reports in the literature.[69-74] In contrast, the particle size does not change for cholesterol in 1-octanol as a function of concentration, consistent with the interpretation that cholesterol disperses as monomers in 1-octanol.[70].

With cholesterol's solution behavior in both cyclohexane and 1-octanol as reference points, we investigated the mixed AOT reverse micelle/cholesterol system. DLS measurements of solutions containing both AOT and cholesterol in either cyclohexane or 1-octanol generate two distinct diffusion times; indicating two types of particles coexist in the solutions. The bottom panel of Figure 5 shows the hydrodynamic radius for particles detected in DLS experiments probing AOT/cholesterol/ mixed system in 1-octanol. The larger of the two aggregates is indistinguishable from the size observed for AOT reverse micelles described in Figure 4.2. The smaller of the two aggregates is the same as the particles observed when cholesterol is dispersed in 1-octanol, as shown in Figure 4.5. Neither the size of the large nor the small particle in 1-

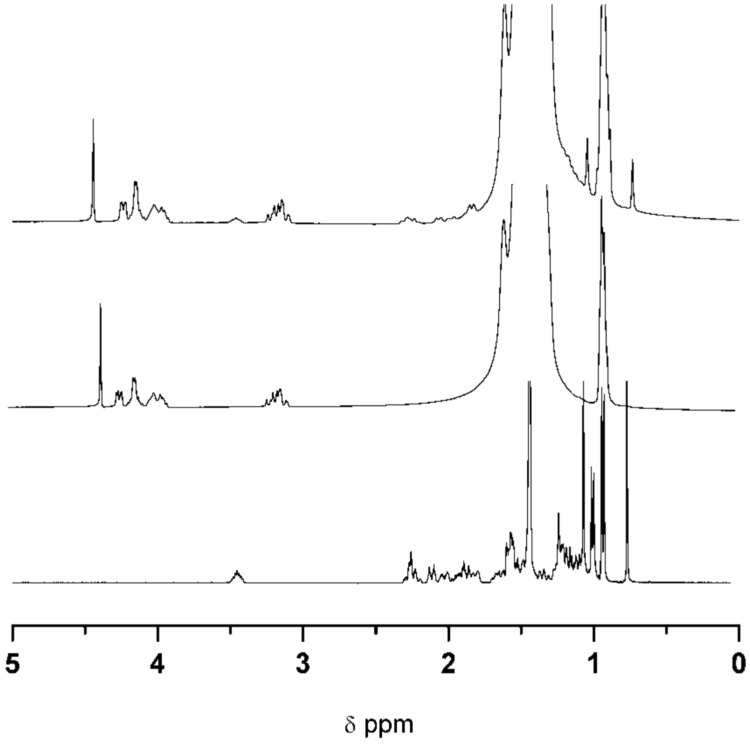

Figure 4.4 a) ^{1}H NMR spectra of cholesterol in chloroform, b) 100mM AOT reverse micelles (w_0 =8) in d_{12}-cyclohexane, and c) 100mM AOT reverse micelles (w_0 =8) in d_{12}-cyclohexane with 25mM cholesterol.

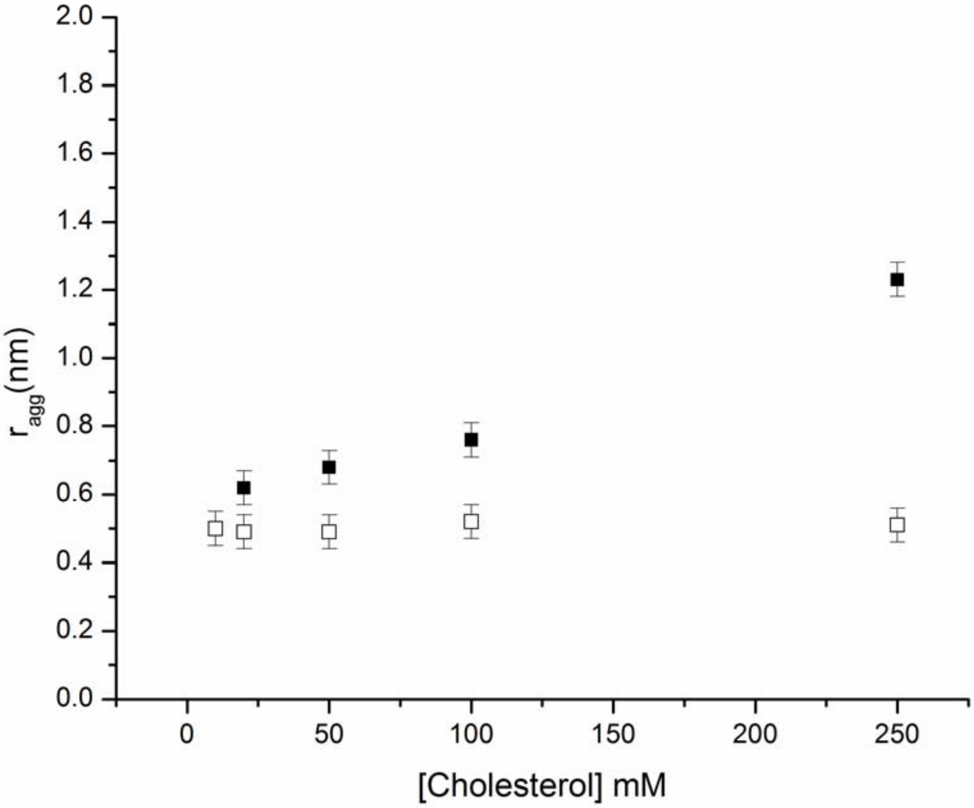

Figure 4.5 Cholesterol particle size, r_{agg}, as a function of [chlolesterol] for cholesterol dissolved in cyclohexane (■) and 1-octanol(□). No AOT is present in these samples. Error bars represent the standard deviation in the particle size.

octanol depends on the cholesterol concentration. As shown in Figure 4.3, changing the AOT concentration has no impact on the reverse micelle size.

Separately, we can make solutions of 0.1 M AOT in cyclohexane and 0.1 M cholesterol in cyclohexane. However, when attempting to make a solution including both 0.1 M AOT and 0.1 M cholesterol in the same cyclohexane solution, phase separation occurs. This fact alone demonstrates that AOT and cholesterol interact with each other. Because we found that certain ratios result in phase separation, the successful ratios targeted in this work generally did not contain less AOT than a 2:1 AOT:cholesterol. Because the solubility of cholesterol in these solutions depends on the AOT concentration, the data points used in this work require varying AOT concentrations to accommodate the increasing cholesterol concentrations. For example, when [cholesterol] = 50 mM, then we use [AOT] = 150 mM but when [cholesterol] = 100 mM, we must increase to [AOT] = 250 mM; specific details about the concentrations used appear in the experimental section and the figure captions.

DLS data for AOT/cholesterol in cyclohexane, shown in the top panel in Figure 4.6, also reveals the presence of two distinct particle sizes coexisting in the solutions. The larger of the two aggregates is same size as the AOT reverse micelles reported in Figure 4.2. However, the smaller of the two aggregates is much smaller than AOT reverse micelles reported in Figure 4.2, but is larger than the cholesterol-only aggregates shown in Figure 4.5. The data obtained for AOT RM samples, w_0 =12 and w_0 =18, are reported here in Figure 4.6. These values for w_0 were chosen out of the range of w_0 from 4-32 for several reasons. First they were chosen due to the ability to resolve the size of the cholesterol aggregate from the AOT reverse micelle. Secondly,

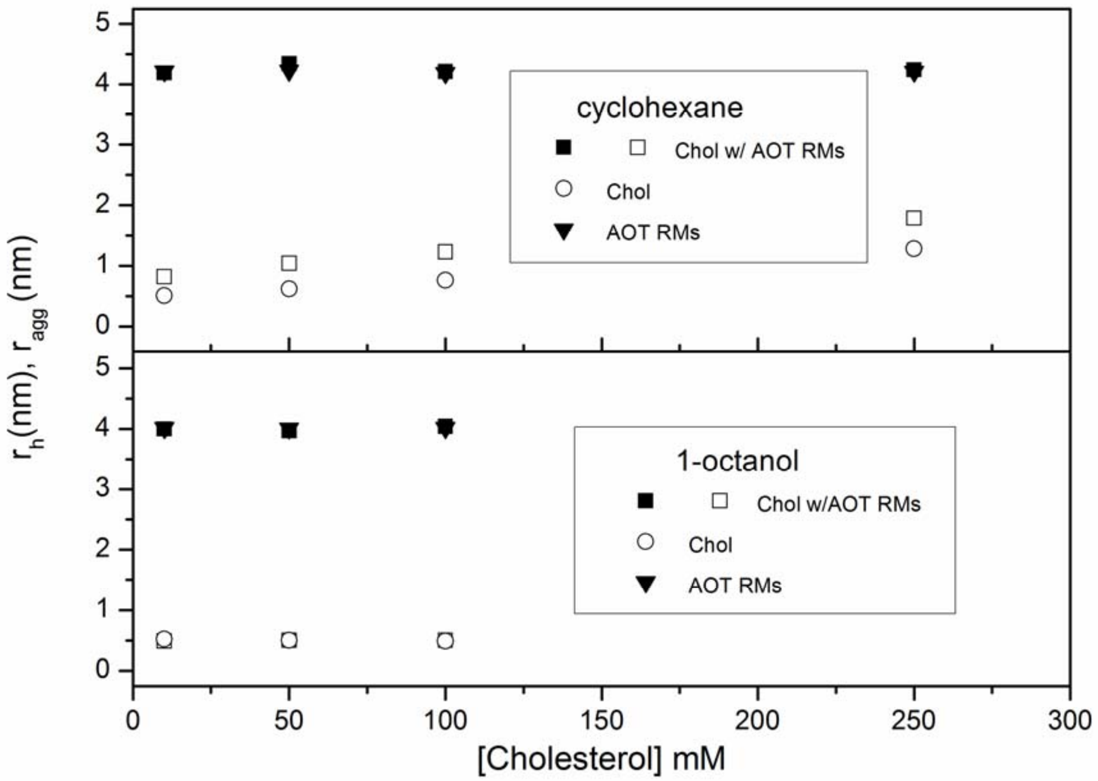

Figure 4.6 Particle size for AOT reverse micelles (r_h) and cholesterol (r_{agg}). Top panel: water/200mM AOT/cyclohexane reverse micelles w_0 =18 (▼), cholesterol particles in cyclohexane with (200mM) AOT reverse micelles w_0 =18 (■), and cholesterol in cyclohexane (●). Bottom panel: water/200mM AOT/1-octanol reverse micelles w_0 =18 (▽), cholesterol particles in 1-octanol with (200mM) AOT reverse micelles w_0 =18 (□), and cholesterol in 1-octanol (○).

w_0 =12 and w_0 =18 are highly characterized and well understood in the literature with few issues of sample preparation and characterization.[19,49,66] For both the cyclohexane and the 1-octanol system, the size of the AOT reverse micelles does not change as a function of cholesterol concentration, indicating that the cholesterol is not associated with these particles. However, the smaller particles that form in cyclohexane depend distinctly on concentration; their size is larger than observed for cholesterol aggregates that in cyclohexane in the absence of AOT. This suggests that the AOT and water present in the microemulsion impact the size of the cholesterol particles. One likely interpretation of these observations is that these particles incorporate both cholesterol and AOT.

When the cholesterol aggregates are similar in size to the AOT reverse micelles the signal from the aggregate and the signal from the reverse micelle appear as one broad peak and cannot be distinguished from each other. Having the cholesterol aggregate and reverse micelles similarly sized would make it difficult to resolve the peaks separately and thus easily missed as for example this was done when we examined this system in AOT/isooctane.

4.4 Discussion

Based on literature reports and the role of cholesterol in lipid bilayers suggests that cholesterol added to a solution containing self-assembled AOT reverse micelles would interact with AOT molecules and add to the interface of the reverse micelles.[22,55,75] Indeed, cholesterol and many other amphiphilic molecules interact with surfactants such as AOT.[8,76] However, cholesterol has a strong propensity to aggregate with itself both in polar and in nonpolar solvents,[68,69,72-74,77] which can substantially impact its behavior in microemulsions. Indeed, there are very few solvents in which cholesterol disperses in its monomeric state without forming aggregates[68,71,74,78-80]. The balance between polar and nonpolar nature found for 1-octanol provides an environment where cholesterol molecules exist without aggregation.[70] Here, we present a detailed study that explores the cholesterol in AOT reverse micelle systems in greater detail using DLS to determine the sizes of the particles forming. The data that we present here supports the interpretation that cholesterol self-aggregation dominates its behavior in microemulsion solutions.

Our DLS measurements of the AOT reverse micelle/cholesterol mixed samples showed evidence for two aggregates coexisting in the solution. When we first analyze the DLS data of the cholesterol/AOT/cyclohexane system, we noticed that some of the reverse micelles formed were smaller than anticipated and that they had a larger polydispersity. Upon investigating the autocorrelation functions, we found substantially better fits to biexponential functions than the standard cumulant fit and regulated fit provided by the DYNAMICS software. Using a biexponential decay to fit the data reveals the presence of two aggregates in solution; one of the aggregates was exactly the size expected for the standard AOT reverse micelle aggregate,[19,21] but the other aggregate was much smaller. At the lowest cholesterol concentrations probed, 20 mM, the size of the smaller aggregate appears the same regardless of w_0 or the presence of AOT, consistent with monomeric or possibly dimeric cholesterol.[68] We crudely estimate the long axis of monomeric cholesterol to be ~1.2 nm, the size data measured by DLS shown in Figure 4.5, yielding a molecular diameter of 1.2 nm is consistent with the interpretation that the cholesterol in 1-octanol is monodisperse. However, trends for the hydrodynamic radius of the smaller peak differ depending on the organic solvent. In 1-octanol, the particle size remains constant as the cholesterol concentration varies whereas in cyclohexane, the particles grow with increasing cholesterol concentration.

Cholesterol's aggregation has been widely characterized in aqueous solutions.[74,78] In contrast, cholesterol disperses without aggregation in 1-octanol.[70] In nonpolar solvents such as cyclohexane and chloroform, Giordani et al. observed that cholesterol forms higher order aggregates.[70] Additionally, when water is present in the nonpolar solvent, they found larger cholesterol aggregates than when using dry solvents. These studies indicate that water incorporates into the cholesterol aggregates and provide precedent for cholesterol self-assembly occurring in multicomponent solutions. We also find that water associates with the cholesterol-AOT aggregate. The DLS results show that the cholesterol containing aggregates present in the mixed systems had hydrodynamic radii about 0.5 nm larger on average than the pure cholesterol aggregates in neat solvent shown in Figure 4.4, consistent with AOT comprising a part of the cholesterol aggregates. Since the w_0 size did not change significantly with changing cholesterol and AOT concentrations, water must accompany the AOT in the cholesterol aggregate. The fact that the amount of water in the cholesterol-AOT aggregate does not change significantly is because the water remains associated with the AOT in reverse micelles.

Cholesterol's solubility and aggregation in neat organic solvents is well known.[70,73,80,81] However, when cholesterol is present in solution with AOT the solubility of cholesterol changes. Cholesterol's solubility depends on the AOT:cholesterol ratio. In solutions with cholesterol at a ratio higher than 2:1 AOT:cholesterol, we observe precipitation, which we attribute to the cholesterol based on the absence of cholesterol peaks in the ^{1}H NMR spectra of the supernatant solution. For example, a solution containing 200 mM AOT in cyclohexane can only accommodate up to 100 mM cholesterol. Because the AOT reverse micelle size does not change as a function of AOT concentration, as shown in Figure 4.3, raising the AOT concentration should not significantly affect the self-assembled AOT reverse micelle structures that form.

Thus, to achieve higher concentrations of cholesterol, we increased the AOT concentration accordingly.

Several previous studies have explored microemulsions containing both AOT and cholesterol.[22,54,55,75] We find that our interpretation of the state of the water/AOT/cholesterol solutions can account for the various results presented in the literature. In ^{13}C NMR nuclear Overhauser effect (NOE) studies, Maitra and co-workers presented evidence that cholesterol hydrogen bonds with AOT head groups.[22] They observed that as cholesterol was added, the negative NOE signal gradually increased to positive values, which they interpreted as the cholesterol interacting with the AOT head group inside the reverse micelle. This interpretation was based on the assumption that when cholesterol is added to solution, it incorporates into the AOT reverse micelles. However, the results by Maitra and co-workers can also be interpreted as cholesterol interacting with AOT in smaller aggregates as observed in our studies.

Destrée and co-workers report facilitation of AOT reverse micelles in heptanes in the formation of cholesterol nanoparticles.[54] They report that adding cholesterol dissolved in chloroform to a solution of water/AOT/heptanes, provides stabilization in the form of cholesterol nanoparticles; they attribute the stabilization to the reverse micelles' ability to solubilize the cholesterol nanoparticle. In fact, it has been shown[70] that cholesterol forms aggregates in chloroform in the absence of AOT, especially if the chloroform contains water. By injecting a solution of cholesterol in chloroform to the AOT/heptanes/water solution, our observations support the suggestion that the cholesterol aggregates acquired some AOT and water from the system.

Chattopadhyay and Kelkar introduced fluorescently-labeled cholesterol into solutions of water/AOT/isooctane.[55] They specifically employ this probe relying on cholesterol to drive the insertion of the probe into the interface. The fluorescent probe is polar and assumed to reside in the water pool.[55] Given the propensity for the fluorescent probe to be solubilized in water and cholesterol's low solubility in isooctane and water, this may drive the location of the labeled-cholesterol. However, the low concentration of Chattopadhyay and Kelkar's study (below 8μM) makes comparison of these studies with our results less straightforward.

Previously, we have studied the interactions of some vanadium containing anti-diabetic drugs with AOT reverse micelles with and without cholesterol.[60] Following ^{1}H NMR chemical shifts of cholesterol[60,61] and the drug, the chemical shifts we observed in the drugs and the surfactant signals suggested that the drug penetrated the interface. Recent studies demonstrated that most of the changes were observed both in self assembled structures that contain cholesterol and those without cholesterol. These results are consistent with our observations reported here where a new AOT/cholesterol particle forms. The observed changes can be due to penetration of the drug in the interface of the AOT reverse micelles of the cholesterol containing particle.

Nagarajan and co-workers inferred that cholesterol assembles into the AOT reverse micelles because their experiments showing that cholesterol oxidase in solutions of AOT and cholesterol in isooctane. The reverse micelles not only continues to demonstrate the same enzymatic activity but actually enhances enzymatic activity.[75] They observed an increase in cholesterol oxidase enzymatic activity for solutions with small water content ($\leq w_0$=8) but not for large ($\leq w_0$=30) reverse micelles. However, given that AOT reverse micelles have dimensions smaller than the enzyme raises questions about the nature of the system and whether the enzyme is in solution.[82] This is particularly pertinent, because in the large reverse micelles, when there is room for the enzyme, no enhancement in enzyme activity was observed. Whatever the nature of the AOT-enzyme particles that forms in these systems, the increased enzyme activity reflects some type of interaction favoring the process. Increased enzymatic activity could arise from the enzyme acting on the AOT-cholesterol aggregate that we observe in this work. The possibility exists that the AOT-cholesterol aggregate is a better substrate than aggregates composed only of cholesterol. This hypothesis could be tested by concentration dependent dissolution of the enzyme and cholesterol in the organic solvent.

4.5 Conclusions.

Through a series of careful measurements of cyclohexane solutions containing AOT reverse micelles and cholesterol, we have tested the hypothesis whether cholesterol incorporates into AOT reserve micelles. These experiments confirm the possibility that a complex media can support formation of two compositional distinct self-assembled particles in solution. Based on our results, we conclude that cholesterol does not incorporate into the AOT reverse micelles in cyclohexane. Rather, cholesterol-AOT aggregates coexist in solution with the AOT reverse micelles. Our studies further suggest that cholesterol self-aggregates including some AOT and water in the adducts formed. The normal AOT reverse micelles form after the cholesterol has been used up. Studies with a dispersing solvent, 1-octanol, was also used for comparison to contrast these observations. We conclude that compositionally distinct self-assembled particles can form and coexist in the same complex solution. Importantly, such cases are only likely to be observed when the additional components readily self-assemble forming very stable structures.

The studies presented here show that cholesterol does not simply incorporate into AOT reverse micelles in cyclohexane as suggested in literature reports. Such systems may form aggregates consisting of cholesterol, AOT, and other surfactants and water. These findings are particularly important for administration of cholesterol for specific health purposes. Not only is cholesterol a metabolite, it is also used as a targeting agent for breast cancer drugs. Specific targeting of the lymph tissue is most likely related to the particular form of cholesterol administered. Because several drug formulations are based on the concept that cholesterol helps target the drug, fundamental information on possible nanostructures, should assist future applications of cholesterol. The fundamental studies described in this work are critically important for future understanding and applications of cholesterol in the life sciences.

4.6 References

(1) Lu, H.-Z.; Li, B.-Q. *Immunopharm.* **2009**, *31*, 485-491.

(2) Hao, M.; Mukkherjee, S.; Maxfield, F. R. *PNAS* **2001**, *98*, 13072-13077.

(3) Simons, K.; Toormre, D. *Nature Reviews Molecular Cell Biology* **2000**, *1*, 31-41

(4) Kucherak, O. A.; Oncul, S.; Darwich, Z.; Yushchenko, D.; Arntz, Y.; Didier, P.; Mely, Y.; Klymchenko, A. *J. Am. Chem. Soc.* **2010**, *132*, 4097-4916.

(5) Zhang, Y.; Li, X.; Becker, K. A.; Gulbins, E. *Biochim. Biophys. Acta* **2009**, *1788*, 178-183.

(6) Ivankin, A.; Kuzmenko, I.; Gidalevitz, D. *Phys. Rev. Lett.* **2010**, *104*.

(7) Presti, F. T.; Pace, R. J.; Chan, S. I. *Biochemistry* **1982**, *21*, 3831-3835.

(8) Ohvo-Rekila; B., R.; P., L.; JP, S. *Prog Lipid Res.* **2002**, *41*, 66-97.

(9) Schubert, D.; Boss, K. *Federation of European Biochemical Societies* **1982**, *150*, 1-8.

(10) Ramstedt, B.; Slotte, J. P. *Biophysical Journal* **1999**, *76*, 908-915.

(11) Mannock, D. A.; Lewis, R. N. A. H.; McMullen, T. P. W.; McElhaney, R. N. *Chem. Phys. Lipids* **2010**, *163*, 403-448.

(12) Boulikas, T. *Expert Opin. Investig. Drugs* **2009**, *18*, 1197-1218.

(13) Selvakumaran, M.; Pisarcik, D. A.; Bao, R.; Yeung, A. T.; Hamilton, T. C. *Cancer Res.* **2003**, *63*, 1311-1316.

(14) Boulikas, T. *Cancer Therapy* **2007**, *5*, 351-376.

(15) Dalmarco, E. M.; Frode, T. S.; Medeiros, Y. S. *Transpl Immunol* **2004**, *12*, 151-157.

(16) Dong, X.; Shi, W.; Yuan, G.; Xie, L.; Wang, S.; Lin, P. *Graefe's Arch Clin Exp Ophthalmol* **2006**, *244*, 492-497.

(17) Dunn, C. J.; Wagstaff, A. J.; Perry, C. M.; Plosker, G. L.; Goa, K. L. *Drugs* **2001**, *61*, 1957-2016.

(18) Kumar, C.; Balasubramanian, D. *J. Colloid Interface Sci.* **1979**, *69*, 271-279.

(19) Zulauf, M.; Eicke, H. F. *J. Phys Chem* **1979**, *83*, 480-486.

(20) Lang, J.; Jada, A.; Malliaris, A. *J. Phys Chem* **1988**, *92*, 1946-1953.

(21) De, T. K.; Maitra, A. *Adv. Colloid Interface Sci.* **1995**, *59*, 95-193.

(22) Maitra, A.; Dinesh; Patanjali, P. K.; Varshney, M. *Colloids Surf.* **1986**, *20*, 211-219.

(23) Magid, L. J.; Konno, K.; Martin, C. A. *J. Phys Chem* **1981**, *85*, 1434-1439.

(24) Levinger, N. E. *Science* **2002**, *298*, 1722-1723.

(25) Baruah, B.; Roden, J. M.; Sedgwick, M.; Correa, N. M.; Crans, D. C.; Levinger, N. E. *J. Am. Chem. Soc.* **2006**, *128*, 12758-12765.

(26) Crans, D. C.; Trujillo, A. M.; Bonetti, S.; Rithner, C. D.; Baruah, B.; Levinger, N. E. *J. Org. Chem.* **2008**, *73*, 9633-9640.

(27) Giustini, M.; Palazzo, G.; Colafemmina, G.; DellaMonica, M.; Giomini, M.; Ceglie, A. *J. Phys. Chem.* **1996**, *100*, 3190-3198.

(28) Umegak, T.; Yan, J.-M.; Zhang, X.-B.; Shioyama, H.; Kuriyama, N.; Xi, Q. *Journal of Power Sources* **2009**, *191*, 209-216.

(29) Correa, N. M.; Biasutti, M. A.; Silber, J. J. *J. Colloid Interface Sci.* **1995**, *172*, 71-76.

(30) Correa, N. M.; Silber, J. J. *J. Mol. Liq.* **1997**, *72*, 163-176.

(31) Sapp, S. A.; Elliot, C. M. *Chem. Mater.* **2003**, *15*, 1237-1241.

(32) Valentine, K. G.; Peterson, R. W.; Saad, J. S.; Summers, M. F.; Xu, X.; Ames, J. B.; Wand, A. J. *Structure* **2010**, *18*, 9-16.

(33) Levinger, N. E.; Swafford, L. A. *Annu. Rev. Phys. Chem.* **2009**, *60*, 385-406.

(34) Hazra, P.; Chakrabarty, D.; Sarkar, N. *Chem. Phys. Lett.* **2002**, *358*, 523-530.

(35) Lawrence, M. J.; Rees, G. D. *Adv. Drug Delivery Rev.* **2000**, *45*, 89-121.

(36) Gupta, S.; Moulik, S. P. *J. Pharm. Sci.* **2008**, *97*, 22-45.

(37) Kreilgaard, M. *Adv. Drug Delivery Rev.* **2002**, *54*, S77-S98.

(38) Beers, M. v.; Sauberborn, M.; Gilli, F.; Brinks, V.; Schellekens, H.; Jiskoot, W. *Pharm. Res.* **2010**, *27*, 1812-1824.

(39) Qin, Y.; Fan, W.; Chen, H.; Yao, N.; Tang, W.; Tang, J.; Kuai, R.; Zhang, Z.; Wu, Y.; He, Q. *J. Drug Targeting* **2010**, *18*, 536-549.

(40) Lee, S.-M.; Chen, H.; O'Halloran, T. V.; Nguyen, S. T. *J. Am. Chem. Soc.* **2009**, *131*, 9331-9320.

(41) Gaidamauskas, E.; Cleaver, D. P.; Chatterjee, P. B.; Crans, D. C. *Langmuir* **2010**, *26*, 13153-13161.

(42) Koper, G. J.; Sager, W. F. C.; Smeets, J.; Bedaux, D. *J. Phys Chem* **1995**, *99*, 13291-13300.

(43) Liu, Z.-T.; Erkey, C. *Langmuir* **2001**, *17*, 274-277.

(44) Luan, Y.; Xu, G.; Yuan, S.; Xiao, L.; Zhang, Z. *Langmuir* **2002**, *18*, 8700-8705.

(45) Formariz, T. P.; Sarmento, V. H. V.; Silva-Junior, A. A.; Scarpa, M. V.; Santilli, C. V.; Oliveira, A. G. *Colliods and Surfaces B: Biointerfaces* **2006**, *51*, 54-61.

(46) Stubenrauch, C.; Tessendorf, R.; Strey, R.; Lynch, I.; Dawson, K. A. *Langmuir* **2007**, *23*, 7730-7737.

(47) Formariz, T. P.; Sarmento, V. H. V.; Silva-Junior, A. A.; Scarpa, M. V.; Santilli, C. V.; Oliveira, A. G. *Colloids Surf., B* **2006**, *51*, 54-61.

(48) Piletic, I. R.; Moilanen, D. E.; Spry, D. B.; Levinger, N. E.; Fayer, M. D. *J. Phys Chem A.* **2006**, *110*, 10369.

(49) Stahla, M. L.; Baruah, B.; James, D. M.; Johnson, M. D.; Levinger, N. E.; Crans, D. C. *Langmuir* **2008**, *24*, 6027-6035.

(50) Faeder, J.; Ladanyi, B. M. *J. Phys Chem B.* **2000**, *104*, 1033-1046.

(51) Zhang, W.; Qiao, X.; Chen, J. *Colloids Surf., A* **2006**, *299*, 22-28.

(52) Pieniazek, P. A.; Lin, Y.-S.; Chowdhary, J.; Ladanyi, B. M.; Skinner, J. L. *J. Phys Chem B* **2009**, *113*, 15017-15028.

(53) Klymchenko, A. S.; Demchenko, A. P. *Langmuir* **2002**, *18*, 5637-5639.

(54) Destree, C.; Ghijsen, J.; Nagy, J. B. *Langmuir* **2007**, *23*, 1965-1973.

(55) Kelkar, D. A.; Chattopadhyay, A. *J. Phys. Chem. B* **2004**, *108*, 12151-12158.

(56) Li, M.; Mann, S. *Langmuir* **2000**, *16*.

(57) Spehr, T.; Frick, B.; Grillo, I.; Falus, P.; Muller, M.; Stuhn, B. *Phys. Rev.* **2009**, *79*.

(58) Hasegawa, M.; Yamaaski, Y.; Sonta, N.; Shindo, Y.; Sugimura, T.; Kitahara, A. *J. Phys Chem* **1996**, *100*, 15575-15580.

(59) Rack, J. J.; McCleskey, M.; Birnbaum, E. R. *J. Phys Chem B* **2002**, *106*, 632-636.

(60) Roess, D. A.; Smith, S. M. L.; Holder, A. A.; Baruah, B.; Trujillo, A. M.; Gilsdorf, D.; Stahla, M. L.; Crans, D. C. In *Vanadium: The Versitile Metal*

ACS Symposium Series: 2007; Vol. 974, p 121-134.

(61) Roess, D.; Smith, S. M. L.; Winter, P.; Zhou, J.; Dou, P.; Baruah, B.; Trujillo, A. M.; Levinger, N. E.; Yang, X.; Barisas, B. G.; Crans, D. C. *Chem. Biodiversity* **2008**, *5*, 1558-1570.

(62) Levanshov, A. V.; Khmelnitsky, Y. L.; Klyachko, N. L.; Chernyak, V. Y.; Martinek, K. *J. Colloid Interface Sci.* **1982**, *88*, 444-457.

(63) Blitz, J. P.; Fulton, J. L.; Smith, R. D. *J. Phys Chem* **1988**, *92*, 2707-2710.

(64) Bohidar, H. B.; Behboudina, M. *Colliods and Surfaces A: Physiochem. and Eng. Aspects* **2001**, *178*, 313-323.

(65) *Surfactant micelle characterization using dynamic light scattering*, Malvern Instruments ltd., 2006.

(66) Maitra, A. *J. Phys Chem* **1984**, *88*, 5122-5125.

(67) Goto, A.; Kuwahara, Y.; Suzuki, A.; Yoshioka, H.; Goto, R.; Iwamoto, T.; Imae, T. *J. Mol. Liq.* **1997**, *72*, 137-144.

(68) Domanska, U.; Klofutar, C.; Paljk, S. *Fluid Phase Equilib.* **1994**, *97*, 191-200.

(69) Cromie, S. R. T.; Ballone, P. *J. Chem. Phys.* **2009**, *131*.

(70) Giordani, C.; Wakai, C.; Okamura, E.; Matubayasi, N.; Nakahara, M. *J. Phys. Chem. B* **2006**, *110*, 15205-15211.

(71) Cromie, S. R. T.; Popolo, M. G.; Ballone, P. *J. Phys. Chem. B* **2009**, *113*, 4674-4687.

(72) Abendan, R. S.; Swift, J. A. *Langmuir* **2002**, *18*, 4847-4853.

(73) Goralski, P. *Fluid Phase Equilib.* **2000**, *167*, 207-221.

(74) Haberland, M. E.; Reynolds, J. A. *Proc. Natl. Acad. Sci. USA* **1973**, *70*, 2313-2316.

(75) Gupte, A.; Nagarajan, R.; Kilara, A. *Ind. Eng. Chem. Res.* **1995**, *34*, 2910-2922.

(76) Hao, M.; Mukkherjee, S.; Maxfield, F. R. *Proc. Natl. Acad. Sci. USA* **2001**, *98*, 13072-13077.

(77) Cromie, S. R.; Popolo, M. G. D.; Ballone, P. *J. Phys Chem B* **2009**, *113*, 4674-4687.

(78) Saad, H. Y.; Higuchi, W. I. *J. Pharm Sci* **1965**, *54*, 1205-1206.

(79) Randolph, T. W.; Clark, D. S.; Blanch, H. W.; Prausnitz, J. M. *Proc. Natl. Acad. Sci. USA* **1987**, *85*, 2979-2983.

(80) Jadzyn, J.; Hellemans, L. *Ber. Bunsen-Ges Phys Chem Chem* **1993**, *97*, 205-210.

(81) Goralski, P.; Tkaczyk, M.; Piekarski, H. *J. Solut. Chem* **1996**, *25*, 1227-1240.

(82) Yue, Q. K.; Kass, I. J.; Sampson, N. S.; Vrielink, A. *Biochem* **1999**, *38*, 4277-4286.

CHAPTER 5

CORRELATING PROTON TRANSFER DYNAMICS TO PROBE LOCATION IN CONFINED ENVIRONMENTS

Preface

Part of the work, the work with AOT and CTAB reverse micelles, presented in this chapter will appear as the journal article, " Correlating Proton Transfer Dynamics to Probe Location in Confined Environments " by Myles Sedgwick, Richard L. Cole, Christopher D. Rithner Debbie C. Crans and Nancy E. Levinger, *J. Am. Chem. Soc.*, Just Accepted Manuscript, Published July 5th 2012 (web). The laser work in this chapter was performed by Dr. Richard L. Cole and can be found, in part in Chapter 5 of his PhD Dissertation[1]. The NMR data were collected and interpreted by Myles Sedgwick with assistance from Dr. Christopher D. Rithner.

5.1 Introduction

Proton transfer reactions are ubiquitous in chemistry, biology and physics.[2] Proton motion is essential to fuel cell operation[3] and enzymatic function.[4] Proton channels shuttle protons across membranes.[5] Detailed studies of proton transfer in a diverse range of model systems have dramatically increased understanding about fundamental proton transfer dynamics.[6-9] Studies enlisting the photoacid, 8-hydroxypyrene-1,3,6-trisulfonate (HPTS), Figure 5.1, have

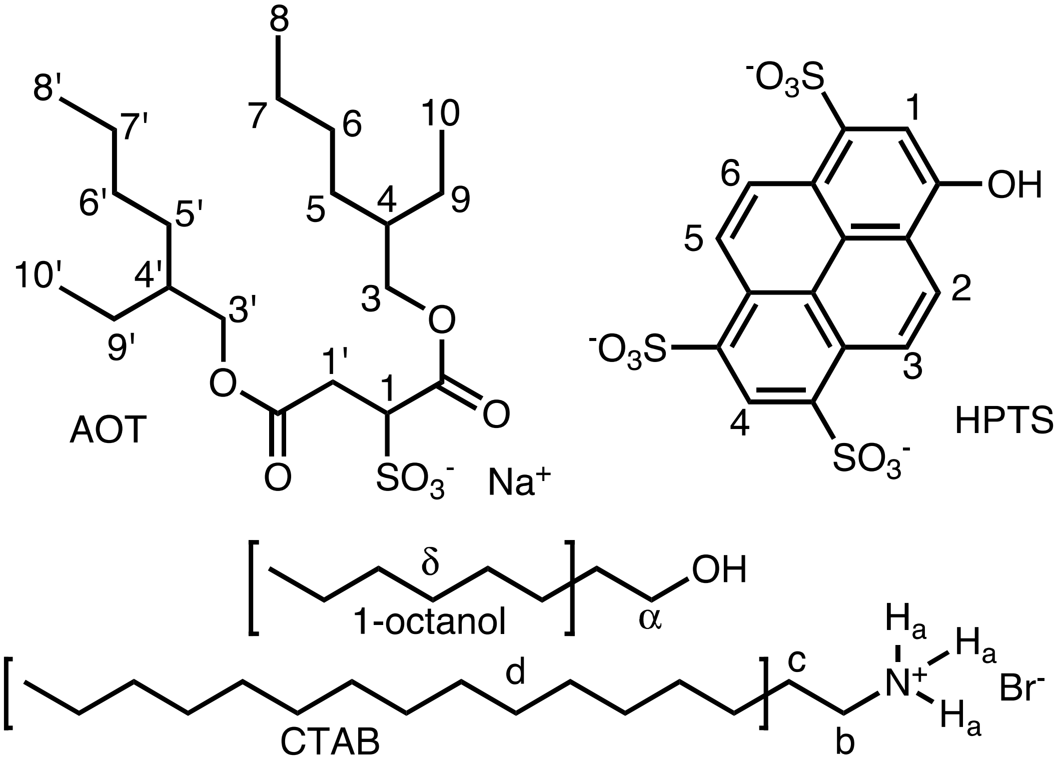

Figure 5.1 Chemical structures for surfactants AOT and CTAB, co-surfactant 1-octanol, and photoacid, HPTS with numbering/lettering for NMR identification used throughout the chapter.

elucidated mechanisms for proton transfer and the role of environment on proton transfer dynamics. [2,6-8,10-16]

As a photoacid, HPTS has a much lower pK_a in its first electronic excited state (0.5-1.4) than in its ground state (7.2-7.7).[10,11] In aqueous environments with $pH > pK_a^*$, photoexcitation leads to excited state HPTS deprotonation.[12] The significant changes in its electronic absorption and emission spectra (Figure 5.2) and its high solubility in aqueous environments contribute to the molecule's utility to study proton transfer reactions. Most HPTS proton transfer studies utilize water as a proton acceptor. Absorption and fluorescence spectroscopy of HPTS in nonaqueous environments lacking proton acceptors show no proton transfer.[12,17]

HPTS proton transfer dynamics have been measured in many different systems. Cox et al. measured how ionic strength affected proton transfer of HPTS in aqueous solution.[16] Exploring peptide-based hydrogels Amdursky et al. found that the walls of self-assembled peptide nanotubes affected the proton geminate recombination process.[15] Spry et al. studied HPTS finding proton transfer dynamics in Nafion membranes at high hydration mirrored 0.5 M HCl solution;[6] at lower hydration levels, the HPTS resides at the Nafion surface where the low local pH precluded proton dissociation. Oxidized porous silicon appears to enhance HPTS proton transfer dynamics.[18] Researchers have also probed proton transfer dynamics at micelle surfaces.[13,19,20] Roy et al.[13] noted HPTS fluorescence quenching at alkyltrimethylammonium bromide micelle surfaces by acetate counterions. Clearly, complex environments dramatically affect HPTS dynamics.

Researchers have studied nanosized systems to learn about proton transfer in complex, confined and interfacial environments.[2] Isolated water droplets sequestered from a bulk nonpolar

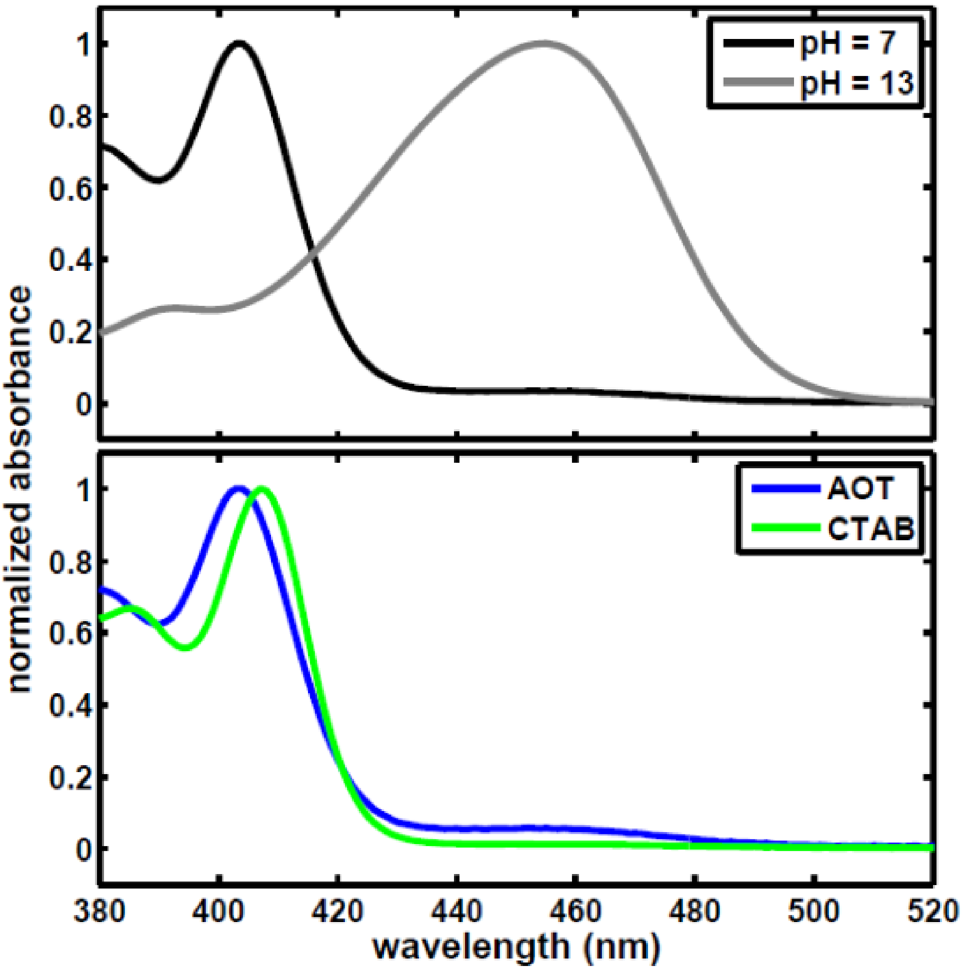

Figure 5.2 Top panel: UV-vis absorption spectrum of HPTS in water under neutral (pH = 7) and basic (pH = 13) conditions displaying protonated and deprotonated forms of HPTS; Bottom panel: in water/AOT/cyclohexane and water/CTAB/*n*-octanol/cyclohexane reverse micelles with w_0=10. Spectra collected with a Varian Cary 500 UV/Vis/NIR spectrophotometer.

phase by a surfactant layer in reverse micelles (RMs) present a versatile model system to explore interfacial and confined environments effects on proton transfer.[21] RMs can be prepared from anionic,[22] cationic[23], nonionic[24] and zwitterionic[25] surfactants; their sizes are well known and proportional to w_0=[H_2O]/[surfactant].[22] Using time-resolved emission spectroscopy, Tielrooij et al. showed decreasing HPTS proton transfer rates in anionic AOT and nonionic Brij-30 RMs[7] with decreasing RM size, regardless of the surfactant used. They also reported some HPTS molecules exhibited nonradiative decay, suggesting that the environment prevented proton transfer. Spry et al. also explored HPTS dynamics in AOT RMs finding that proton diffusion decreases dramatically with decreasing w_0, which they attributed to a change in the water hydrogen bonding network with decreasing micelle size.[26] In this chapter HPTS is investigated in RMs formed using three common surfactants, the anionic AOT (sodium docusate) in cyclohexane, the cationic cetyl trimethylammonium bromide (CTAB) with 1-octanol cosurfactant (5:1 ROH:CTAB) in cyclohexane, and the nonionic surfactant Igepal CO-520 in cyclohexane.

Knowledge of a probe's local environment provides critical understanding of proton transfer dynamics. Probe molecule motion depends on local environment thus measurements of molecular rotation through time-resolved anisotropy have become a standard tool in the ultrafast spectroscopy community. Comparison of parallel and perpendicular time-dependent signals for spectroscopic transitions where the transition dipole remains fixed yields the anisotropy decay,[27]

$$r(t) = \frac{I_{\parallel}-I_{\perp}}{I_{\parallel}+2I_{\perp}} = 0.4C_2(t) \tag{5.1}$$

where $I_{\parallel}(t)$ and $I_{\perp}(t)$ are the time dependent intensities for the probe polarization parallel and perpendicular to the pump beam and $C_2(t)$ is the second Legendre polynomial. Time-resolved anisotropy has shown that some RM environments[6,7] reduce HPTS rotational freedom compared to bulk aqueous solution.[14] Although time-resolved anisotropy shows reduced rotational motion it does not indicate the cause, precluding direct correlation of the reduced molecular motion with changes in the observed proton transfer dynamics. For example, changes in the local viscosity at an interface or embedding the probe molecule in the interface both lead to reduced rotational motion, but it is unclear how these changes would affect the proton transfer reaction.

Using two complementary techniques, we explored the proton transfer dynamics and the location of HPTS in RM environments. Broadband ultrafast time-resolved transient absorption spectroscopy demonstrates significant dependence of the proton transfer dynamics on the charge interactions of HPTS with the surfactant with a cationic headgroup in the RM while the anionic RM shows no probe-surfactant interactions. Together with time-resolved anisotropy measurements, these studies develop a comprehensive picture of the environmental effect on the HPTS proton transfer dynamics.

5.2 Materials and Methods

5.2.a Materials

8-hydroxypyrene-1,3,6- trisulfonate (HPTS, 97%), bis (2-ethylhexyl) sulfosuccinate sodium salt (AOT, 99%), cetyl trimethylammonium bromide (CTAB), polyoxyethylene (5) nonylphenylether (Igepal CO-520), 1-octanol (99%), cyclohexane (99%), d_{12} cyclohexane (99%) and deuterium oxide (D_2O, 99.98%) were purchased from Sigma Aldrich. HTPS, AOT, Igepal CO-520, 1-octanol, cyclohexane and d_{12}-cyclohexane were used without further purification. CTAB was purified by dissolving in absolute ethanol and recrystallizing three times, dried under vacuum filtration, and dried under vacuum. Deionized water was used throughout and was prepared to a specific resistivity > 18MΩ cm (Barnstead E-pure system). pH/pD was controlled by adding HCl/DCl or NaOH to the system.

5.2.b Reverse Micelle Sample Preparation

Reverse micelle samples were made from stock solutions of 0.4 M AOT, 0.4 Igepal CO-520 and 0.1 M CTAB in cyclohexane. For the CTAB samples, 1-octanol was added as a co-surfactant in a ratio of 1:5 (CTAB: 1-octanol). The HPTS stock solution was added to the surfactant solutions to yield $w_0 = 10$ for reverse micelles. A 20 mM stock solution of HTPS was made in slightly acidic conditions (pH ≈ 6.5) to ensure that the ground state form of the dye was protonated. This was confirmed using UV-Vis spectroscopy. Figure 5.2 displays steady-state absorption spectra of HPTS in acidic and basic conditions and protonated HPTS in the reverse micelle environments.

5.2.c Transient Absorption Spectrometer

A description of the laser system and broadband ultrafast transient absorption spectrometer has appeared.[28,29] Briefly, 125 μJ/pulse of the output of a chirped pulse regenerative amplifier (50 fs FWHM pulses at 800 nm, 1 kHz repetition rate) is used for the transient absorption experiment. Frequency doubling in BBO (β-barium borate) generates the second harmonic pump pulses (~20 μJ). Before reaching the sample, the pump beam is optically chopped to provide a reference signal, double passes a fused silica Brewster prism pair to precompensate for material dispersion, and travels down a variable delay path that provides relative delay between the pump and probe pulses. The residual fundamental beam double passes through a fused silica Brewster prism pair before generating a single filament white light continuum used for the probe pulses. Pump and probe beams are focused onto the sample flowing through a 0.5 mm cuvette. The diverging probe beam is collimated, spatially filtered, and traverses a short pass dichroic filter to extinguish the spectral intensity around 800 nm. Transient absorption signals are collected using an Ocean Optics spectrometer (USB 2000+), which is synchronically triggered externally at twice the frequency of the pump beam modulation 100/200 Hz respectively.

Data were collected as a function of the delay between the pump and probe pulses using a custom MatLab (Release 2011b) program that sequentially measured the white light continuum transmitted through the sample with the pump on (signal), $I_{sig}(v,t)$ and pump blocked (reference) $I_{ref}(v,t)$.

$$S(v,t) = -\log\left(\frac{I_{sig}(v,t)}{I_{ref}(v,t)}\right) \tag{5.2}$$

To generate transient absorption spectrograms, signals generated using equation 5.2were compiled as a function of both time and frequency, $S=S(v,t)$. Raw transient spectra were truncated to 1100 wavelength values over a 380-720 nm range and collected from −100 fs to 2 ns with 200 logarithmically spaced time delays values.[28] Spectrograms were generated from both parallel and perpendicular pump beam polarizations with respect to the probe beam polarization. Because the white light continuum has a non-zero temporal chirp, we limited analysis of our data to times longer than 300 fs to avoid spectral shifting arising from the chirp.

To extract information about reorientation dynamics from the two dimensional data we used one of two methods. For data with high signal to noise, intensities at single wavelength (~530 nm) as a function of time for both parallel and perpendicular spectrograms yielded effective signals, $S=S(t)$, from equation 5.2. For samples yielding lower signal to noise, we averaged data from several wavelength values near the strongest broadband femtosecond transient absorption signal to yield parallel and perpendicular signals from which reorientational dynamics were determined.

To measure decay times in the absence of rotational contributions, signals were calculated from parallel and perpendicular polarization spectrograms via,

$$P(v,t) = \frac{1}{3}(S_{\parallel}(v,t,) + 2S_{\perp}(v,t)) \tag{5.3}$$

Rotational anisotropy decays were calculated via,

$$r(t) = \frac{S_{\parallel}(t) - S_{\perp}(t)}{S_{\parallel}(t) + 2S_{\perp}(t)} \tag{5.4}$$

where $S_{||}(t)$ and $S_{\perp}(t)$ are the time-dependent integrated transient absorption spectral intensities for parallel and perpendicular polarization between the pump and probe beams, respectively. The anisotropy data for HPTS in CTAB reverse micelles does not decay to zero, prompting us to fit the data to the wobble-in-a-cone model.[30,31] This analysis allows us to gauge the degree of librational motion possible for the HPTS in these confined systems. We fit the anisotropy decay data to the function,

$$r(t) = A\left(Q^2 - (1 - Q^2)\exp\left(-\frac{t}{\tau_R}\right)\right)\exp\left(-\frac{t}{\tau_M}\right) \tag{5.5}$$

where Q and τ_R quantify the degree of restriction and time scale for motion within the cone, and τ_M accounts for slower decay components. Results from this fit appear in Table 5.1. From this fit, we use Q to obtain the cone semi-angle, θ, from,

$$Q^2 = (\frac{1}{2}\cos\theta\,(1 + \cos\theta))^2 \tag{5.6}$$

Table 5.1 Fit Parameters Acquired from Wobble-in-a-Cone Analysis[30,31] of HPTS Anisotropy in CTAB Reverse Micelles.

Parameter	Q	τ_M (ps)	τ_R (ps)	A
Fit value	0.89±0.02	2500±250	190±50	0.28±0.001

For HPTS in CTAB reverse micelles, we find $\theta = 22.4^\circ$. This indicates significant confinement of the HPTS molecule in the reverse micelle samples, and is consistent with the interpretation that the molecule embeds in the interfacial region.

5.2.d NMR spectroscopy

Proton NMR data were obtained using Varian Inova 400 and 500 MHz NMR spectrometers equipped with 5 mm proton indirect detection probes. Routine parameters were used when collecting the ^{1}H 1D spectra. An external reference of tetramethylsilane (TMS) was used to reference the ^{1}H chemical shifts. Signals were averaged at 1028 scans. The NMR FIDs collected were Fourier transformed and subjected to phase correction (MestReC V. 4.5.9.1 NMR data processing software for Windows). Resulting spectral peaks were fitted to find the chemical shifts and line widths (OriginPro 8.1) of each spectral peak. 1D ^{1}H NMR Spectra for AOT reverse micelles are consistent with previous work.[32] 1D ^{1}NMR spectra for HPTS in water. HPTS in CTAB reverse micelles, and HPTS in AOT reverse micelles are shown in Figures 5.2 5.3 and 5.4, respectively.

For the 2D-NOESY data that was obtained at 500 MHz, the 90 degree pulse width was 5.9 μs, the spectral window was 8kHz in both t_1 and t_2, the acquisition time was 0.15s, digital signal processing and frequency shifted quadrature detection were used. The mixing time was 250 ms. 256 complex increments were obtained in States-TPPI mode and 16 signal averaging transients were collected per increment with a total of 1.9 second recycle time per transient. Gaussian apodization was applied and then the data was zero-filled to 2K by 512 complex points prior to Fourier transform. Forward linear prediction in t_1 was not used. Spectral data processing was done in part by using NMRPipe.[33]

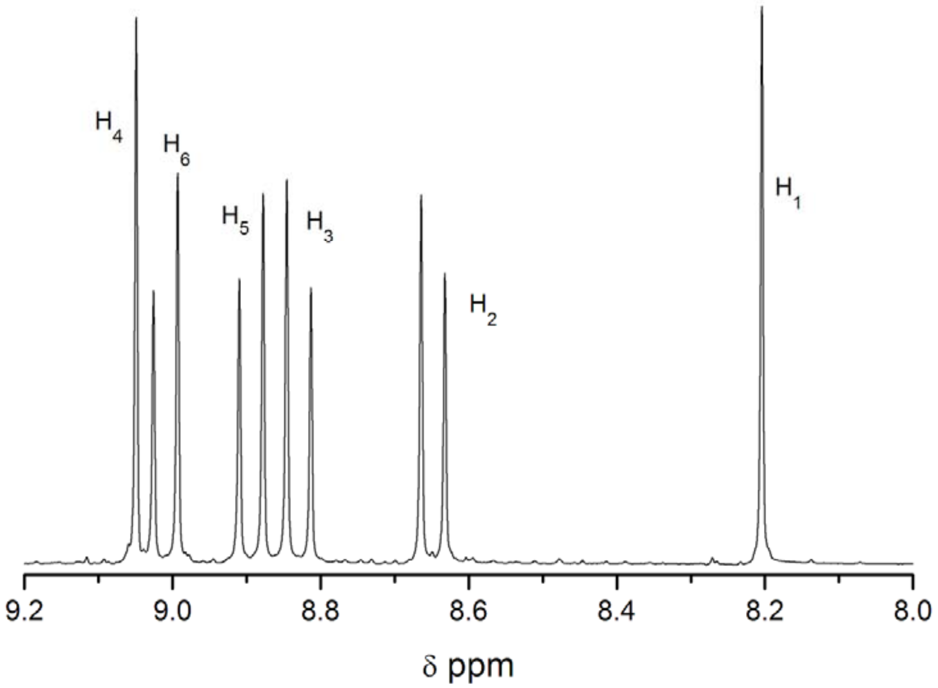

Figure 5.3 ^{1}H NMR spectrum of HPTS in pH 4 water. Labels follow the numbering for HPTS in Figure 5.11

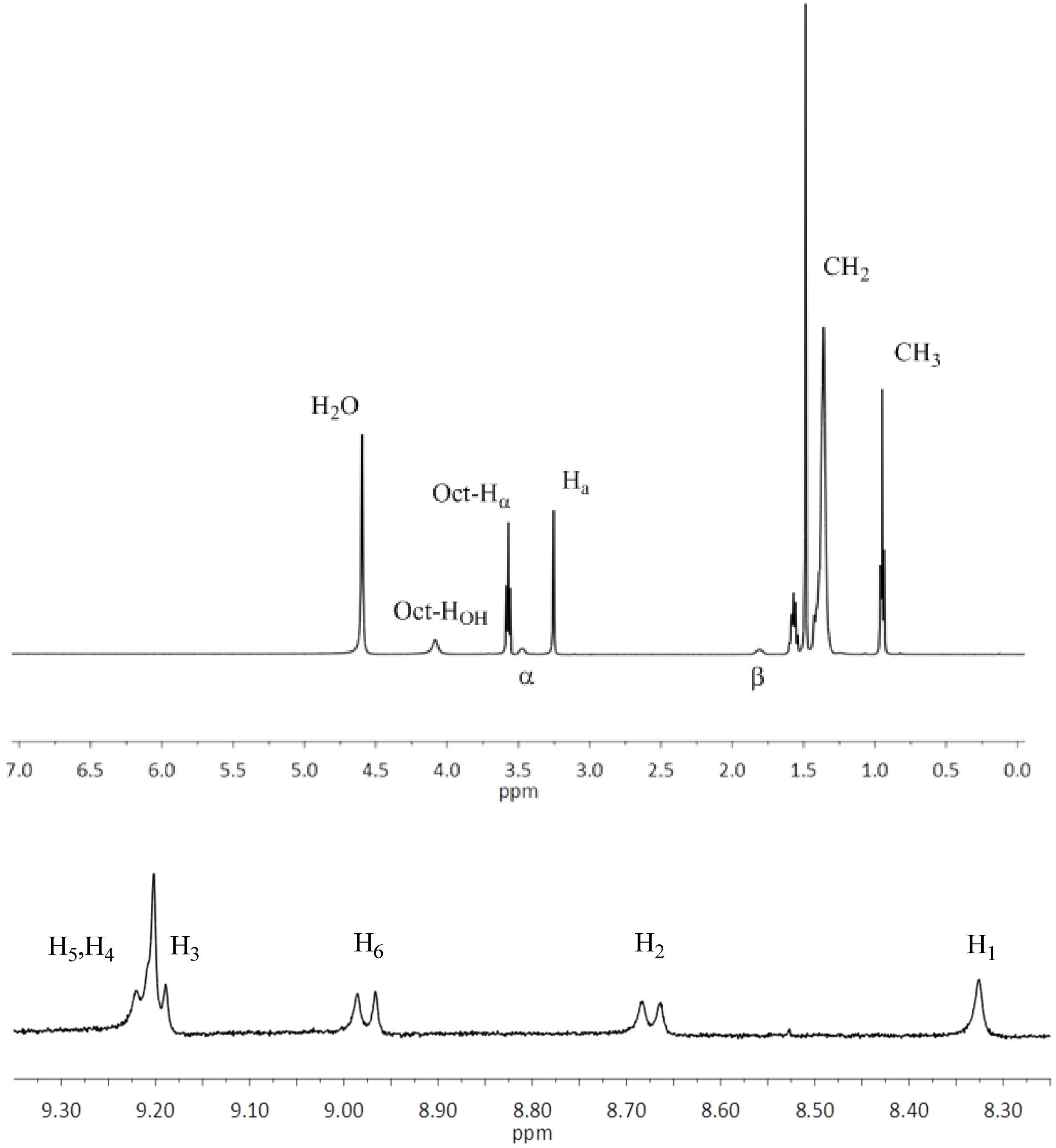

Figure 5.4 ^{1}H NMR spectrum of HPTS in water/CTAB/*n*-octanol/cyclohexane reverse micelles with w_0=10. Top: Spectrum showing signals from water/CTAB/*n*-octanol/cyclohexane. Bottom: Expanded (25×) portion showing HPTS signals.

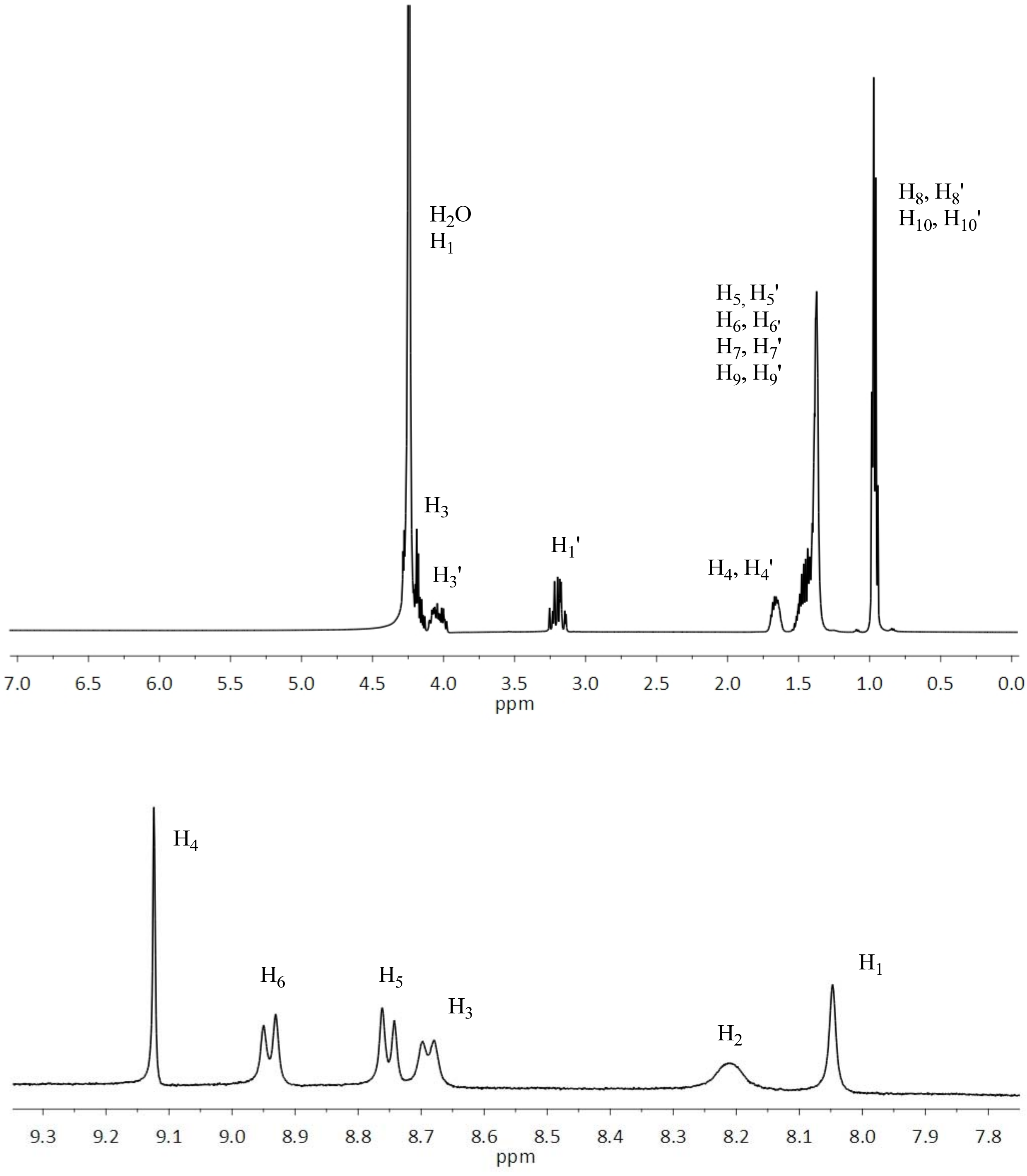

Figure 5.5 ^{1}H NMR spectrum of HPTS in water/AOT/cyclohexane reverse micelles with w_0=10. Top: Spectrum showing signals from water/AOT/cyclohexane reverse micelle. Bottom: Expanded (25×) portion showing HPTS signals.

5.3 Results and Discussion

Broadband ultrafast time-resolved transient absorption spectra were measured for HPTS in AOT, Igepal CO-520, and CTAB RMs as well as in bulk aqueous solution. Briefly, a 400 nm light pulse excites the HPTS molecule, which is subsequently probed by a delayed white light continuum pulse; complete spectra are collected following photoexcitation. Modulating the pump beam reveals the change of absorption. Spectrograms reflecting changes in intensity as a function of time and wavelength were collected for pump beam polarizations both parallel and perpendicular to the probe beam polarization.

Figure 5.6 shows transient absorption data for HPTS in aqueous solution, and in AOT and CTAB RMs. In aqueous solution (top panel) the onset of increased absorption between 500 and 600 nm marks the deprotonation of the molecule. The HPTS dynamics in w_0=20 AOT RMs are nearly indistinguishable from the response in bulk water. In contrast, the transient spectra of HPTS in large CTAB RMs, w_0=40 and Igepal CO-520 RMs, w_0=20 show no spectral shifting or evidence for dye deprotonation. The environment of HPTS in CTAB and Igepal CO-520 RMs appear to block proton dissociation.

Figure 5.7 shows the time-dependent anisotropy signals measuring HPTS molecular reorientation dynamics inside CTAB, AOT, and Igepal CO-520 RMs and in bulk aqueous solution. The HPTS anisotropy decays much more slowly in CTAB RMs and Igepal CO-520 RMs than in bulk aqueous solution or in AOT RMs. The signals appear to plateau indicating that the rotational diffusion is incomplete on the experimental time scale. A wobbling-in-a-cone analysis (see supporting information) reveals that the HPTS molecule is confined to a cone angle

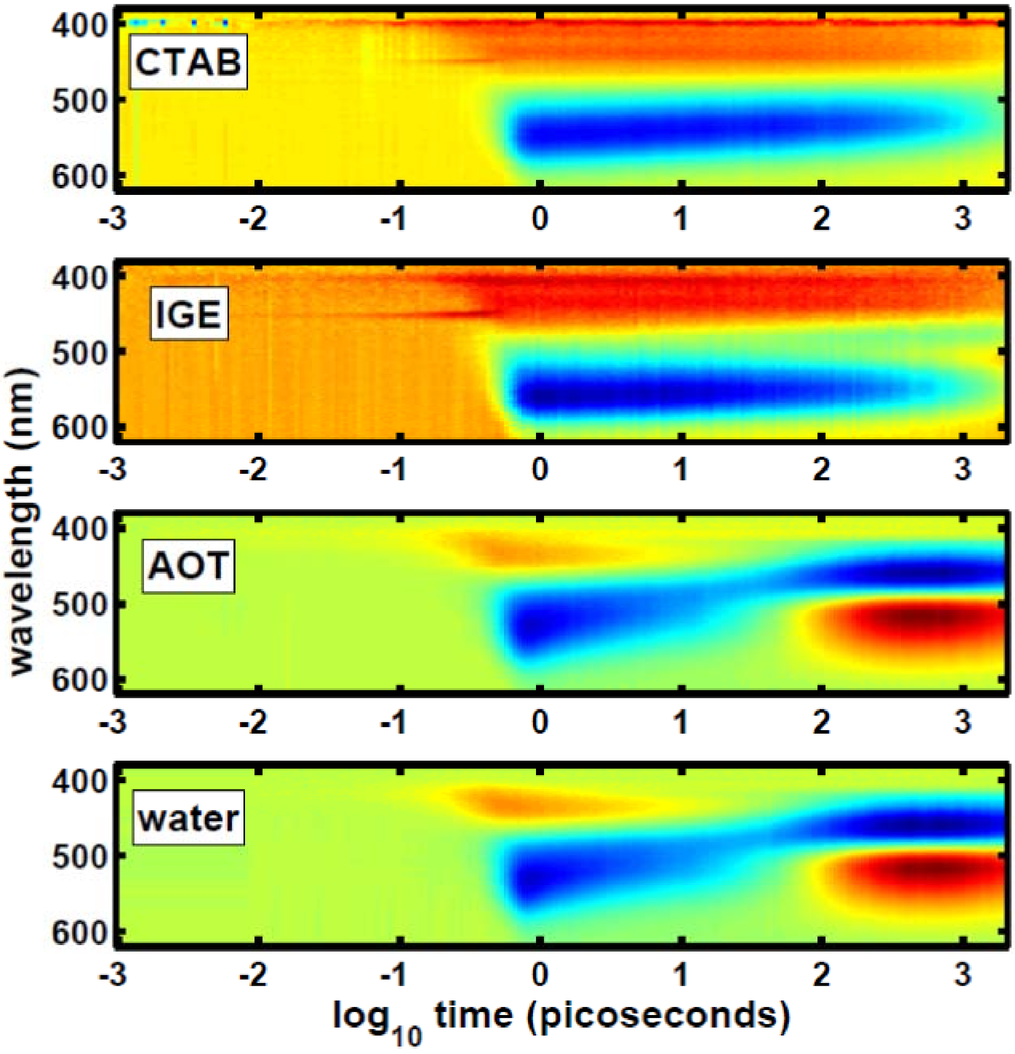

Figure 5.6 Comparison of BFTA spectrograms of HPTS in the largest CTAB, IGE, and AOT RM investigated (w_0 = 40, 20, 20 respectively) and in bulk water. Red hues indicate positive signals (excited state absorption, ESA) and blue hues indicate negative signals (stimulated emission/ground state bleach, SE/BL). Bulk-like behavior is observed only for HPTS in AOT RM. (Note the logarithmic time scale for the x-axis).

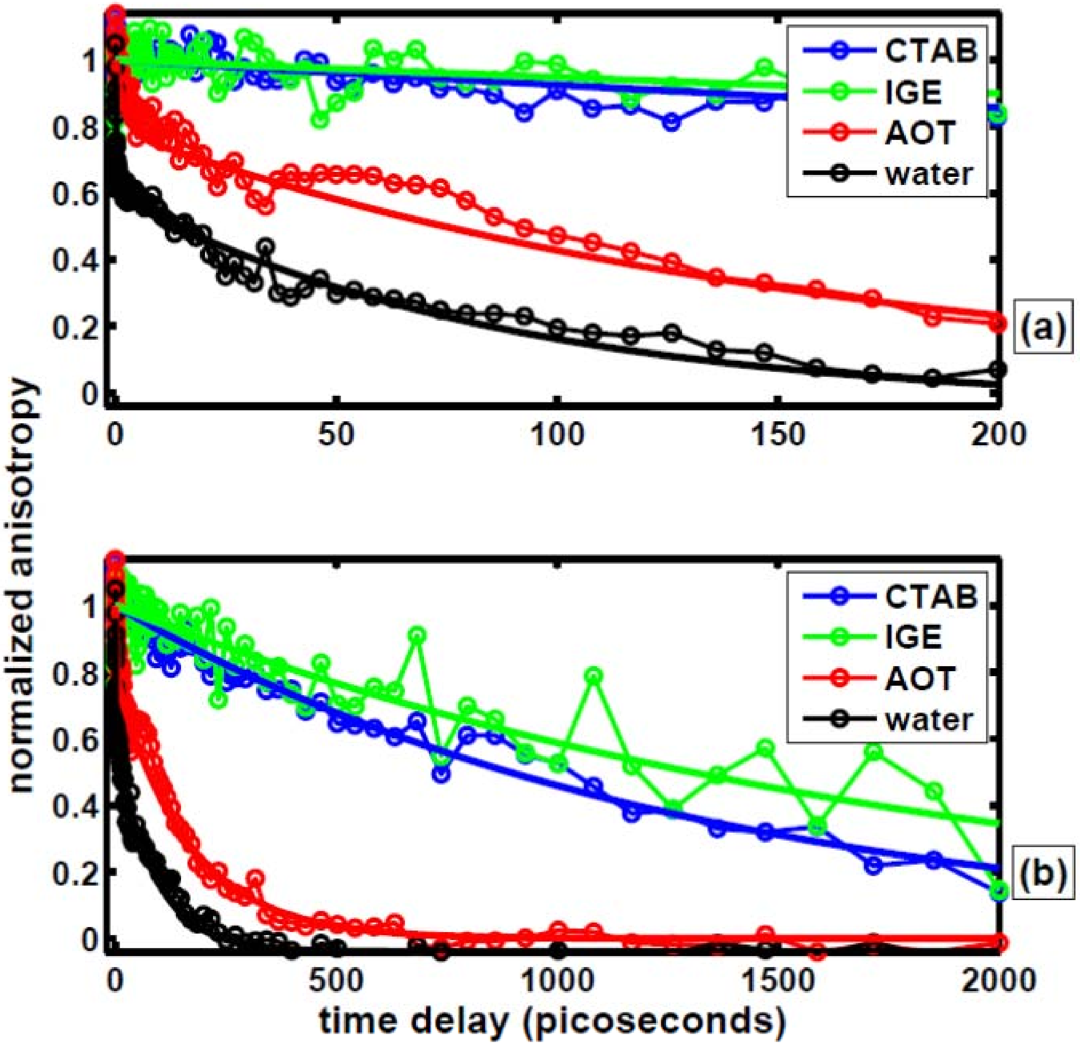

Figure 5.7 Comparison of HPTS anisotropy decays in the largest CTAB, IGE, AOT RM investigated (w_0 = 40, 20, 20 respectively) and in bulk water. Solid lines are biexponential fits to the data. HPTS reorientational motion is severely hindered in large IGE, CTAB RM with respect to bulk reorientational motion while HPTS reorientational motion in large AOT RM approaches bulk behavior.

of ~22°. Although slightly slower than bulk aqueous solution, the HPTS reorientation in the AOT RMs is much faster than the other two environments and resembles that observed in the bulk aqueous solution.

Various explanations can account for the differences in dynamics observed for HPTS in AOT, CTAB, and Igepal CO-520 RMs. The slow anisotropy decay times and missing proton transfer signal from HPTS in CTAB and Igepal CO-520 RMs vs. the fast reorientational decay times and proton transfer dynamics similar to bulk water for AOT suggest HPTS samples significantly different environments in these systems. Time-resolved spectroscopy only indicates dramatically different dynamics, but 2D NMR spectroscopy allows evaluation of HPTS environments. By frequency labeling the spins on specific HPTS hydrogen atoms, NMR NOESY follows the spin population transfer from one atom to another in close proximity, showing when atoms are near to each other.[34] Previous reports[35,36,37,38] have demonstrated NMR NOE as an effective method to identify interactions of small molecules with micelles.

Through 2D NOESY experiments, we measured the interaction of protons in HPTS with protons in RMs. Figure 5.8 shows many cross peaks in the 2D NOESY spectrum of HPTS in the same w_0=10 CTAB RMs used for ultrafast transient absorption measurements. The off-diagonal or cross peaks, arise from intra- and intermolecular interactions. The HPTS NMR signals from protons on aromatic groups appear from ~8.3 to 9.3 ppm and are well separated from all the peaks associated with the RM, that is, water, CTAB surfactant, 1-octanol co-surfactant and cyclohexane. Figure 5.8 near 8.3 ppm on the F2 axis shows cross peaks arising from the interaction of HPTS H_1 with (right to left) H-atoms of the CTAB H_d/1-octanol H_δ, 1-octanol H_α, CTAB headgroup H_a, 1-octanol OH, and water (following the numbering given in Figure 1). Strong interactions also appear for F2≈9.2 ppm (HPTS $H_3/H_4/H_5$) with CTAB H_d/1-octanol H_δ,

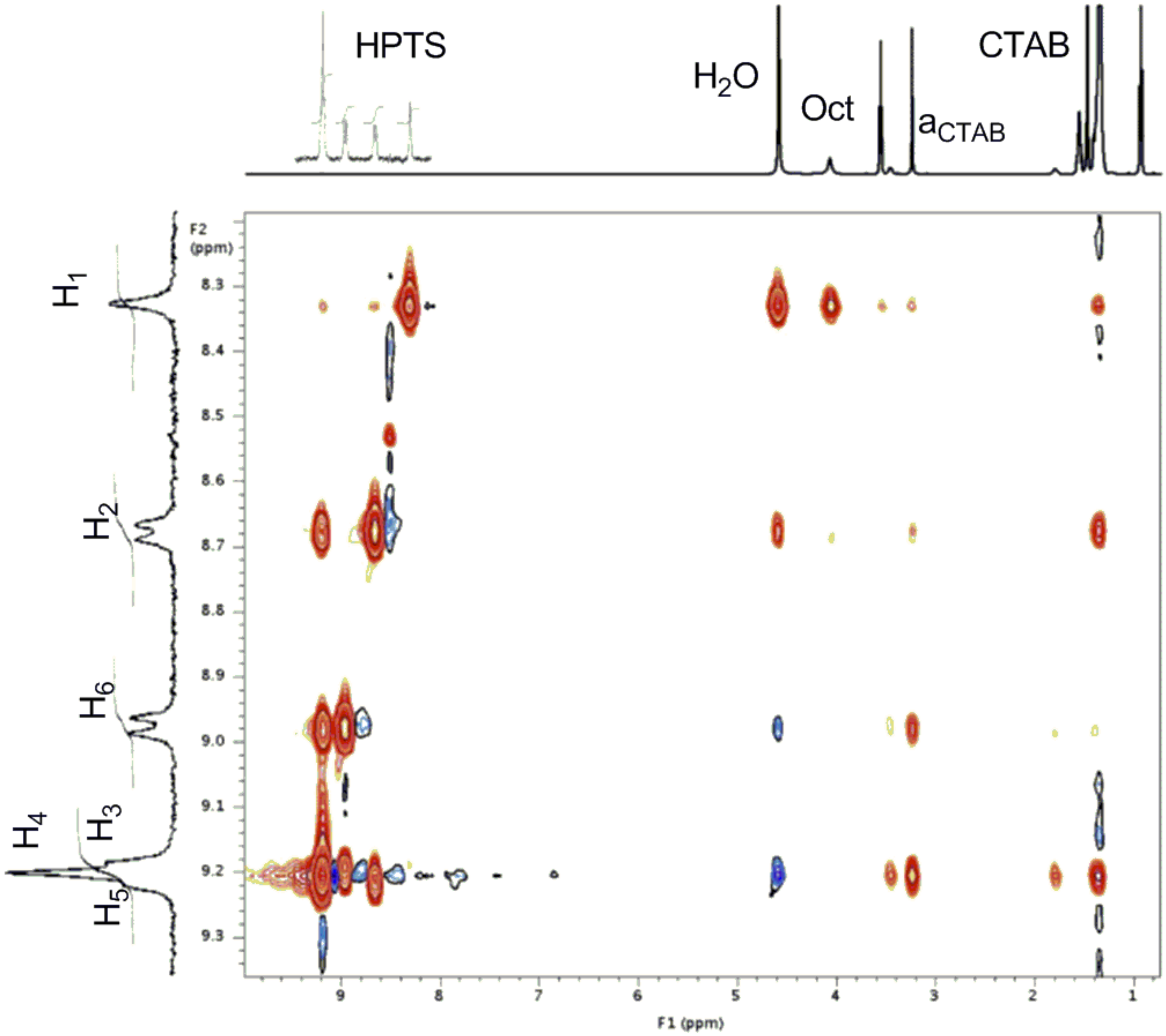

Figure 5.8 2D NOESY spectrum showing interactions between HPTS with w_0 =10 CTAB RM solution. Orange indicates positive peaks; blue indicates negative peaks. Note that the diagonal peaks are orange. The F2 axis is along the vertical or left side of the spectrum.

CTAB H_c, H_a, H_b, and with water. Near 9.0 ppm the HPTS H_6 displays strong cross peaks with CTAB H_a and water, and weaker signals with CTAB H_d/1-octanol H_δ, and CTAB H_b and H_c. Finally HPTS H_2 signals near 8.7 ppm on F2 show strong interactions with CTAB H_d/1-octanol H_δ, and water, and weaker interactions with H_a and 1-octanol OH. To generate these correlations, the HPTS would need to reside embedded in the CTAB RM interface, potentially as drawn in Figure 5.9.

Corresponding 2D NMR experiments on AOT, Figure 5.10 showed only intramolecular interactions between HPTS protons as well as cross peaks reflecting intermolecular interactions between HPTS and water protons No cross peaks were observed between HPTS and AOT or cyclohexane protons. These results demonstrate that HPTS does not interact with the protons forming the interface of the AOT RMs. Instead, HPTS resides well separated from the amphiphiles at the interface.

The 2D NMR experiments on Igepal CO-520 RMs, Figure 5.11, showed interactions intramolecular cross peaks corresponding to HPTS and off-diagonal signals arising from interactions between HPTS and water protons, as well as HPTS and the polyethylene glycol head group of Igepal CO-520. In Chapter 3, we observed that in when a probe is located in the water pool of the Igepal CO-520 RM, there is little interaction with the polar head group. These results demonstrate that the HPTS does not deeply imbed itself in the interface, but is most likely associating with the head group of the Igepal CO-520 RMs.

The sign of the NOE reflects the correlation time for the molecules and/or supramolecular structures giving rise to the NMR signals therefore suggesting the orientation of the HPTS at the CTAB RM interface. The H_1/H_2 HPTS/water interactions lead to a positive

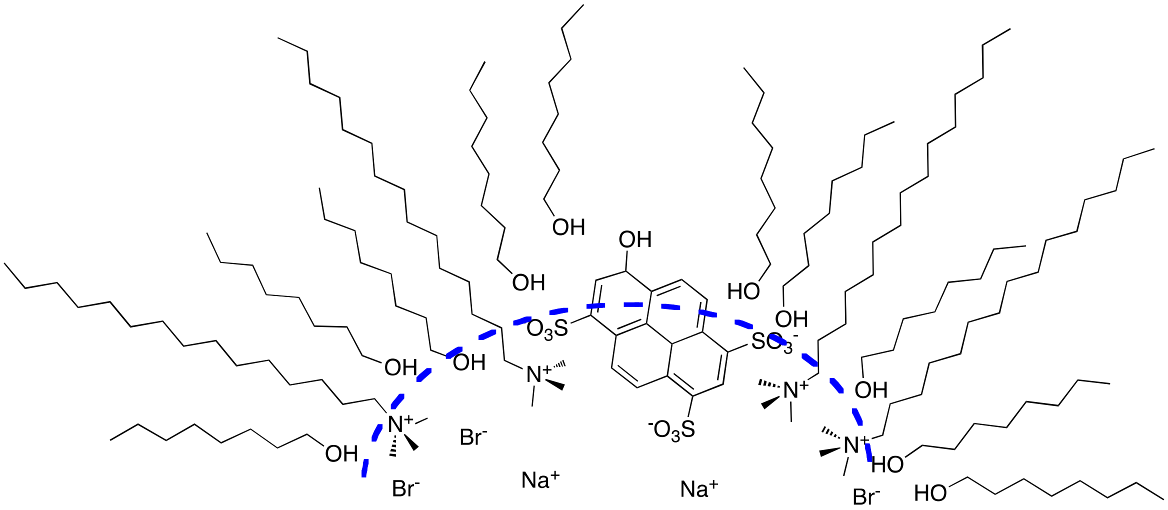

Figure 5.9 Cartoon suggesting a possible orientation of HPTS embedded in the CTAB/1-octanol RM interface that would lead to the observed time-resolved spectroscopy and NOESY results.

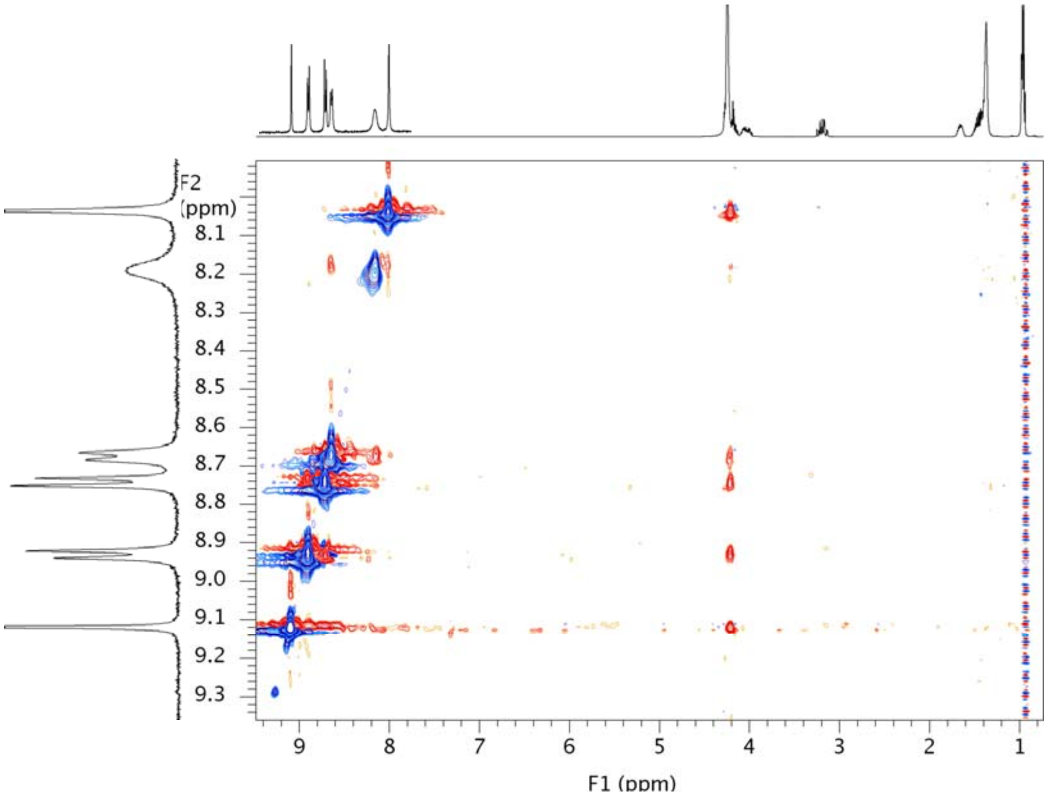

Figure 5.10 ^1H-^1H 2D-ROESY of HPTS in water/AOT/cyclohexane-d_{12} reverse micelle, w_0 = 10. Contour levels are drawn at the noise level accounting for increased artifacts displayed in the plot. Cross peaks are observed between HPTS protons and H_2O protons indicating interactions between HPTS and the reverse micelle water pool but no other cross peaks appear signifying that the HPTS interacts only with water in the sample and not with interfacial surfactant or nonpolar solvent.

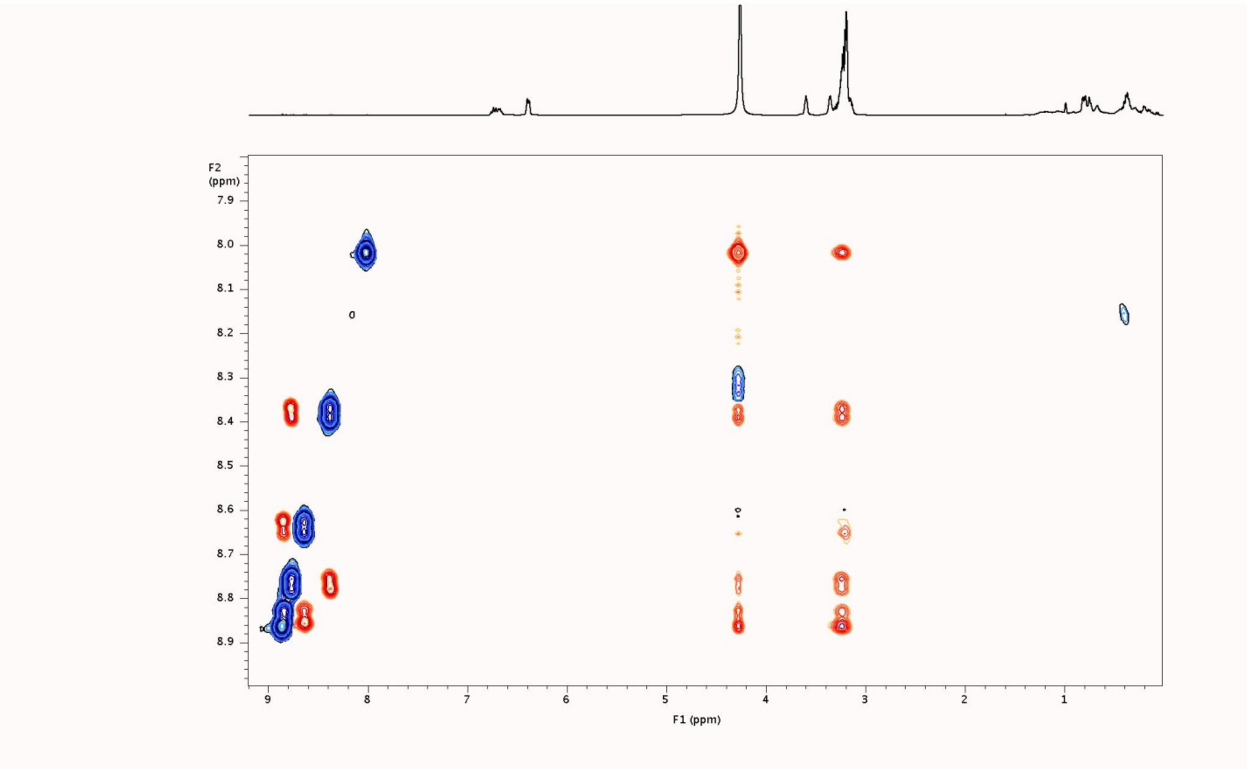

Figure 5.11 ^1H-^1H 2D-ROESY of HPTS in water/Igepal CO-520/cyclohexane-d_{12} reverse micelle, w_0 = 10. Contour levels are drawn at the noise level accounting for increased artifacts displayed in the plot. Cross peaks are observed between HPTS protons and H_2O protons indicating interactions between HPTS and the reverse micelle water pool. Cross peaks are also observed for the head group of Igepal CO-520, indicated HPTS's location to be partially imbedded in the interface.

signal (same sign as diagonal peaks), while a negative signal (opposite sign from diagonal peaks) arises between water and HPTS $H_3/H_4/H_5/H_6$. This shows slower relaxation dynamics contributing to the H_1/H_2 NOEs compared to the $H_4/H_5/H_6$ signals, and consistent with a dramatic difference in the environments sampled by protons on different sides of the HPTS molecule.

Results from our NMR experiments corroborate and explain observations from ultrafast time-resolved transient absorption measurements. In CTAB RMs, HPTS molecules display no deprotonation and slow molecular reorientation. For the same samples, NOESY data show clear interactions of HPTS with water and the CTAB and 1-octanol, molecules comprising the RM interface. Embedding the HPTS molecule into the interface could present an environment that damps the photoinduced deprotonation reaction. Increased acidity reported at RM interfaces[39,40,41] could also favor protonated HPTS but would not lead to the strong interactions between HPTS and molecules of the interface. The signs of the NOE signal for HPTS interactions with water reflect the substantially different correlation times for water sensed by HPTS protons H_1/H_2 compared to $H_3/H_4/H_5/H_6$ and are consistent with the HPTS oriented partially buried in the interface, as shown in Figure 5.9. The negative cross peaks indicate much shorter correlation times for the $H_4/H_5/H_6$ interactions than for H_1/H_2. We assign the positive cross peaks to the OH groups at the water/surfactant interface; negative cross peaks are consistent with the bulk-like water in the interior of the RM. Halliday et al. recently reported distinct NMR signals from the OH groups in water and pentanol in CTAB/pentanol RMs[41] which we have also observed. This contrasts observations for bulk aqueous solutions where signals coalesce because of the rapid chemical exchange. Considering the positive and negative NOE signals shown in Figure 5.8, we propose that the HPTS molecule is partially buried in the interface, as depicted in Fig. 5.9, possibly due to the Coulomb attraction between the negatively charged SO_3^- groups on HPTS with the positively charged CTAB headgroups. It may seem unlikely to find a highly charged molecule like HPTS buried in the RM interface. However, through NMR NOE measurements, we demonstrated the $VO_2(dipic)^-$ molecule comfortably embedded in AOT RM interfaces.[38] Likewise, Binks et al. have observed interactions between the bipyridyl groups of the $Ru(II)(bpy)_3^{2+}$ molecule with AOT methyl protons.[42] In contrast, HPTS in AOT RMs behaves much like it does in bulk aqueous solution. That is, we observe no HPTS interactions with surfactant protons in the AOT RM interface and only negative NOE signals indicating that HPTS interacts with bulk-like water in the RM core. Ultrafast anisotropy measurements agree and indicate HPTS molecules in AOT RMs reside separated from the interface, well solvated by the RM water pool. This most likely reflects Coulomb repulsion between SO_3^- groups on both HPTS and the AOT headgroups. HPTS inside Igepal CO-520 RMs show behavior similar to that of CTAB reverse micelles. However, as a nonionic surfactant, Igepal CO-520 no Coulombic interactions exist between the HPTS and the head group of the surfactant. The ultrasfast anisotropy data for Igepal CO-520 suggest that the HPTS molecules have restricted motion, and the 2D NMR experiment shows interactions between the headgroup of Igepal CO-520 and HPTS. From our previous work reported in Chapter 3, we know that a true water pool forms in the interior of Igepal reverse micelles and our data imply that the PEO surfactant head groups are not highly hydrated. The 2D NMR data suggest that the HPTS molecules embed in the region of the PEO groups. This nonaqueous environment would tend to block proton dissociation from the HPTS molecules, as observed in the transient absorption spectrograms. Embedding in the interface would also lead to reduced rotational motion of the HPTS molecules.

Our results demonstrate how complementary methods lead to detailed understanding of probe environment. Ultrafast time-resolved transient absorption measurements of HPTS in CTAB RMs show unequivocally that the environment impacts the dynamics, but do not reveal specific structures leading to the observed effects. Likewise, NOESY NMR measurements reveal details about the interaction of HPTS and RMs.

5.4 References

(1) Cole, R. L., PhD Dissertation, 2011.

(2) Thompson, W. H. In *Annual Review of Physical Chemistry, Vol 62*; Leone, S. R., Cremer, P. S., Groves, J. T., Johnson, M. A., Eds. 2011; Vol. 62, p 599.

(3) Kreuer, K. D. *Chem. Mat.* **1996**, *8*, 610.

(4) Michel, H.; Behr, J.; Harrenga, A.; Kannt, A. *Annual Review of Biophysics and Biomolecular Structure* **1998**, *27*, 329.

(5) Wraight, C. A. *Biochim. Biophys. Acta-Bioenerg.* **2006**, *1757*, 886.

(6) Spry, D. B.; Fayer, M. D. *J. Phys. Chem. B* **2009**, *113*, 10210.

(7) Tielrooij, K. J.; Cox, M. J.; Bakker, H. J. *ChemPhysChem* **2009**, *10*, 245.

(8) Mondal, T.; Das, A. K.; Sasmal, D. K.; Bhattacharyya, K. *J. Phys. Chem. B* **2010**, *114*, 13136.

(9) Sen Mojumdar, S.; Mondal, T.; Das, A. K.; Dey, S.; Bhattacharyya, K. *J. Chem. Phys.* **2010**, *132*.

(10) Bardez, E.; Goguillon, B. T.; Keh, E.; Valeur, B. *Journal of Physical Chemistry* **1984**, *88*, 1909.

(11) Pines, E.; Huppert, D.; Agmon, N. *J. Chem. Phys.* **1988**, *88*, 5620.

(12) Tran-Thi, T. H.; Gustavsson, T.; Prayer, C.; Pommeret, S.; Hynes, J. T. *Chem. Phys. Lett.* **2000**, *329*, 421.

(13) Roy, D.; Karmakar, R.; Mondal, S. K.; Sahu, K.; Bhattacharyya, K. *Chemical Physics Letters* **2004**, *399*, 147.

(14) Ghosh, S.; Dey, S.; Mandal, U.; Adhikari, A.; Mondal, S. K.; Bhattacharyya, K. *J. Phys. Chem. B* **2007**, *111*, 13504.

(15) Amdursky, N.; Orbach, R.; Gazit, E.; Huppert, D. *J. Phys. Chem. C* **2009**, *113*, 19500.

(16) Cox, M. J.; Siwick, B. J.; Bakker, H. J. *ChemPhysChem* **2009**, *10*, 236.

(17) Barrash-Shiftan, N.; Brauer, B.; Pines, E. *J. Phys. Org. Chem.* **1998**, *11*, 743.

(18) Hutter, T.; Presiado, I.; Ruschin, S.; Huppert, D. *Journal of Physical Chemistry C* **2010**, *114*, 2341.

(19) Mukherjee, T. K.; Ahuja, P.; Koner, A. L.; Datta, A. *Journal of Physical Chemistry B* **2005**, *109*, 12567.

(20) Barnadas-Rodriguez, R.; Estelrich, J. *Journal of Physical Chemistry B* **2009**, *113*, 1972.

(21) Levinger, N. E.; Swafford, L. A. *Annual Review of Physical Chemistry* **2009**, *60*, 385.

(22) De, T. K.; Maitra, A. *Adv. Colloid Interface Sci.* **1995**, *59*, 95.

(23) Giustini, M.; Palazzo, G.; Colafemmina, G.; DellaMonica, M.; Giomini, M.; Ceglie, A. *J. Phys. Chem.* **1996**, *100*, 3190.

(24) Zhu, D. M.; Feng, K. I.; Schelly, Z. A. *J. Phys. Chem.* **1992**, *96*, 2382.

(25) Walde, P.; Giuliani, A. M.; Boicelli, C. A.; Luisi, P. L. *Chem. Phys. Lipids* **1990**, *53*, 265.

(26) Spry, D. B.; Goun, A.; Glusac, K.; Moilanen, D. E.; Fayer, M. D. *Journal of the American Chemical Society* **2007**, *129*, 8122.

(27) Tokmakoff, A. *J. Chem. Phys.* **1996**, *105*, 1.

(28) Cole, R. L.; Barisas, B. G.; Levinger, N. E. *Review of Scientific Instruments* **2010**, *81*, 093101.

(29) Cole, R. L.; Colorado State University, Fort Collins CO, USA: 2011.

(30) Kinosita, K.; Kawato, S.; Ikegami, A. *Biophys. J.* **1977**, *20*, 289.

(31) Lipari, G.; Szabo, A. *Biophys. J.* **1980**, *30*, 490.

(32) Stahla, M. L.; Baruah, B.; James, D. M.; Johnson, M. D.; Levinger, N. E.; Crans, D. C. *Langmuir* **2008**, *24*, 6027.

(33) Delaglio, F.; Grzesiek, S.; Vuister, G. W.; Zhu, G.; Pfeifer, J.; Bax, A. *J. Biomol. NMR* **1995**, *6*, 277.

(34) Neuhaus, D.; Williamson, M. P. *The nuclear Overhauser effect in structural and conformational analysis*; 1st ed.; VCH: New York, N.Y., 1989.

(35) Bachofer, S. J.; Simonis, U.; Nowicki, T. A. *J. Phys. Chem.* **1991**, *95*, 480.

(36) Sabatino, P.; Szczygiel, A.; Sinnaeve, D.; Hakimhashemi, M.; Saveyn, H.; Martins, J. C.; Van der Meeren, P. *Colloid Surf. A-Physicochem. Eng. Asp.* **2010**, *370*, 42.

(37) Ceraulo, L.; Fanara, S.; Liverib, V. T.; Ruggirello, A.; Panzeri, W.; Mele, A. *Colloid Surf. A-Physicochem. Eng. Asp.* **2008**, *316*, 307.

(38) Crans, D. C.; Rithner, C. D.; Baruah, B.; Gourley, B. L.; Levinger, N. E. *J. Am. Chem. Soc.* **2006**, *128*, 4437.

(39) Baruah, B.; Roden, J. M.; Sedgwick, M.; Correa, N. M.; Crans, D. C.; Levinger, N. E. *J. Am. Chem. Soc.* **2006**, *128*, 12758.

(40) Sedgwick, M. A.; Crans, D. C.; Levinger, N. E. *Langmuir* **2009**, *25*, 5496.

(41) Halliday, N. A.; Peet, A. C.; Britton, M. M. *J. Phys. Chem. B* **2010**, *114*, 13745.

(42) Binks, D. A.; Spencer, N.; Wilkie, J.; Britton, M. M. *J. Phys. Chem. B* **2010**, *114*, 12558.

APPENDIX A

INDEPENDENT RESEARCH PROPOSAL

TRANSDERMAL DETECTION OF HIV-1

A.1 Specific Aims:

A.1a Specific Aim 1: Development of a Spatially Offset Coherent Anti-Stokes Raman Microscope

This instrument will combine the technique of spatially offset Raman spectroscopy (SO) with the signal enhancement gained with coherent anti-Stokes Raman spectroscopy (CARS). This instrument will work in a similar fashion to standard CARS microscope, except it will have a translational component on it, to utilize the spatially offset Raman signal. Development of this device will focus on determining the maximum and minimum number of translational steps and translational distance needed to get the desired resultant signal.

Using spatially offset coherent anti-Stokes Raman microscopy (SO-CARM), we will determine the chemical composition of a standard sample volume under a visually opaque (400-800 nm) surface. By using infrared light, we can probe the sub-surface and gain chemical information about why lies beneath the surface.

After the SO-CARM instrument has been demonstrated with standard solutions, in vitro biological samples will be measured. These measurements will show the efficacy of the technique for biological samples in vivo. Samples of blood containing HIV-1 and samples devoid of HIV will be compared using this technique to show the ability of the device to determine the differences between each of the blood samples.

A.1.b Specific Aim 2: Determining Infection of Feline Specimens with the Feline Immunodeficiency Virus

By using SO-CARM we will be able to determine in feline species whether or not they are infected with feline immunodeficiency virus (FIV). By placing the translation stage of the SO-CARM perpendicular to a major artery and having it scan into the artery, we expect to be able to detect a difference in the resultant Raman signal when the microscope is over the artery and when it is in close proximity to it. By analyzing the spectrum from a configuration with the SO-CARM is over the artery, we will be able to determine the part of the spectrum that is a result of the blood and that which arises from the rest of the sample volume (skin, hair, fat, etc...) If the cat is infected with FIV, there will be clear markers in the Raman spectrum which will be evident after subtracting the non-blood components of the sample volume.

A.1.c Specific Aim 3: Determining Infection of Human Subjects with HIV

The SO-CARM in this experiment will be placed perpendicular to the human carotid artery, to maximize the volume of blood near the surface. Scanning will then commence, traversing the carotid artery, before stopping. Once again, the volume that has mostly blood (carotid artery volume) will be compared to that of the area near artery. Once the blood component of the spectrum has been characterized, it will be compared against known Raman markers of HIV in human blood.

A.2 Background and Significance:

A.2.a HIV

In their 2008 report on the global AIDS epidemic, the United Nations reported that 0.6% of the world's population is infected with a form of the Human Immunodeficiency Virus (HIV).[1]This number increases to almost 7% in certain regions of sub-Saharan Africa.[1] Because HIV is a lentivirus, or slow acting virus, transmission can easily occur.[2] Early detection of the virus is needed in order to stop this pandemic.[3]

HIV infection goes through four main stages: incubation, acute infection, latency, and Acquired Immunodeficiency syndrome (AIDS)[2]. Incubation usually takes around 3 weeks; individuals are asymptomatic and at a reduced chance to spread the virus. When the individual reaches the acute infection stage, infected individuals show signs of fever, malaise, muscle pain, and swollen lymph nodes. This is usually assumed to be an infection or the flu. After the acute stage, the individual goes into the latency or dormant stage. Here the individual can stay for 2 weeks to 40+ years. This is the most dangerous stage for transmission because the individuals are usually asymptomatic but infectious at the same time. Once the individual reaches the fourth and final stage, AIDS, opportunistic infections start to settle in and the individual will usually succumb to one or many at a given time.

HIV is a highly adaptive virus, and is easily mutated.[4,5] There are two main types of HIV: HIV-1 which is the most common and easily transmitted strain of the virus and HIV-2 which is primarily found in Africa.[1] HIV-2 was not seen outside of Africa until 1987. The Stanford HIV reverse transcriptase and Protease Sequence Database tracks and catalogs these variations.

The ability to detect the HIV virus is critical in stopping the spread of this deadly virus. The prominent test for HIV now uses the Western Blot to look for specific HIV antibodies.[6] The major problem with this test is the length of time it takes from when the person is infected to when large enough amounts of antibodies are present to be detected. This window is usually between 3-6 months. In the meantime, if an individual believes they may have contracted the virus, they will have to wait 3 months before they can test for it, due to the false negatives that can occur.[6] The instrument proposed here provides a way to detect the virus directly, so that the time an individual needed to wait from exposure to test could be reduced, thus greatly reducing the chance for further transmission to other individuals. There are quick, home tests available, but these have received a lot of scrutiny due to high rate of false positives.[7] In fact New York City has reverted back to whole blood screenings as opposed to the fast home tests in 2008.[7]

One direct way to test for the virus is to probe for something that is associated with the structure of the virus itself. Three predominant glycoproteins are our main targets, the gp120 gp41 and gp24 proteins. The gp120 and gp41 protein are used in the virus's mechanism for entering a cell.[8] On each virus there are about 300 copies of these glycoproteins. The other choice, the gp24 protein is a transmembrane protein in the viral coat. There are over 2000 copies of this protein, per virus, making it ideal for targeting.[8] Many drugs have targeted these proteins, since they are essential to the virus's replication cycle.[8]

A.2.b Spatially-Offset and Coherent Anti-Stokes Raman Spectroscopy

Currently, there are a 2 main classes of techniques available for determining if a patient is infected with HIV. The first class, which is also the most widely used, is the antibody tests. Antibody tests rely on the patient's body to create antibodies to the virus and then detect them with viral antigens. The most commonly used antibody test is Enzyme-linked immunosorbent assay (ELISA). This test requires blood be drawn and separated. The patient's serum is then applied to a plate with HIV antigens on it. If there are HIV antibodies present they will bind to these antigens. The plates are then cleaned and then a spectroscopicly tagged secondary antibody is introduced to bind to all the remaining antigen sites. A substrate is then introduced that binds to the spectroscopic tag on the antibody, resulting in either a color change or fluorescence signal. This technique is highly accurate, but can lead to a number of "false positives" due to a lack of clearly defined negative/positive result boundaries. [9]ELISA also requires a patient's blood to be drawn, which if the patient is infected with HIV, could become a potential threat to the person drawing the blood. The other class of detection techniques is nucleic acid based techniques. In this class of techniques, detection of a 142 base target sequence is performed. This region in the viral DNA is studied due to the fact that this region is present in most forms of the virus. Polymerase chain reaction (PCR) is used to amplify the viral DNA present. The DNA sequence is then placed in the presence of specific primers to replicate the viral DNA. A spectroscopic tag is then added that will only bind to the viral DNA. Given the cost of the technique, it is no longer used. ELISA can give similar results and is inexpensive in comparison to nucleic acid detection.

The antibody techniques detect the body's response to HIV and not the virus directly. This can become problematic in early infection, as the body hasn't built up sufficient antibodies to be detected. Both techniques are time consuming and require the patient's blood to be drawn, which leads to possible contamination and even transmittance of the disease itself. The ability to detect the virus directly in-vivo would alleviate all of the drawbacks to the techniques listed above. One such technique is Raman spectroscopy. Every molecule has a unique Raman signal, which will allow us to detect the virus directly, as opposed to detecting the body's response to the virus.

In order to get an in-vivo Raman signal that is not overwhelmed by signals that are not of interest, one can employ spatially-offset Raman spectroscopy.[10] Spatially offset Raman spectroscopy makes at least two Raman measurements, one in the place of interest and one or more measurements a few millimeters away as depicted in Figure A.1. In figure A.1, there are two media that contribute a Raman signal, one being the bulk media and the other being the purple mass located in the center. When a Raman signal is collected at arrows 1 and 3, there is only one component to the system and thus only one Raman signal present. But, when we look at the Raman signal from arrow 2, we can see the Raman signal from the bulk medium, but we can also a see a contribution from the purple mass. By analyzing the data from arrows 1, 2, and 3 and subtracting spectrum 1 or 3 from spectrum 2 we can obtain a spectrum of just the purple mass, removing most of the signal arising from the bulk medium.

Spatially offset Raman spectroscopy enables collection of vibrational spectra arising from species located in spatially separated locations. However, Raman spectroscopy does not offer the sensitivity necessary to a allow us to observe Raman signals from species at relatively low concentrations. Since the goal is to use this technique to observe viruses in the human body, which have very low concentrations (10,000 replicants per mL)[11], we will need to couple spatially offset Raman with a method to increase the signal of the analyte. Coherent anti-Stokes Raman spectroscopy (CARS) is a common technique in Raman spectroscopy and can yield a significant increase in the signal to noise compared to a typical standard Raman spectroscopy experiment.[12] CARS works slightly differently than typical Raman spectroscopy in that it is a coherent technique.

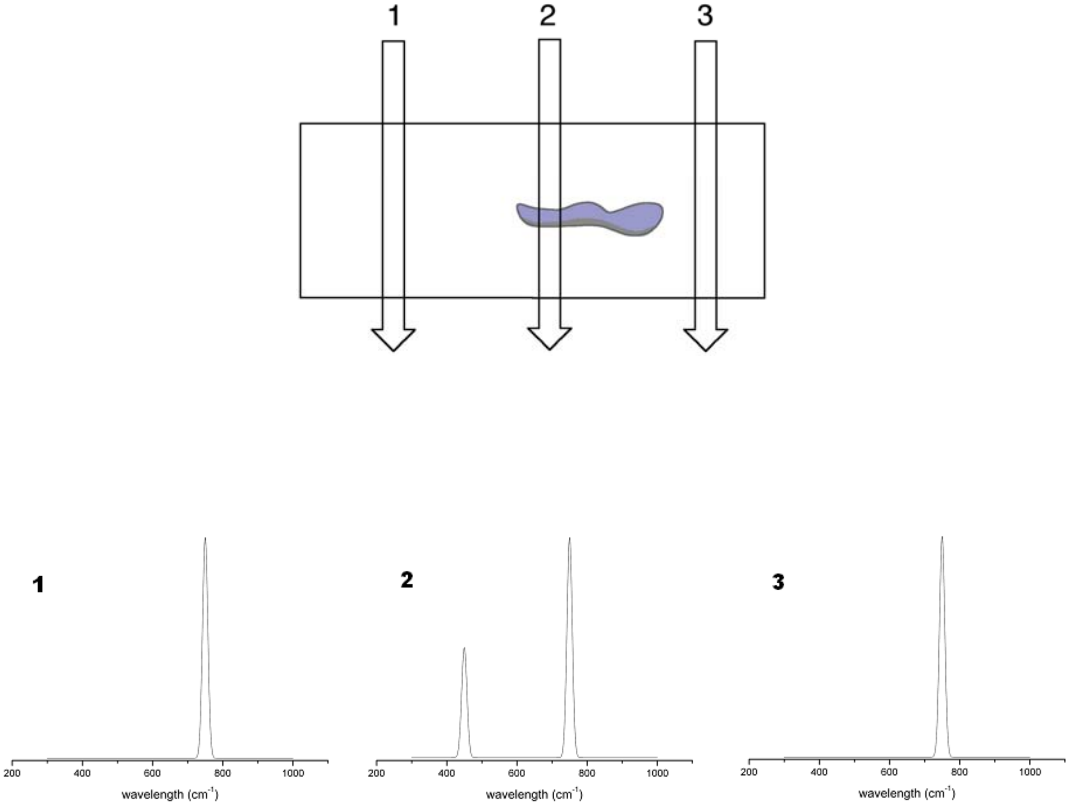

Figure A.1 (a) A schematic of a region that will undergo spatially offset Raman spectroscopy. Each hollow arrow indicates a specific spatial location where the Raman signal will be collected. Locations 1 and 3 collect only background signals while location 2 collects signal from the purple species as well as background. (b) The simulated Raman spectra corresponding to data collection at locations 1, 2 and 3 in part (a). Spectrum 2 shows a stimulated Raman spectrum of both the purple species and the background, where in Spectrum 1 and 3 there is only a Raman spectrum of the background.

In Figure A.2 we can see that CARS requires 3 laser pulses: a pump pulse, a Stokes emission pulse, and a probe pulse. The pump is a narrow bandwidth pulse that excites most of the molecules from a ground state to a virtual state. Then a spectrally broad Stokes emission pulse enters the sample and the molecules undergo stimulated Stokes Raman emission. Now the molecules are vibrating coherently. The probe pulse will enter sample and excite the molecules to a different virtual state. Once the molecules decay from that virtual state, we can then detect the anti-Stokes signal. We look at the anti-Stokes signal due to the overwhelming amount of fluorescence that occurs in the same region as the Stokes signal.

One of the benefits to using CARS is that it generates a collimated, directional beam, whereas in spontaneous Raman scattering, signal is produced in all directions. Given that all the Raman emission is in this single direction, the intensity of this beam is orders of magnitude larger than its spontaneous Raman counterpart. This increase in the signal to noise is of the technique is going to be critical when observing viruses in the bloodstream, since they low concentrations. In 1982, Manuccia and co-workers developed a microscopy technique utilized CARS, CARM (coherent anti-Stokes Raman microscopy).[14] Unlike optical microscopy, which relies on refractive index changes in a sample, or fluorescence microscopy, which introduces a fluorescent probe, which could perturb the system, CARS microscopy can give chemically specific information about the sample. Standard vibrational microscopies have poor sensitivity due to the low spatial resolution of the infrared light. Standard Raman spectroscopy could be used to distinguish different vibrations in a sample, but high laser powers and the length of the experiment can become damaging to biological systems. In 1999 Xie and co-workers developed

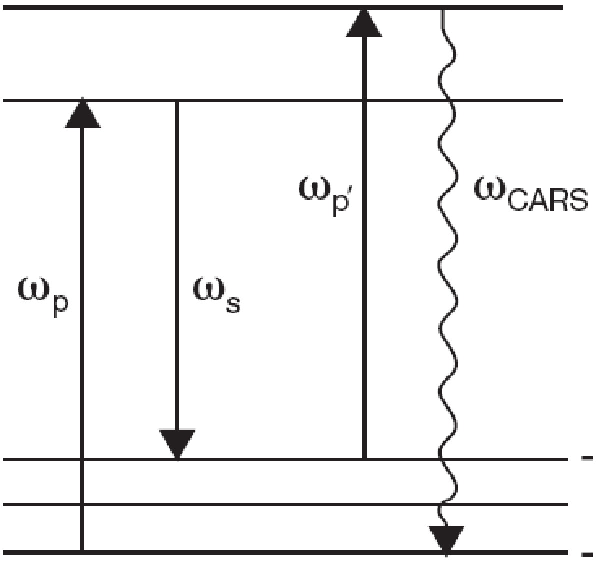

Figure A.2 Diagram of a coherent anti-Stokes Raman experiment (CARS)Where ω_p is the pump pulse, ω_s is the Stokes emission, $\omega_{p'}$ is the probe pulse, and ω_{CARS} is the CARS signal detected.[13]

a real-time imaging CARS microscope. Building off of this device developed by Xie and co-workers we will add the spatially offset component to the device.

By using CARM and SORS together, SO-CARM in one technique, we will be able to observe lower concentration molecules through a non-transparent medium. Once the SO-CARM data is acquired; the background will be subtracted from the blood spectrum. Once the blood spectrum has been separated, it can be compared to a standard spectrum with known Raman signals resulting from carbohydrates and proteins for HIV. Major signals contributions from HIV carbohydrates occur at a Raman shift of 880, 1456 and 2935 cm^{-1}, where contributions from gp 120, gp41 and gp24 occur at a Raman shift of 1048, 1089 and 2883 cm^{-1}(Figure A.3).[15]There is little to no signal from these Raman shifts in blood, Figure A.4, so significant signal from these 6 peaks can be used to indicate infection. Given the strong in-vitro signal from HIV in Figure A.3, CARS microscopy will be able to obtain similar signals in-vivo. By looking at the vibrations of the virus itself, this technique is not impacted by biological variations in the infected patient. The gp120 and gp41 proteins are of particular interest to look for, since they do not change significantly in any known mutations of HIV[16].

Assuming a human subject has a viral load of about 10,000 replicants/mL (common viral loads range from 2000 replicant/mL to upwards of 300,000 replicants/mL [11]) the concentration of the virus in the blood is about 1.67×10^{-17} M. There are roughly 250 copies of the gp120 protein on each virus[16], yielding a concentration of the gp120 protein to be 4.18×10^{-14}. By utilizing CARS microscopy instead of normal Raman, we expect to see an enchantment of our Raman signal of about 10^5, which puts our concentration at about 4.18×10^{-9} which is well within the detection limit of Raman spectroscopy.

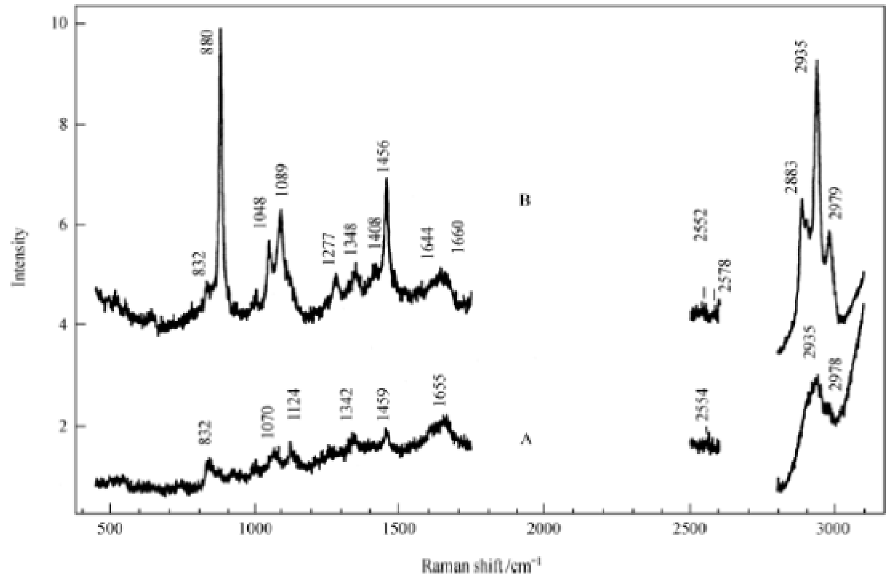

Figure A.3 Raman spectrum of human serum (A) and human serum with the HIV present (B). In spectrum B, peaks at a shift of 880, 1456 and 2935 cm^{-1} are from carbohydrates in the virus, where the peaks at a shift of 1048, 1089 and 2883 cm^{-1} are from the glycoproteins in the virus.[15] These 6 peaks are going to be the points on interest in detecting the virus in vivo.

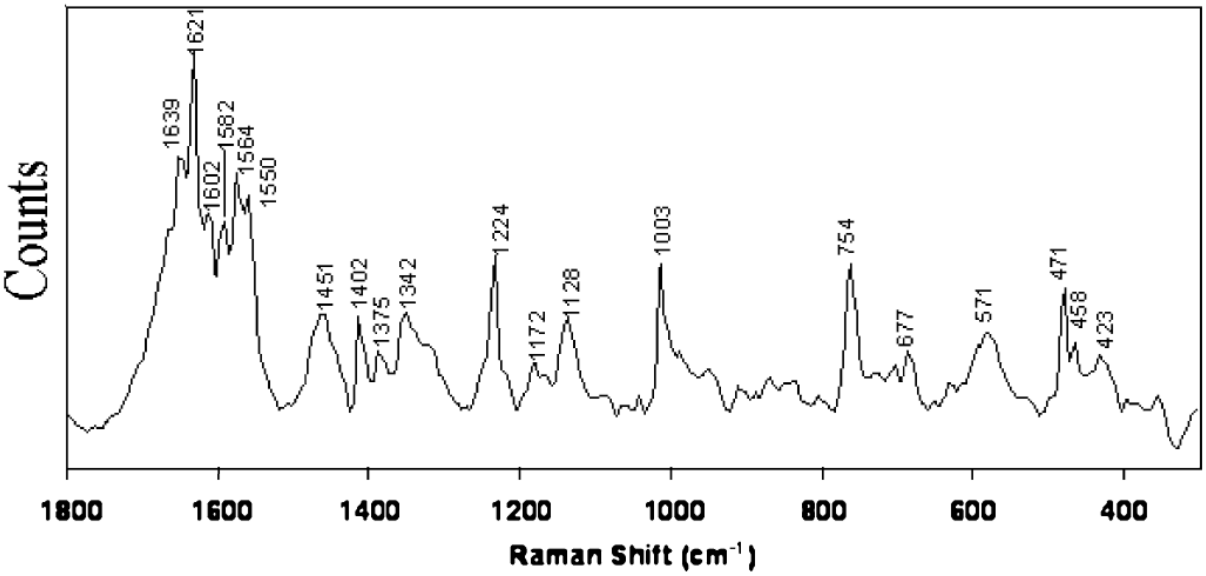

Figure A.4 Resonance Raman spectrum of red blood cells.[17] This spectrum shows that the red blood cells are not going to interfere with the measurements looking for HIV, since most of the HIV peaks are in void regions of this spectrum.

This technique can easily be adapted to look at other diseases that have high viral loads (above 200,000 replicants/mL), such as hepatitis B and C, assuming they have a resolvable Raman spectrum. Once a Raman spectrum is collected from the virus of interest in human serum, we can then use it to compare to the serum that is without the virus of interest. If the spectrum shows differences upon infection, we can then use that spectrum for comparison to determine infection in different samples.

A.3 Experimental Design

A.3.a Aim 1:Development of a spatially offset coherent anti-Stokes Raman microscope

First we will need to adapt a CARS microscope for spatially offset capability for part of the experiment. We will utilize a CARS microscope design developed by Xie and coworkers[18]. (Figure A.5) This instrument uses a 7ps pulsed Nd: vanadate laser(1064nm) which pumps an optical parametric oscillator for the CARS process, $\omega_{p'}$; part of this beam is used as the CARS Stokes beam, ω_p. The light is then focused into a microscope, which is then placed on a point of interest and a CARS signal is obtained. The microscope objective is then moved and another CARS signal is detected. This is repeated multiple times, depending on the experiment, to obtain enough signal variability to do the spatially offset analysis. Using light at 1064nm is a good choice for in vivo studies due to the body's transparency to light at that wavelength.

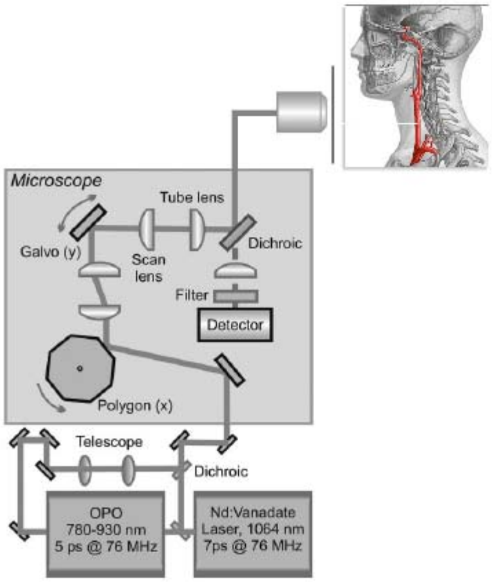

Figure A.5 Representative schematic of the instrumentation to be utilized to detect HIV-1 in-vivo. A Nd: Vanadate laser pumps a dual-wavelength OPO. The CARS signal is generated in the backwards direction and is collimated and separated from the pump by a filter and focused onto a detector.[19]

Unlike most microscopes, where the microscope slide can move, in this experiment we will need to move the microscope objective. This type of motion is critical for the later studies, where the sample (animal/person) cannot move, so the objective must move, to acquire the spatially offset signal. This can easily be achieved by placing the entire microscope objective on a translational motor, as depicted in Figure A.5. Currently there is research being done using such devices to study breast cancer[20] and to determine the contents of a sealed container[10].

To test the spatially offset method, we will design a special cuvette, in order to carry out these measurements. As depicted in Figure A.6, this cell will have two types of cuvettes. In cuvette A will be a solution containing only background fluid. Cuvette B contains a different sample with probe in it. The cells will be initially coated with a white polyester film, to make them visibly opaque. Given the turbidity of skin (which is the eventual goal for these experiments) we will no longer use the polyester film, but we will switch to using chicken skin[21]. Chicken skin will offer the turbidity we need to more closely mimic the biological system. The first experiments probe the cell with cuvettes A filled with neat water and cuvettes B containing 0.2 μm polystyrene beads suspended in water. When we scan the microscope over the regions of the cell, we will either observe a spectrum that is just from cuvettes A or we will see a spectrum from cuvettes A and that of cuvette B, we will subtract the spectrum from A to determine the spectrum for cuvette B, which will match the spectrum collected from just the CARS experiment.

Once the device had been able to successfully detect the polystyrene beads in water, we will suspend them in human serum. This will allow us to try to resolve the polystyrene bead from the rest of the serum. Once we are able to resolve the beads in the human serum, we will add them to whole human blood. Upon resolving the beads against the polyester film, we will repeat

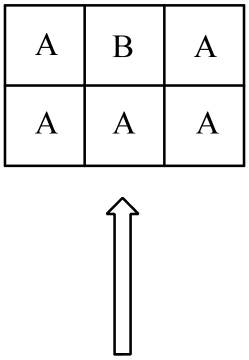

Figure A.**6** Top view of the cell design to test the spatially offset part of the CARS microscope. The hollow arrow indicates direction of the laser light entering the cell. The cell itself will be made up from 6 disposable plastic cuvettes. To make them visually opaque, we will use a white polyester film at first, and later using chicken skin. Cuvettes A and B will be filled with specific solutions to the experiments designs.

the last experiment, enclosing the cell with chicken skin. Once we have determined that we can resolve the spectrum of the polystyrene beads, we will move to a biological system, the feline samples.

A.3.b Aim 2: Determining Infection of Feline Specimens with the Feline Immunodeficiency Virus

As a test case, we first need to test the validity of the instrument on an animal model. Feline immunodeficiency virus or FIV, was discovered in 1986. FIV and HIV have a lot in common, even though they are such different species. FIV has about 45% identical residues to that of HIV. FIV also attack the cat's cells in a similar manner that of HIV, instead of using a gp120, FIV has a gp70. Given how similar the viruses are in structure and function, we expect the Raman spectrum of FIV to be similar to that of HIV. We will explore whole blood samples from cats that are infected with FIV and those that have not been infected. Initial experiments will enlist the cell described in section A.3.a. By placing FIV infected blood in cuvette B and non-infected blood cuvette A, we will be able to resolve the FIV in the infected blood spectrum. Once this has been determined we will place solid meat, such as a piece of chicken breast, and thread a piece of tygon tubing, bore diameter 1/8", through it, to mimic the vein we will be looking for.The chicken breast is used to give added turbidity, which will be used to model muscle and other fiberous tissue that is not skin. Tygon tubing will be utilized due to its wide variety and availability. If tygon tubing presents a problem, we will use dialysis tubing. Infected blood will flow through the tygon tubing at rate of 200 mL/min, which is the average value of blood flowing through the jugular vein of a cat. This will be used to determine the parameters for penetrating tissue in a living organism. The turbidity of the skin and chicken breast will provide an adequate model for the in-vivo studies. Once these tests are completed, we will move to cat to determine the presence of the FIV virus in vivo.

In-vivo studies will be carried out by sedating the feline, and taking a SO-CARM measurements on the cats external jugular vein. This vein is close to the surface of the cat and has a large amount of blood flowing through it. A series of measurements will take radially, around the neck across the skin, making sure to hit regions with the vein and regions without the vein present, for about 2 cm, in 0.10 cm increments for about 5 sec per increment. This should provide enough spectra of the surrounding tissue for the single value decomposition to separate out the blood spectrum from the rest of the surrounding media. Once the infection has been determined in the feline specimens, we will move to human subjects.

A.3.c Aim 3: Determining Infection of Human Subjects with HIV

How do we apply the above experiment to humans? Speed of these measurements vs cats.By moving the radially around the neck to the carotid artery over the span of about 3 cm in 0.25 cm increments, acquiring the signal for 5 sec per increment, we should have a sufficient signal to be able to do the subtraction needed from the spatially-offset experiment. The average lumen diameter for the common carotid artery is about 5-7 mm[22] By moving this number of steps, we can ensure that we have some signals from the carotid artery and others that will be from the surrounding tissues for the spatially offset comparison. Once the spatially-offset subtraction can be done, we will be able to resolve a spectrum similar to that in figure 4, which would be indicative of the blood in the sample. The resultant spectrum will be a combination of the blood, gp120, gp41, gp24, and the carbohydrates associated with HIV. Once compared to known Raman spectra of the HIV virus in human serum, infection will be able to be determined.

A.4 Overall Proposal Significance and Future Studies

A.4.a Development of a Technique to Transdermally Detect Infectious Agents.

Direct detection of infectious agents in vivo is critical, limiting the potential for possible infection to the doctor. More than 60% of the cases of occupationally transferred (health care employees getting infected in the job) involve drawing of blood for testing. Direct detection also saves valuable time, where doing secondary detection and amplification tests can take valuable time. The ability for a doctor to diagnose a patient's infection without having to draw blood and/or do time consuming lab work ups is a major benefit to this technique. Samples will need to have a significant viral load, 10,000 replicants/mL, to be detectable initially. Having such a viral load will ensure that a signal can be acquired for the HIV in the blood.

This device can easily be modified to look for any number of diseases or defects at the same time. Whether it is used for detecting breast cancer or hepatitis B, each disease will have a unique Raman spectrum and thus making them detectable.

A.5 Conclusion

These experiments will confirm the ability for this technique to be used for detection of HIV in the human body without having to take a blood sample. Do date, there are only a few tests that can determine infection of HIV without drawing blood, and most that do not draw blood are inaccurate or have long lab processing times. Even outside the medical field, the ability to probe the interior of an object without disrupting it can be heavily utilized.

This device also has the ability to be miniaturized into a portable device. By making this device portable, it can be used to scan for disease in places like sub-Saharan Africa, where HIV infection is at an all time high or to be used in clinics to determine infection of patients awaiting treatment to help minimize exposure to health care professionals. It can also be used in preliminary screenings in hospitals, where results can be given to a doctor before they even see the patient.

A.6 References

(1) Report on the global AIDS epidemic, UNAIDS, 2008.

(2) The Relationship Between the Human Immunodeficiency Virus and the Acquired Immunodeficiency Syndrome National Institute of Health, 1995.

(3) Quinn, T. C. The Lancet **1996**, 348, 99-106.

(4) Rambaut, A.; Posada, D.; Crandall, K. A.; Holmes, E. C. Nature Review Genetics **2004**, 5, 52-61.

(5) Robertson, D. L.; Hahn, B. H.; Sharp, P. M. J. Mol Evol **1995**, 40, 249-259.

(6) Chou, R.; Huffman, L. H.; Fu, R.; Smits, A. K.; Korthuis, P. T. Annals of Internal Medicine **2005**, 143, 55-73.

(7) False-Positive Oral Fluid Rapid HIV Tests---New York City, 2005--2008, 2008.

(8) Ronaldson, P. T.; Bendayan, R. Molecular Pharmacology **2006**, 70, 1078-1098.

(9) Wang, D.; Coscoy, L.; Zylberberg, M.; Avila, P. C.; Boushey, H. A.; Ganem, D.; DeRisi, J. L. PNAS **2002**, 99, 15687-15692.

(10) Eliasson, C.; Matousek, P. Anal. Chem. **2007**, 79, 1696-1701.

(11) Ochieng, W.; Ogoyi, D.; Mulaa, F. J.; Ogola, S.; Musoke, R.; Otsyula, M. G. Afr Health Sci **2006**, 6, 3-13.

(12) Nestor, J.; Spiro, T. G.; Klauminzer, G. Proc. Natl. Acad. Sci. **1976**, 73, 3329-3332.

(13) Coherent Anti-Stokes Raman Scattering Microspectrometer, Spectra-Physics, 2007.

(14) Duncan, M. D.; Reintjes, J.; Manuccia, T. J. Optics Letters **1982**, 7, 350-352.

(15) Yiming, X.; Chuanzong, L. Science in China **2005**, 48, 117-132.

(16) Wyatt, R.; Kwong, P. D.; Desjardins, E.; Sweet, R. W.; Robinson, J.; Hendrickson, W. A.; Sodroski, J. G. Nature Review Genetics **1998**, 393, 705-711.

(17) Wood, B. R.; Caspers, P.; Puppels, G. J.; Pandiancherri, S.; McNaughton, D. Anal Bioanal Chem **2007**, 387, 1691-1703.

(18) Cheng, J.-X.; Xie, X. S. J. Phys. Chem. B **2004**, 108, 827-840.

(19) Evans, C. L.; Xie, X. S. Annual Review of Analytical Chemistry **2008**, 1.

(20) Keller, M. D.; Majumder, S. K.; Mahadevan-Jansen, A. Optics Letters **2009**, 34, 926-928.

(21) Smith, Z. J.; Berger, A. J. Optics Letters **2005**, 30, 1363-1365.

(22) Ruan, L.; Chen, W.; Srinivasan, S. R.; Sun, M.; Wang, H.; Ahmet Toprak; Berenson, G. S. Journal of the American Heart Assoication **2009**.

LIST OF ABBREVIATIONS

AIDS	Acquired Immune Deficiency Syndrome
AOT	Aerosol OT (Aerosol Organic Trapper)
BBO	β-Barium borate
BL	Ground State Bleach
CAMELSPIN	Cross-Relaxation Appropriate for Mini-Molecules Emulated by Spin-Locking
CARM	Coherent Anti-Stokes Raman Microscopy
CARS	Coherent Anti-Stokes Raman Spectroscopy
Chol	Cholesterol
CIF	Central Instrument Facility
CMC	Critical Micelle Concentration
CRCM	Critical Reverse Micelle Concentration
CTAB	Cetyltrimethylammonium bromide
d_1	First Delay (NMR)
d_2	Second Delay (NMR)
DLS	Dynamic Light Scattering
DMSO	Dimethyl sulfoxide
DNA	Deoxyribonucleic acid
ELISA	Enzyme-linked Immunosorbent Assay

ESA	Excited State Absorption
FID	Free Induction Decay
FIV	Feline Immunodeficiency Virus
FT	Fourier Transform
FWHM	Full Width Half Maximum
gp24	Glycoprotein 24 (HIV)
gp41	Glycoprotein 41 (HIV)
gp120	Glycoprotein 120 (HIV)
HIV	Human Immunodeficiency Virus
HOHAHA	Homonuclear Hartmann-Hahn Spectroscopy
HPTS	8-Hydroxypyrene-1,3,6-trisulfomic acid
IGE	Igepal CO-520
NIR	Near-Infrared
NMR	Nuclear Magnetic Resonance
NOE	Nuclear Overhauser Effect
NOESY	Nuclear Overhauser Effect Spectrscopy or Nuclear Overhauser Enhancement Spectroscopy
OPO	Optical Parametric Oscillator
PCR	Polymerase Chain Reaction
PEO	Polyethylene glycol
pw_1	First Pulse Width (NMR)

pw_2	Second Pulse Width (NMR)
RM	Reverse Micelle
ROESY	Rotating Frame Nuclear Overhauser Effect Spectroscopy
SE	Stimulated Emission
SO	Spatially Offset
SORS	Spatially Offset Raman Spectroscopy
sw	Sweep Width (NMR)
t	Acquisition Time (NMR)
T_1	Spin-Lattice Relaxation (NMR)
TMS	Tetramethylsilane
UV	Ultra Violet
V_1	Orthovanadate (VO_4^{2-})
V_2	Pyrovanadate ($V_2O_7^{4-}$)
V_3	Trivanadate anion ($V_3O_{10}^{5-}$)
$V_{4\ cyc}$	Cyclic tertavanadate ($V_4O_{12}^{4-}$)
$V_{4\ lin}$	Linear tetravanadate ($V_4O_{13}^{6-}$)
V_5	Cyclic pentavanadate ($V_5O_{14}^{3-}$)
V_{10}	Decavanadate ($V_{10}O_{28}^{6-}$)
V_A	Central Vanadium Atoms in Decavanadate (V_{10})
V_B	Equatorial Vanadium Atoms in Decavanadate (V_{10})
V_C	Axial Vanadium Atoms in Decavanadate (V_{10})
Vis	Visable